Universität Zürich[UZH]

UNIVERSITÀ DEGLI STUDI DI SALERNO

INTERNATIONAL PH.D. IN ASTROPHYSICS AND CONDENSED MATTER PHYSICS
(X SERIES II COURSE – 2009/2012)

Facoltà di Scienze Matematiche Fisiche e Naturali
Dipartimento di Fisica "E.R. Caianiello" and
Mathematisch-naturwissenschaftlichen Fakultät

PH.D. THESIS

by

Sergey Mirzoyan

Microlensing Towards the SMC and CMB Probing the Dark Matter in Galaxies

Advisers

Prof. Gaetano Scarpetta
Prof. Philippe Jetzer
Prof. Vahe Gurzadyan

April 2013

Microlensing Towards the SMC and CMB Probing the Dark Matter in Galaxies

Contents

List of Figures

List of Tables

-

Introduction

The last two decades were revolutionary in cosmology as astronomers have discovered that the universe is filled with not only dark matter, but also the even more enigmatic dark energy (Perlmutter et al., 1999; Riess et al., 1998; Spergel et al., 2003). The nature of these two dark components of the universe is currently one of the most fundamental mysteries in physics. While our understanding of dark energy is still inadequate, recent progress on dark matter has been promising even though the dark matter particle itself remains unidentified. The first hints of the existence of dark matter, or ”missing mass”, as it was originally known, came relatively early in the history of extragalactic astronomy. In the 1930's, Fritz Zwicky realized that the galaxies in the Coma cluster are moving much faster than expected based on the amount of luminous matter present (Zwicky, 1933, 1937). He therefore argued that the cluster galaxies must have masses of order 100 times larger than one would calculate for only stellar systems. Alike results were obtained soon thereafter by Smith (1936) for the Virgo cluster.

In the 1970's, observations convincingly demonstrated that the missing mass problem is also present in individual spiral galaxies (Rubin & Ford, 1970; Roberts & Whitehurst, 1975; Ostriker et al., 1974; Einasto et al., 1974) as well as clusters. These studies showed that spiral galaxies have flat rotation curves extending out to radii of tens of kpc. Assuming spherically symmetric mass distribution for galaxy , Newtons Law of Gravitation Newton (1687) states that

$$V_{rot}(R)^2 = \frac{GM(R)}{R} \tag{1}$$

where V_{rot} is the rotation velocity as a function of radius, and M is the mass interior to a radius R. A flat rotation curve therefore implies that the mass enclosed increases linearly with radius and that the density declines as R^{-2}. Since the light distribution of spirals tends to decline exponentially with radius (de Vaucouleurs, 1959; Freeman, 1970), it is clear that these galaxies must contain non-luminous material in their outer regions. These early observations typically revealed at least 10 times more mass than would be expected for a normal stellar population. Later on elliptical and S0 galaxies (Knapp et al., 1978; Faber & Gallagher, 1979), galaxy pairs (Page, 1962; Turner, 1976; Peterson, 1978), and galaxy groups (Gott & Turner, 1977; Rood & Dickel, 1978; Faber & Gallagher, 1979) were found to require large mass-to-light ratios as well.

Various types of systems were studied using wide range of observational techniques. Compatibility of the results suggests existence of dark matter. Constituents and distribution of dark matter are two of the most important puzzles of the present physics.

According to observations of structures larger than solar systems, as well as Big Bang cosmology interpreted under the Friedmann equations and the Friedmann-Lemaître-Robertson-Walker (FLRW) metric, dark matter accounts for 23% of the mass-energy content of the observable universe and the dark energy for ~73%. In comparison, ordinary matter accounts for only 4.6% of the mass-energy content of the observable universe (Fig. 1).

A wide variety of candidates for the dark matter have been suggested, most falling into one of two broad classes: (1) some unknown elementary particle-weakly interacting massive particles (WIMPS) that interact only through gravity and the weak force, but there are also more exotic possibilities such as axions; (2) non-luminous macroscopic objects, such as neutron stars, black holes, faint white dwarfs, faint stars or massive compact dark objects as brown dwarfs or Jupiters.

In 1936 A. Einstein published a short note in Science entitled ”lens-like action of a star by the deviation of light in the gravitational field”, with the following final comment: ”There

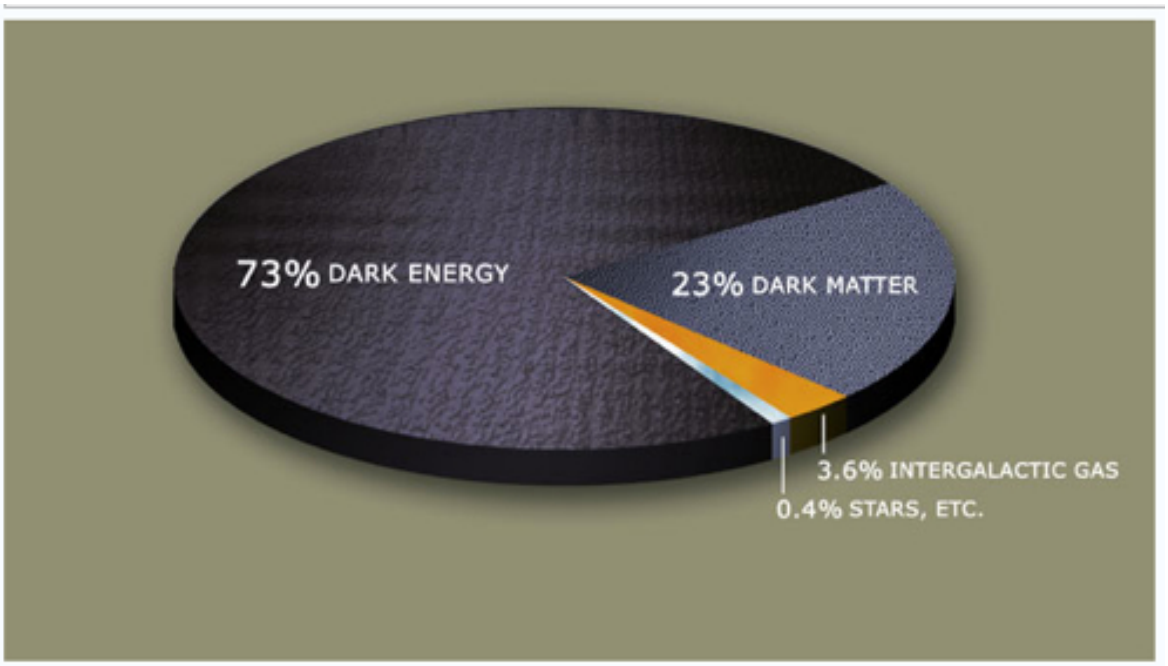

Figure 1: The matter-energy composition of the universe according to ΛCDM. Image is taken from the web page (1).

is not great chance of observing this phenomenon." The effect was already predicted by A. Einstein as early as 1912, before completion of the general theory of relativity. S. Liebes considered again the properties of the gravitational lenses in 1964, and studied the possibility to detect high magnification events, mentioning the possibility to detect invisible compact objects through microlensing.

In 1986 B. Paczyński (Paczyński, 1986) suggested to detect massive compact halo objects (MACHO) of the Galactic halo in the direction of the Magellanic Clouds using gravitational microlensing effect (see Fig. 2). Since then, several experiments have been monitoring millions of stars towards the Large and Small Magellanic Clouds and candidates have been observed towards the two targets (Alcock et al., 1993; Aubourg et al., 1993; Ansari et al., 1996; Alcock et al., 1997; Afonso et al., 1999; Lasserre et al., 2000).

The event rates towards the LMC and SMC can be used to ascertain whether astrophys-

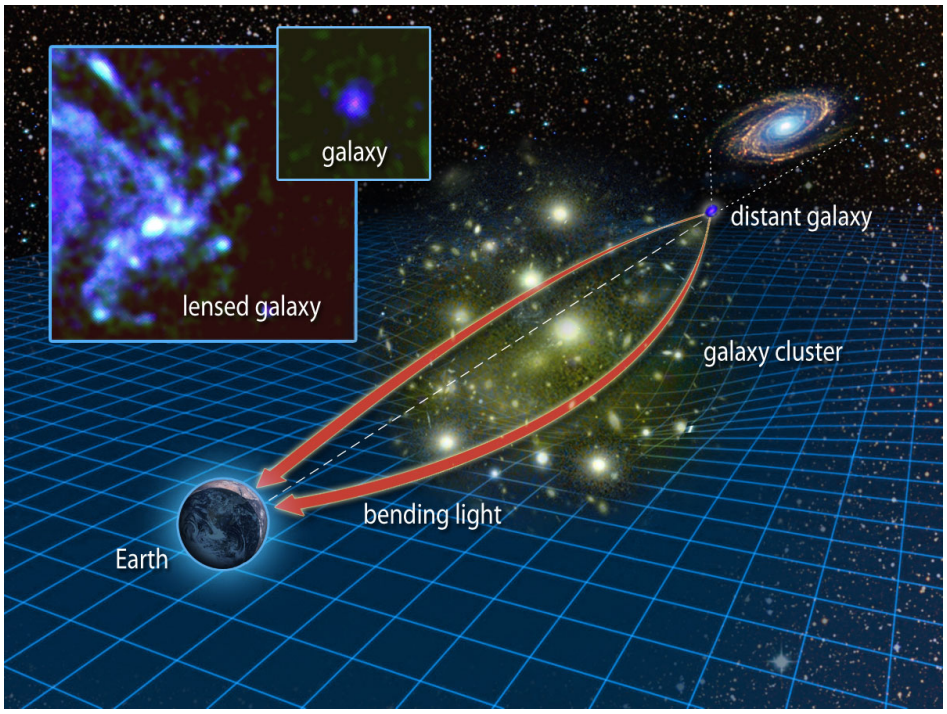

Figure 2: Illustration of the gravitational lensing effect. The gravity of a gigantic cluster of galaxies has bent and magnified the light of the distant spiral galaxy Sp1149 making its spiral arms visible (2).

ical objects comprise the dark matter halo of the Milky Way (Roulet & Mollerach, 1997; Paczyński, 1996). The rate of microlensing seen towards the LMC exceeds that predicted from known Galactic sources (Alcock et al., 1997). One of the puzzling issues of the astrophysics is to understand whether this excess is due to Galactic dark matter in form of MACHOs. In other words, the key to resolving this issue lies in determining the location of the lensing objects.

The issue of the Galactic halo dark fraction is still remaining open too. Quantitatively, the MACHO collaboration claimed for a mass halo fraction in form of $(0.2 - 0.9)M_{\odot}$ MACHOs of about $f \approx 20\%$ out of observations of 13-17 candidate microlensing events towards the LMC (Alcock et al., 2000). On the other hand, the analyses of the EROS (Tisserand et al.,

2007), and the OGLE collaboration, for both OGLE-II (Wyrzykowski et al., 2009, 2010) and OGLE-III (Wyrzykowski et al., 2011a,b), out of observations towards both the LMC and SMC, concluded much less upper limit on the MACHO contribution in the same mass range. In particular, EROS collaboration reported an upper limit of $f = 8\%$ at 95% CL for $0.4M_{\odot}$ mass MACHOs, and OGLE $f = 6\%$ for $0.4M_{\odot}$ MACHOs and 4% for mass range between $(0.01 - 0.15)M_{\odot}$.

The goal of this thesis is to contribute in understanding of dark matter and estimating dark matter fraction in the galactic halo. The firs three chapters are theoretical reviews on Dark Matter and Dark Energy, MW and SMC morphology and gravitational lensing theory. Particularly, in the Chapter 1 we discuss the evidence and problems of both Dark Matter and Dark Energy. In particular, we discuss in details possible constituents of Dark Matter and possible explanation of Dark Energy. Then, in Chapters 2 and 3 we describe SMC and MW morphological appearances and kinematics and gravitational lensing theory. For microlensing purposes the SMC has somewhat peculiar orientation with respect to the line-of-sight, then LMC. It's elongated shape makes it very valuable target. As the Einstein radius R_E proportional to $\sqrt{D_{LS}}$, so this elongation is expected to enhance the SMC self-lensing signal. However, the morphology of the SMC is matter of debate and, therefore, we have described large set of the SMC morphological appearances known up to now.

The Capter 4 is an article submitted to the MNRAS journal. Here we present a new analysis of the results of the EROS-2, OGLE-II, and OGLE-III microlensing campaigns towards the Small Magellanic Clouds. Through a statistical analysis we address the issue of the nature of the reported microlensing candidate events, whether to be attributed to lenses belonging to known population or to the would be population of dark matter compact halo objects (MACHOs). In particular, we present profiles of the optical depth and, comparing to the observed quantities, we carry out analyses of the events position and duration. Then, we evaluate and study the microlensing rate and calculated the expected number of events

comparing with the observed one. Finally, we evaluate the upper limit for the halo mass fraction in form of MACHOs given the expected luminous and MACHO lensing signal.

The second topic of this thesis is devoted to the galactic dark baryon studies using Cosmic Microwave Background (CMB) as new tool of investigation. The Chapter 5 is a review dedicated to the CMB. Some useful information about HEALPix method is given as well. While the Capter 6 is a published article in A&A journal. Here we have shown the possible detection of the Andromeda galaxy (M31) rotation in the Wilkinson Microwave Anisotropy Probe(WMAP) data (De Paolis et al., 2011, 2012). We used the 7-year WMAP three bands (W, V, and Q) data to trace the disk and the halo of that nearby giant spiral galaxy, by dividing the region of the sky around M31 into several concentric circular areas. An asymmetry in the mean microwave temperature in the M31 disk along the direction of the M31 rotation has been observed with a temperature contrast up to $\simeq$130 μK/pixel. As for M31 halo, an excess exists as well, but the effect is much weaker then for the disk, up to a galactocentric distance of about 10° ($\simeq$120 kpc) with a peak temperature contrast of about 40 μK/pixel. We also simulated 500 random control fields in the real WMAP maps and 500 sky maps from best-fitted cosmological parameters in order to verify the robustness of the results. Finally, we estimated the probability of this effects to be due to random fluctuations of the CMB signal.

Acknowledgements

This Ph.D thesis is the yield of the three years of my studies in the University of Salerno and University of Zürich. I would like to express my deep gratitude to my supervisors, Professor G. Scarpetta and Professor Ph. Jetzer for fruitful discussions and constant help. I am specially grateful to Prof. V. Gurzadyan for collaboration and for his valuable advises. Additionally, I would like to express my gratitude to Dr. S. Calchi Novati, Dr. V. Bozza, Dr. C. Tortora and Dr. M. Lubini for useful discussions on astrophysical and mathematical topics.

Finally, I am thankful to my family for their love, respect and continuous support, in particular to my father, S. Mirzoyan and my mother, G. Sahakyan, whom I dedicate this thesis.

Chapter 1
Dark Matter and Dark Energy

Almost all information on celestial bodies comes to us via photons. Mostly objects are observed because of emitted light. If not so, like for example in some nebulae, we notice dark regions against otherwise luminous background which are due to absorption of light. Thus both light absorption and light emission allow us to trace the matter in the Universe. However, another direct way to determine the masses of astronomical bodies is using motions of other bodies around or within the body under study. In some cases such directly estimated total mass exceeds the estimated luminous one. This suggests the need of **missing** or **dark matter** concepts. Another evidence for dark matter is measurements of fluctuations of the Cosmic Microwave Background (CMB) radiation in combination with data from type Ia supernovae in nearby and very distant galaxies which give information on the curvature of the Universe that depends on the amount of both **Dark Matter** and **Dark Energy**.

The Chapter is organized as follows: In Section 1.1 we describe various evidences of the dark matter. The possible constituents of dark matter and contribution in the total density of the universe are also discussed. Section 1.2 is dedicated to the dark energy. Here we start from the accelerating expansion of the Universe, the possible relationship of this expansion with the Λ cosmological term. The contribution of dark energy density in the total one is also discussed.

1.1 Dark Matter

The most convincing and direct evidence for dark matter on galactic scales comes from the observations of the rotation curves of galaxies. Observed rotation curves usually show flat behavior at large distances. A typical example of flat rotation curve is shown in Fig. 1.1.

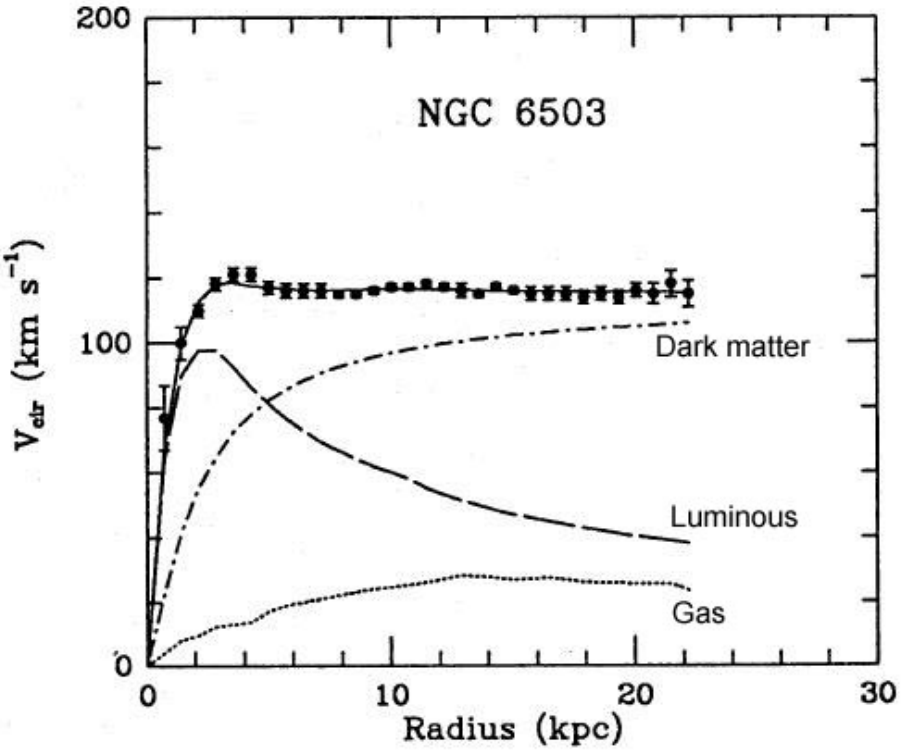

Figure 1.1: Rotation curve of NGC 6503. The dotted, dashed and dashdotted lines are the contributions of gas, disk and dark matter, respectively.

In Newtonian dynamics the circular velocity is expected to be

$$V_{rot}(r)^2 = \frac{GM(r)}{r} \tag{1.1}$$

where

$$M(r) = 4\pi \int \rho(r) r^2 \mathrm{d}r \tag{1.2}$$

and $\rho(r)$ is the mass density profile, and should be falling $\propto 1/\sqrt{r}$ beyond the optical disk. The fact that $V_{rot}(r)$ is approximately constant implies the existence of an halo with $M(r) \propto r$ and $\rho(r) \propto 1/r^2$.

It is important to stress that assuming an existence of the dark halo in the galaxy and adopting the following spherical isothermal profile for the halo

$$\rho_{DH}(r) = \rho_0 \frac{a^2 + r_0^2}{a^2 + r^2} \tag{1.3}$$

provides a qualitatively consistent description of the data. Here a is the core radius, ρ_0 is the local halo density and $\rho(r_0) = \rho_0$.

There is also cosmological evidence for DM. Our theoretical prejudice, as well as some specific models of the early Universe such as inflationary models, require density parameter $\Omega_0 = 1$, where $\Omega_0 = \rho_0/\rho_c$, critical density is

$$\rho_c \equiv \frac{3H_0^2}{8\pi G} = 1.88 \times 10^{-29} h^2 g/cm^3 = 2.76 \times 10^{11} h^2 M_\odot/Mpc^3 \tag{1.4}$$

and corresponds the present mean density required to make the Universe bound.

In order to determine the M/L ratio, which is the estimator of the dark matter, one must estimate the mean luminosity density. Davis et al. (1982) and Kirshner et al. (1983) estimated it to be

$$j_0 \approx 1.7 \times 10^8 h (L_\odot/Mpc^3)_V \tag{1.5}$$

and hence, using (1.4) we derive

$$\Omega_0 = \rho_0/\rho_c = \frac{M}{L}\frac{j_0}{\rho_c} \approx \frac{(M/L)_V}{1600h} \tag{1.6}$$

which clearly means that $(M/L)_V$ must be $1600h$ times larger in order to have $\Omega_0 = 1$ (unity density parameter means flat Universe). To give an idea about this large $(M/L)_V$ we recall that it is by about 4 times larger than that of the Coma cluster and there is no known system of galaxies whose dynamical mass implies a mass-to-light ratio as high as $1600h$.

An independent limit on the total amount of baryonic matter in the Universe comes from

the study of primordial nucleosynthesis. The present amount of deuterium and helium is mainly produced during an early phase of the Universe. The observed abundances of deuterium and helium set a limit on Ω_0 in the form of baryonic matter (Bahcall et al., 2004).

$$\Omega_B \approx (0.011 - 0.048)h^{-2} \tag{1.7}$$

which, using Eq. 1.6 translates $20 < (M_B/L)_V h < 80$, where M_B is the mass of baryons.

Taking into account all the underlying arguments, one may conclude that. firstly, there must be both baryonic DM (to provide the DM in the Solar neighborhood) and non-baryonic DM (so that $\Omega_0 = 1$ without violating Eq. 1.7), secondly, the DM in galaxies may be baryonic but the DM in clusters like Coma must be non-baryonic (unless h is as small as 0.5, in which case the upper limit to $(M_B/L)_V$ implied by nucleosynthesis may be barely consistent with the (M/L)'s of rich clusters) and thirdly the ratio of DM to luminous mass must be larger outside galaxies, groups, and clusters than inside, since the mass-to-light ratios of these systems are not sufficient to close the Universe.

1.1.1 Dark Baryons

As we have stressed before one of the main puzzling questions is the distribution of the dark matter. With the exception of clusters, where the dark baryons exist as hot, x-ray emitting intracluster gas, the nature of the dark baryons is not known. Clusters only account for around 10% or so of the baryons in the Universe (Persic & Salucci, 1992) and the dark baryons elsewhere, which account for 90% or more of all the baryons, could take on a different form.

The two most promising possibilities for the dark baryons are diffuse hot gas and "dark stars". There are two arguments for dark stars as the baryonic dark matter (Turner, 1999). First, the gaseous baryons not associated with clusters have not been detected. Second, the results of the microlensing surveys toward the LMC and SMC (Spiro et al., 1999; Alcock et

al., 2000), where consistent $\sim (20-30)\%$ of our halo being in the form of $0.5M_{\odot}$ mass white dwarfs.

Another possible candidates for "dark stars" are non-luminous macroscopic objects, such as neutron stars, black holes, faint white dwarfs, faint stars or massive compact dark objects as brown dwarfs or Jupiters.

1.1.2 Cold Dark Matter

The idea of non-baryonic dark matter is inserted to satisfy the condition for the ordinary and overall matter density parameters. As the luminous component accounts only for $0.007 < \Omega_l < 0.014$ (Goenner, 1994), matter density parameter falls within $0.2 < \Omega_m < 0.36$ and $\Omega_l < \Omega_b$, an existence of some non luminous, dark baryonic matter is required. From other side, the discrepancy between Ω_b and Ω_b implies the existence of a dark non baryonic component.

Now, another important question one may ask is, "what does non-baryonic matter composed of?". There are several candidates for non-baryonic dark matter, which are

• Neutrino

Neutrino is relativistic collisionless particle. A stringent constraint on the neutrino relic density comes from the analysis of CMB anisotropies, combined with large-scale structure data, suggesting $\Omega_\nu h^2 < 0.0067$ (95% confidence limit). This contribution suggests that neutrinos are not dominant component of dark matter.

• Sterile neutrinos

These hypothetical particles are similar to Standard Model neutrinos, but without Standard Model weak interactions, apart from mixing. They were proposed as dark matter candidates in 1993 by Dodelson & Widrow (Dodelson & Widrow, 1994).

• Axions Those are very light particles introduced in an attempt to solve the problem of Charge Parity violation in particle physics, axions have also often been discussed as a dark

matter candidate. Laboratory searches, stellar cooling and the dynamics of supernova 1987A constrain axions to be very light ¡ 0.01 eV). Furthermore, they are expected to be extremely weakly interacting with ordinary particles, which implies that they were not in thermal equilibrium in the early universe. The calculation of the axion relic density is uncertain, and depends on the assumptions made regarding the production mechanism. Nevertheless, it is possible to find an acceptable range where axions satisfy all present-day constraints and represent a possible dark matter candidate (Rosenberg & van Bibber, 2000).

- Supersymmetric candidates
  - Neutralinos

The neutralino is an object that arises in theories of elementary particles involving supersymmetry. The neutralino weighs as much as a large atom or small molecule, and hardly interacts with normal matter except through its gravitational attraction.

  - Sneutrinos

The superpartners of the Standard Model neutrinos in supersymmetric models have long been considered as dark matter candidates. It has been shown that sneutrinos will have a cosmologically interesting relic density if their mass is in the range of 550-2300 GeV.

  - Gravitinos

Gravitinos are the superpartners of the graviton in supersymmetric models. In some supersymmetric scenarios, gauge mediated supersymmetry for example, gravitinos can be the lightest supersymmetric particle and be stable. Gravitinos are thus very strongly theoretically motivated.With only gravitational interactions, however, gravitinos are very difficult to observe (Feng et al., 2003).

  - Axinos

Axinos, the superpartner of the axion, were believed until recently to only be capable of acting as a warm, or hot, dark matter candidate (Bonometto et al., 1994; Goto & Yamaguchi, 1992). It has been shown, however, that for quite low reheating temperatures, cold axino

dark matter may be possible (Covi et al., 2001; Chun et al., 2000). In many ways, axinos and gravitinos share similar phenomenological properties.

1.2 Dark Energy

Our theoretical prejudice as well as inflationary models give a tip that the Universe is flat ($\Omega_0 = 1$) or nearly flat. The estimated dark matter (baryonic and non-baryonic) density parameter contributes in overall just for ≈ 0.3. This means that matter by alone does not succeed in explaining unity of Ω_0.

In 1998 two independent groups discovered an accelerating behavior of the Universe based on the type Ia supernovae (SN Ia) observations (Riess et al., 1998; Perlmutter et al., 1999). The reason for this acceleration, named dark energy (Huterer & Turner, 1999), has been still a mystery in spite of tremendous efforts to understand its origin over the last decade (Copeland et al., 2006; Durrer & Maartens, 2008; Caldwell & Kamionkowski, 2009). Dark energy is distinguished from ordinary matter in that it has a negative pressure whose equation of state ω_{DE} is close to -1. Independent observational data such as SN Ia (Wood-Vasey et al., 2007), Cosmic Microwave Background (CMB) (Spergel et al., 2007; Komatsu et al., 2009), and Baryon Acoustic Oscillations (BAO) (Eisenstein et al., 2005; Percival et al., 2010) have continued to confirm that about 70% of the energy density of the present Universe consists of dark energy.

The simplest candidate for dark energy is the cosmological constant Λ proposed by Albert Einstein at 1917 as a modification of his original theory of general relativity to achieve a stationary universe. The cosmological constant has the same effect as an intrinsic energy density of the vacuum with the equation of state $\omega_{DE} = -1$. Assuming that cosmological constant is identical with the vacuum energy arises the problem called Λ-problem, which is that there is $\sim$ 120 order of magnitude difference between vacuum and today's dark energy

densities.

Several efforts have been made to deal with this problem under the framework of particle physics and different treatments of understanding the property of dark energy have been done. For example, to clarify whether it is a simple cosmological constant or it originates from other sources that dynamically change in time. The dynamical dark energy models can be distinguished from the cosmological constant by considering the evolution of ω_{DE}. The scalar field models of DE such as quintessence (Copeland et al., 1998; Caldwell et al., 1998) and k-essence (Chiba et al., 2000; Armendariz-Picon et al., 2000) predict a wide variety of variations of ω_{DE}, but still the current observational data are not sufficient to provide some preference of such models over the Λ-Cold-Dark-Matter (ΛCDM) model.

Anyway, our understanding of the today's Universe is that the Universe contains $\Omega_r \approx 10^{-5}$ in radiation, $\Omega_b \approx 0.04$ in baryons, $\Omega_r \approx 0.23$ in cold, collisionless, non-baryonic (i.e. the Dark Matter), and $\Omega_{DE} \approx 0.73$ in some mysterious substance (i.e. dark energy) with $p \simeq -\rho$.

Chapter 2

The Milky Way and the Small Magellanic Cloud

Our Solar System resides in the galaxy called Milky Way. Milky Way is the second largest galaxy in the Local Group after Andromeda galaxy, which is also known as M31 (see Fig. 2.1). This galaxy is at about at 740 kpc distance from the Milky Way. There are number of dwarf galaxies in the Local Group, much closer to the Milky Way. The closest one is the Sagittarius dwarf galaxy at about 22 kpc from us. Another nearby galaxies are Small and Large Magellanic Clouds, at about 65 kpc and 50kpc distances from as, respectively, which are satellite galaxies of the Milky Way.

In this Chapter we focus on the morphology of the Milky Way and the Small Magellanic Cloud. We organize the Chapter as follows: In the Section 2.1 we describe the structure of the Milky Way galaxy, but concentrating only on Disk and Dark Halo of the Galaxy. While the Section 2.2 is dedicated to SMC morphology and kinematics.

2.1 The Milky Way

The Milky Way Galaxy structure is fairly typical of a large spiral system. This structure can be viewed as consisting of six separate parts: (1) a nucleus, (2) a central bulge, (3) thin and thick disks (4) spiral arms, (5) a spherical component, and (6) a massive halo (see Fig. 2.2). Some of these components blend into each other.

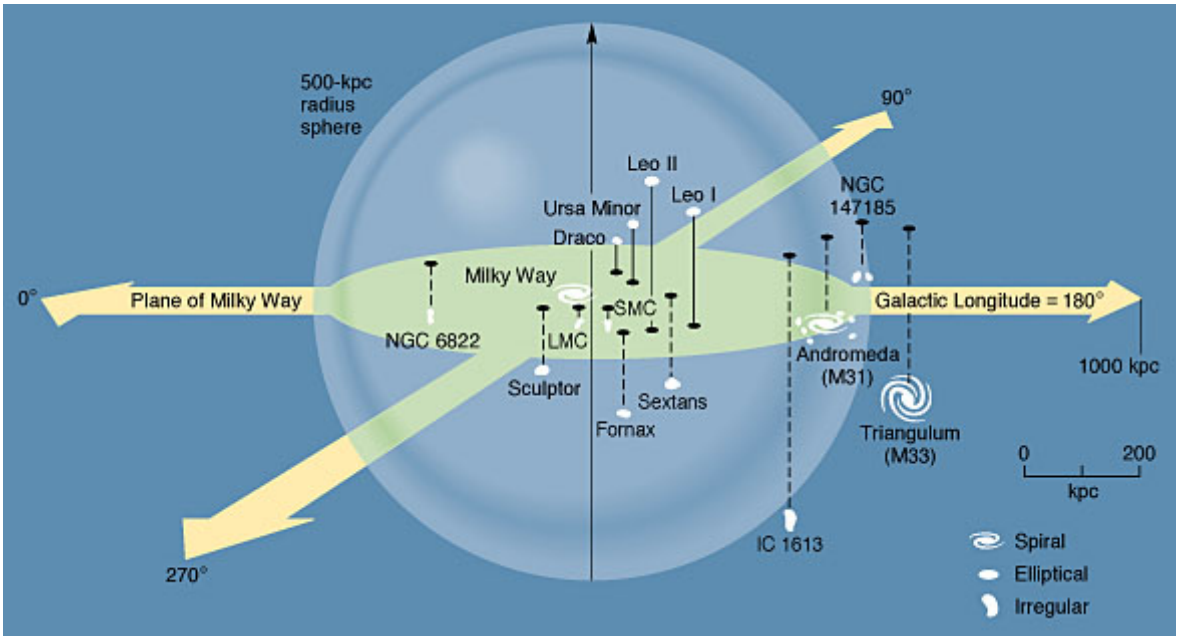

Figure 2.1: The Local Group. Positions of the group member galaxies are shown. The image is taken from the web page (3).

In this chapter I will describe components that lie on our line-of-sights towards the Small Magellanic Cloud and therefor can contribute as a lenses.

2.1.1 MW Disk

The disk is the most conspicuous part of the Galaxy, which extends from the center out to approximately 15 kpc. It can be thought of as being the underlying body of stars upon which the arms are superimposed. The thinnest component, often called the ”thin disk”, includes the dust and gas and the youngest stars, while a thicker component, the ”thick disk”, includes somewhat older stars.

The mass density profile is matter of the argument, since some of the authors believe

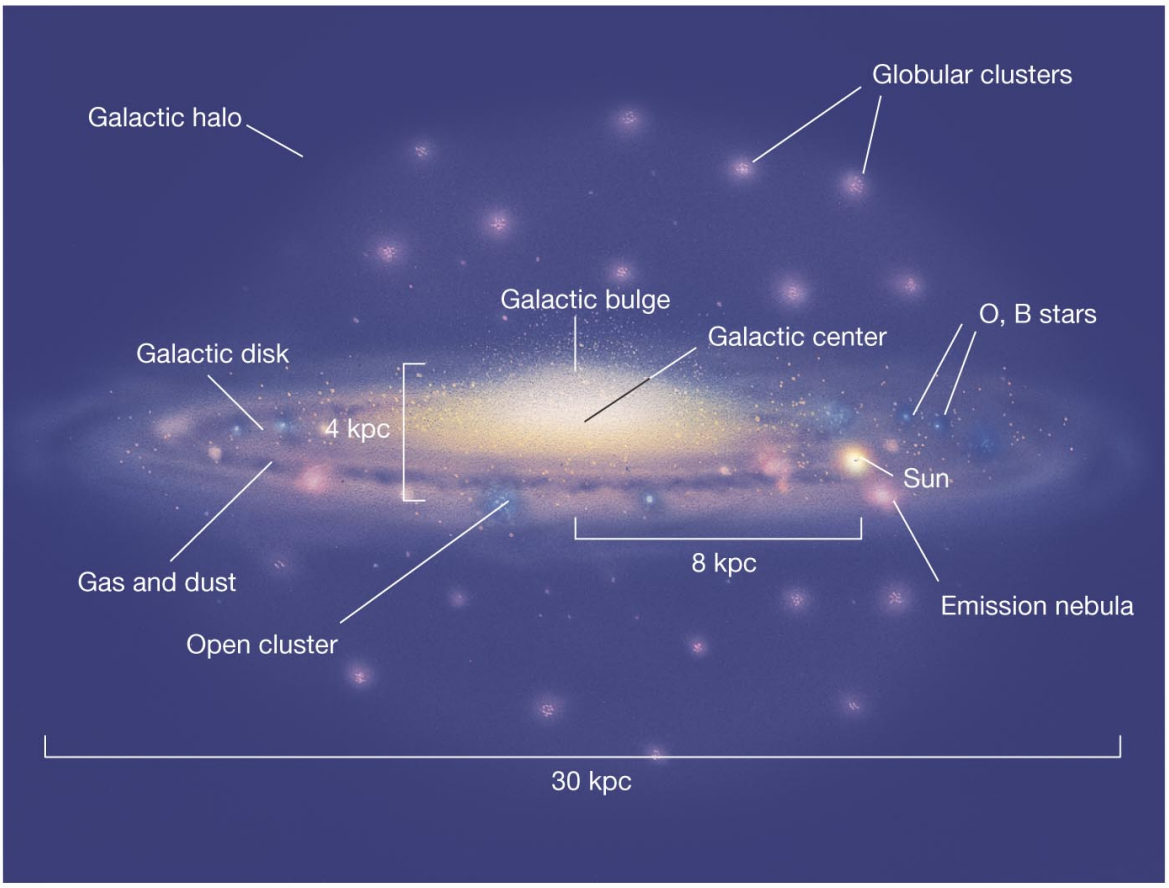

Figure 2.2: Milky Way structure. The Galactic Bulge, Disk, Halo, as well as the position of the Sun are demonstrated. Taken from the web page (4).

it to be composition of the $sech^2$ and exponential, and some others just double exponential profiles. However we describe it with the standard double exponential disc model as in Dehnen & Binney (1998) for each sub-disk, which is

$$\rho_d(R,z) = \rho_{d,\odot} Exp\Big(-\frac{R}{R_d} - \frac{|z|}{z_d}\Big) \tag{2.1}$$

with scale length R_d and scale height z_d, assuming a thin disc and a thick disc component. According the detailed stellar mass budget of Kroupa (2007) we fix the thin (thick) disc stellar central density to $\rho_{thin,\odot} = 0.044 M_\odot pc^{-3}$ ($\rho_{thick,\odot} = 0.050 M_\odot pc^{-3}$). For a scale height

$z_{d,thin}$ = 250 pc ($z_{d,thick}$ = 750 pc) and for scale length $R_{d,thin}$ = 2.75 kpc ($R_{d,thick}$ = 4.1 kpc) (Kroupa, 2007; Juríc et al., 2008; de Jong et al., 2010). The line-of-sight velocity dispersion are $30km/s$ and $40km/s$ for thin and thick disks, respectively.

2.1.2 The Halo of the Milky Way

Besides the stellar components, there are many indications that the mass of Galaxy is dominated by an extended, in first approximation spherical distribution of dark matter (see Chapter 1). The flatness of the rotation curve of the Galaxy (Fig. 2.3), with $v_c \simeq 220kms^{-1}$, implies

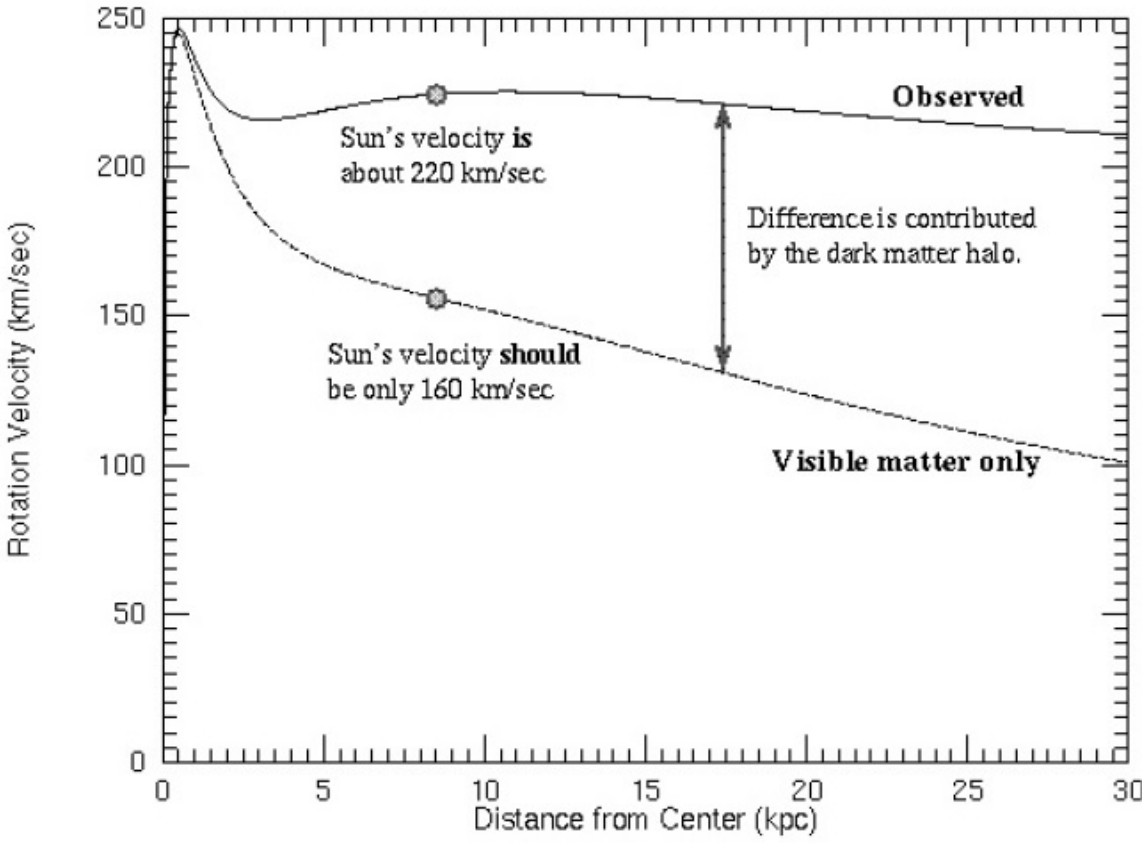

Figure 2.3: Rotation curve of the Milky Way. Taken from the web page (5).

that the halo density should vary as $\rho \propto r^{-2}$, and hence a simple parameterization used for it

is

$$\rho_{DH}(r) = \rho_0 \frac{a^2 + r_0^2}{a^2 + r^2} \tag{2.2}$$

where a is halo core radius, typically few kpc and $r_0 = 8$ kpc is the Sun distance from the Galactic center. There are different estimates for the core radius, in particular, Bahcall et al. (1983) estimated a equal to 2 kpc, while Alcock et al. (2000) used core value to be 5kpc, which is also consistent with the results by de Boer et al. (2005); Weber & de Boer (2010).

The velocity dispersion of the halo objects is usually adopted as constant and isotropic, with $\sigma_{DH} \simeq 155 kms^{-1}$. The density profile in Eq. 2.2 must be truncated in some large distance since otherwise the total mass would be divergent. It is believed that MW halo is composed mainly of dark matter which may extend far beyond the edge of the disk, plausibly beyond 200 kpc and its mass is $2 \times 10^{12} M_{\odot}$. Unfortunately, the investigation of the dark halo is very complicated due to its invisibility and our location inside the Galactic disk. The question related to the constituents of the dark halo is already discussed in the Chapter 1.

2.2 The Small Magellanic Cloud: morphological appearance and kinematics

Like its larger apparent neighbor, the Large Magellanic Cloud (LMC), the Small Magellanic Cloud was certainly known to the ancient southerners, and was probably mentioned by Amerigo Vespucci during his third voyage about 1503-1504. It became known to us only when Magellan went on his journey around the world, in 1519. The main body of the Small Magellanic Cloud has been assigned NGC 292 in Dreyer's catalog.

This galaxy looks like a piece of the Milky Way for the naked eye. It orbits our Milky Way galaxy at about 240,000 light years distance, which makes it the third-nearest external galaxy known (after the LMC and the 1994 discovered Sagittarius Dwarf Elliptical Galaxy).

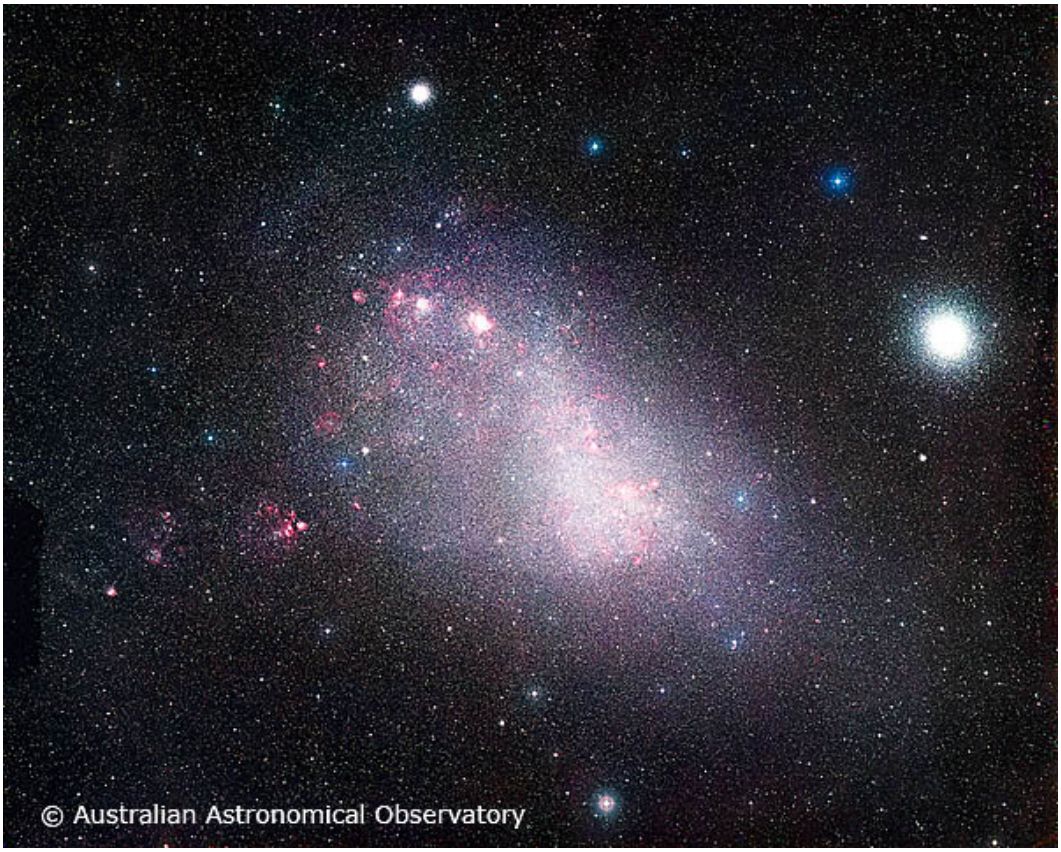

Figure 2.4: The picture of the SMC. Top left is NE. The picture is taken from the wab page (6).

It is dwarf irregular galaxy (see Fig. 2.4), and unlike the LMC its structure and kinematics are less well studied and understood. In the next two subsections we give a detailed description of the SMC morphology and kinematics.

2.2.1 Morphology

The SMC is a dwarf irregular galaxy orbiting, in interaction with the LMC, the MW (van den Bergh, 1999; McConnachie, 2012). The detailed spatial structure and overall characteristics of the SMC are still debated. According to the Gonidakis et al. (2009) the estimated coordi-

nates of the SMC Mass Center (J2000) is (RA,Dec) = (0:51:00, -73:7.2) and that the center is the same for all the different age population and are in good accordance with the kinematic center of the SMC. These coordinates of the SMC center is similar one given by Haschke et al. (2012), that are $\alpha = 0^h51^m$ and $\delta = -73^\circ.1$. For the distance modulus different authors give different values. For example di Benedetto (2008) estimated the distance modulus to be $\mu_0 = m - M = 19.053$, which translates to the $D_0 = 64.65$ kpc distance. While Haschke et al. (2012) estimated $D_0 = 61.5 \pm 3.4$ kpc for RR-Lyrae and $D_0 = 63.1 \pm 3.0$ kpc for Cepheids, quite compatible with values of $D_0 = 60.0$ kpc by Subramanian & Subramaniam (2012).

Alike the distance, the mass of the SMC is another important parameter, which is again not estimated exactly. The systematic uncertainty on this relevant quantity is at least of about a factor of 2. Bekki & Chiba (2009) investigated structural, kinematic, and chemical properties of stars and gas in the Small Magellanic Cloud interacting with the Large Magellanic Cloud (LMC) and the Galaxy based on a series of self-consistent chemodynamical simulations. Their "fiducial" model mass estimate is $M_{SMC} = 1.0 \times 10^9 M_\odot$ within 5 kpc of the SMC center. From other side, having in mind previously reported values of the SMC luminosity this correspond roughly to a mass-to-light ratio within the range $M/L_V \approx 2 - 3$. It is important to stress that McConnachie (2012) reports $M_{SMC} = 4.6 \times 10^8 M_\odot$ and that Bekki & Stanimirović (2009) consider the range for the mass-to-light ratio to be $M/L_V \approx 2 - 4$ assuming $4.3 \times 10^8 L_\odot$ stellar luminosity. Another estimates for SMC total stellar mass was suggested by Stanimirović et al. (2004) to be $1.8 \times 10^9 M_\odot$ (within 3 kpc of the SMC center). Similar values have been derived previously by Hindman (1967) ($1.5 \times 10^9 M_\odot$ within central 2.6 kpc) and by Gardiner et al. (1994) ($\sim 2.0 \times 10^9 M_\odot$). However we are tend to believe, that value of the SMC mass given by Bekki & Chiba (2009) is reasonable, and we have used it in our calculations.

The dynamical mass of the SMC has also been object of several investigations. Stanimirović et al. (2004) report $2.4 \times 10^9 M_\odot$ for SMC total dynamical mass within 3 kpc. In

their investigations Harris & Zaritsky (2006) estimate the value to be $1.4-1.9\times10^9 M_\odot$ within 1.6 kpc, and less well constrained mass within 3 kpc between $2.7 - 5.1 \times 10^9 M_\odot$. The difference between dynamical and stellar masses therefore suggests the dark matter component even in the innermost SMC regions. This topic is discussed in Bekki & Stanimirović (2009).

2MASS, OGLE-II and, more recently, OGLE-III data set have been extensively used to constrain the spatial structure of the SMC. In their investigations Zaritsky et al. (2000); Harris & Zaritsky (2004) concluded that SMC old stellar population forms spherical distribution. The same result was derived by Dopita et al. (1985) from PN observations and Hardy et al. (1989) from C star observations. They found that older stellar component in the central SMC region has the kinematics of a spheroidal component, with no significant rotation. In their recent work Subramanian & Subramaniam (2009, 2011, 2012) investigated red clump stars and the RR Lyrae stars, which represent the intermediate-age and the old stellar populations of a galaxy. This stellar populations clearly show slightly ellipsoidal distribution with elongation from NE-SW. They also estimated an axes ratio of 1:1.33:1.61 with a 2.6° inclination of the longest axis with the line of sight and position angle of the projection of the ellipsoid on the sky is 70.2°. The density profile is well fitted by 3D King's profile King (1962, 1966) with the tidal radius fixed at 7 kpc. Crowl et al. (2001) mapped the distances of star clusters using red clump magnitudes. They concluded that the SMC has axial ratios of 1:2:4, and is viewed almost pole on. While different authors have found a range of other axial ratios using different types of tracers, most authors agree that the SMC has a considerable line-of-sight depth. The line-of-sight depth is one of the most important parameters for microlensing purposes. We recall that the value estimated by Subramanian & Subramaniam (2011, 2012) is smaller then one given in Nidever et al. (2011) (their estimate for SMC extent is 10.6°, which, taking into account the distance of the SMC center to be order of $\sim$ 61.0 kpc, translates into $\sim$ 12 kpc). Specifically, for the 1σ depth, for the line of sight through the SMC center, Haschke et al. (2012) estimated value of σ = 4.3 kpc, which is in good agreement

with more recent average values by Subramanian & Subramaniam (2012) and Kapakos & Hatzidimitriou (2012), respectively $\sigma = 4.57 \pm 1.3$ kpc and $\sigma = 5.3 \pm 0.4$ kpc.

On the contrary, younger stellar component is highly asymmetric and irregular, giving evidence for the severe impact of the SMC during its close encounter with the LMC some 0.2 to 0.4 Gyr ago. Maragoudaki et al. (2001); Gonidakis et al. (2009), analysis show that younger stellar population resides in the disk-like structure and we assume it to has an exponential profile, with 0.66 kpc scale length, 0.3 kpc scale height and 0.6 ellipticity parameter. As for spatial orientation of young star disk, there are several estimations. For instance, the inclination angle of the disk was estimated to be $73 \pm 4^\circ$ by Kunkel et al. (2000) and $70 \pm 3^\circ$ by Caldwell & Coulson (1986).

The ratio in mass of the two stellar components, despite an indication in Harris & Zaritsky (2004) that about half of the SMC star should belong to the OS, is not very well constrained. In their analysis Bekki & Chiba (2009) give the following mass ratio OS:YS = 6:4 for their "fiducial" model. On the contrary, Yoshizawa& Noguchi (2003) reported a larger ratio.

However our analysis are based upon the recent work of Haschke et al. (2012). In particular, Haschke et al. (2012) address the issue of the three dimensional SMC structure based on the analysis of RR-Lyrae stars and Cepheids as tracers of the old and young populations, respectively. The Fig. 2.5 exhibits RR-Lyrae and Cepheids population densities as a function of distance and right ascension α (upper left panel), function of distance and declination δ (lower panel) and 3-D representation of an isodensity contour. With respect to the north direction, the value of the position angle is fixed at 66° and 83° for the YS and OS populations, respectively. The YS are strongly inclined by an angle of 74° with the north-east part nearer to us, while the OS population show almost no inclination. This later result is consistent with one by Subramanian & Subramaniam (2012). As for line-of-sight depth they estimated 4.2 kpc and in the range 5.4-6.2 kpc for the old and young populations, respectively.

We have constructed SMC old and young population density profiles coherent to the

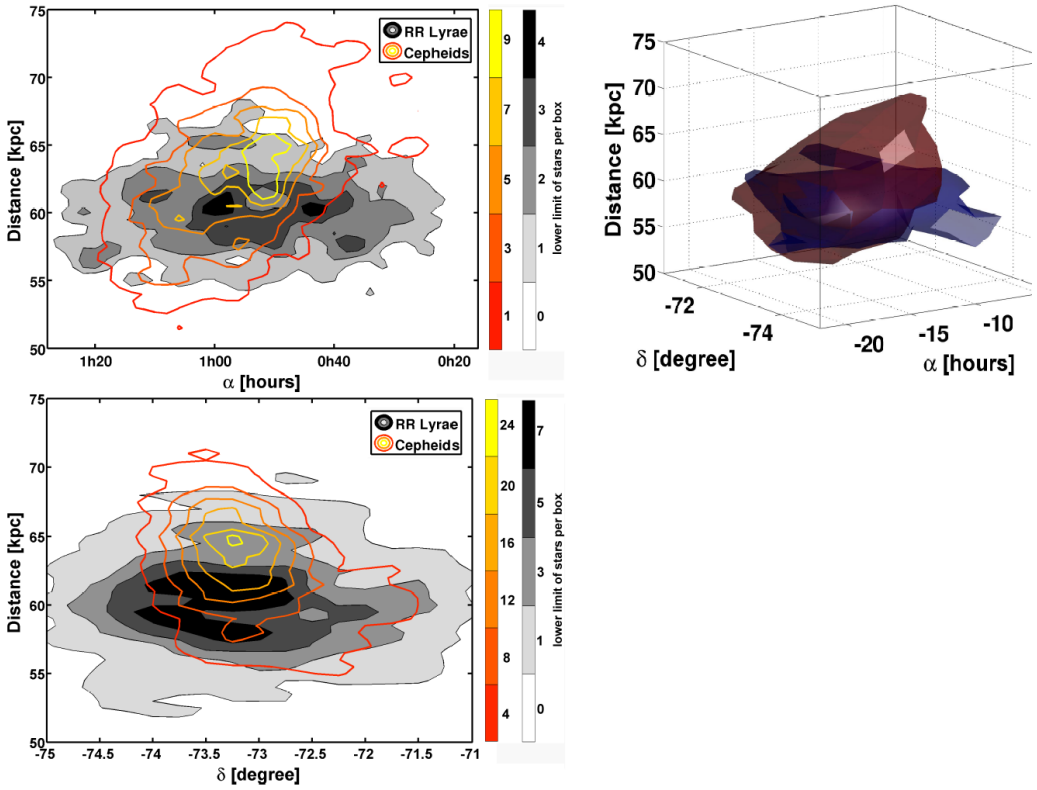

Figure 2.5: The picture of the SMC. Stellar densities of RR Lyrae stars (filled grey contours) and Cepheids (colored contours) as a function of distance and right ascension α in the upper panel and as a function of distance and declination δ in the lower panel. The upper right panel shows a three-dimensional representation of an isodensity contour of the RR Lyrae stars (blue) and Cepheids (red) as a function of right ascension α, declination α, and distance. The distributions of the old and young stars have a very different orientation in the SMC. While the RR Lyrae form a attended disk-like structure and are not inclined, the Cepheids show a large inclination angle. The picture is taken from Haschke et al. (2012).

Haschke et al. (2012) results. All the important parameters in those profiles, such as a scale lengths along the principal axis for each component and fixed central density values are given in Chapter 4.

2.2.2 Kinematics

We consider the velocity of SMC lenses as due to the sum of a non-dispersive component and a dispersive component. For the systemic proper motion we follow the analysis of Kallivayalil et al. (2006) with $(\mu_W, \mu_N) = (1.16, 1.17)\ mas\ yr^{-1}$ (in acceptable agreement with the outcome of the analysis of Piatek et al. (2008), with an observed line-of-sight velocity 146 $km\ s^{-1}$ (Harris & Zaritsky, 2006). The disk-like YS are assumed to show a rotation velocity linearly increasing to 60 $km\ s^{-1}$ with a turnover radius at 3 kpc (Stanimirović et al., 2004). For the dispersive velocity component we hypothise an isotropic Gaussian distribution (Harris & Zaritsky, 2006) (they report the line-of-sight velocity distribution to be well characterized by a Gaussian with a velocity dispersion profile independent from the position). For the velocity dispersion values we, again, follow those of the "fiducial" model of Bekki & Chiba (2009), with $\sigma = 30$ km/s for the OS and $\sigma = 20$ km/s for the YS. This is in good agreement with $\sigma = 27.5$ km/s for the old populations stars analyzed in Harris & Zaritsky (2006) and with the analysis of Evans & Howarth (2008).

Chapter 3

Gravitational Lensing.

3.1 Introduction

In 1704, Sir Isaac Newton has written: ”Do not Bodies act upon Light at a distance, and by their action bend its Rays, and is not this action strongest at the least distance?”. The calculation of the bending of the light by a spherical body of mass M was calculated by Henry Cavendish in 1784. He assumed light corpuscles move like ordinary material particles and calculated the deflection angle to be

$$\tilde{\alpha} = \frac{2GM}{rc^2} = \frac{R_s}{r} \tag{3.1}$$

provided the photon's speed is c at infinity and its closest distance r from the center of the body is much larger then R_s, which is the Schwarzschild radius of the body.

Moreover the same calculation was done by the Bavarian astronomer Johann von Soldner in 1801, and the final conclusion was that if the effect exist at all, than it is practically negligible on account of the accuracy with which angles could be measured at that time.

In 1907 Albert Einstein raised the question of the light deflection. Finally in 1915, in

possession of his field equation, he noted that space curvature doubles the bending angle, so

$$\tilde{\alpha} = \frac{2R_s}{r} \tag{3.2}$$

the so-called Einstein angle. Eq. 3.2 was later verified by VLBI (Very-Long-Baseline Interferometry) within an accuracy of 1σ.

Since than, several physicists realized that light deflection may lead to multiple images and changes of apparent brightness. However, the observability of this effect was considered very unlikely. In 1937 in two remarkable papers Fritz Zwicky (Zwicky, 1937a,b) considered the possible astronomical importance of gravitational light bending by external galaxies and concluded that "the probability that nebulae which act as gravitational lenses will be found becomes practically a certainty" (the confirmation of this prediction was done in 1979 when Walsh et al. 1979 interpreted a "double quasar" as a pair of images of one quasar. Later, A. Stockton and P. Young et al. identified the lensing galaxy). The effects of gravitational lensing of stars were revisited in a galactic and extragalactic context starting from 1964, thanks to the works of Liebes (Liebes, 1964), Refsdal (Refsdal, 1964) and Chang (Chang & Refsdal, 1979). In particular, they observed that the measured brightness of an image of a lensed cosmological source varies with time as a star lens passes near the line of sight between the observer and the source. The variation of the brightness is due to the superimposition of the unresolvable multiple images (or microimages) generated by the intervening star.

In 1986, B. Paczyński (Paczyński, 1986) pointed out the possibility of using the gravitational microlensing effect to detect massive compact objects of the Galactic halo in the direction of the Magellanic Clouds. This effect might be detected due to magnification of the flux from the background sources. As microlensing investigations showed possibility to deal with the puzzling question of the dark matter, several groups started survey programs to search for compact halo objects within the Galactic halo. The challenge for the EROS and MACHO teams was to clarify the status of the missing hadrons in our own Galaxy. In

1993, EROS (Aubourg et al., 1993), MACHO (Alcock et al., 1993) and OGLE (Udalski et al., 1993) discovered the first microlensing events in the directions of the Large Magellanic Cloud and the Galactic Center. Since these first discoveries, thousands of microlensing effects have been detected in the direction of the Galactic Center (GC) together with an events towards the Galactic Spiral Arms (GSA) and the Magellanic Clouds.

Since then Gravitational Lensing was applied to different fields of research, such as cosmological parameter estimates, search for extrasolar planets, probe of theoretical models describing the structure of the galaxies.

3.2 Gravitational lensing theory

3.2.1 Point like lenses. The lens equation

In this section we study the effect of gravitational lensing considering the simplest case, which is, the point-like lens L located nearby to the line of view to a source S (see Fig. 3.1). In the picture angle β shows the actual position of the source with respect to the optical axis, which is conveniently chosen along the lens direction, θ is the angle of the apparent position of the source image S_1, α is the angle between directions to the actual (S) and apparent S_1 positions of the source. The trajectory of the light ray is bent by an angle $\tilde{\alpha}$ due to the gravity of the lens mass. From Fig. 3.1 we see that the following relations hold:

$$\theta D_s = \beta D_s + \tilde{\alpha} D_{LS} \tag{3.3}$$

and introducing the reduced deflection angle

$$\alpha = \tilde{\alpha} \frac{D_{LS}}{D_S} \tag{3.4}$$

we get

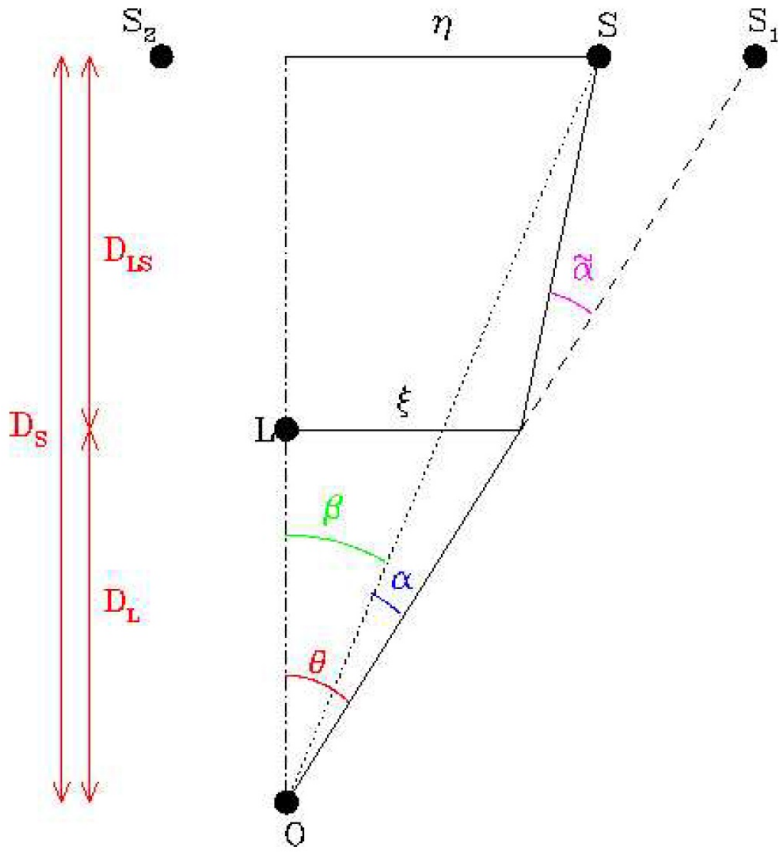

Figure 3.1: An illustration of the gravitational lensing effect geometry. All the important angles and distances are shown. Three distances D_{LS}, D_L and D_S correspond to lens-source, observer-lens and observer-source distances, respectively.

$$\beta = \theta - \alpha \tag{3.5}$$

The Eq. 3.5 is so-called lens equation and is true, when $\theta, \beta, \tilde{\alpha} \ll 1$.

As the deflection angle is given as

$$\tilde{\alpha} = \frac{4GM}{rc^2} \tag{3.6}$$

and using that minimal distance of the light ray to the lens is $r = \theta D_L$, the reduced

deflection angle results

$$\alpha = \frac{D_{LS}}{D_S D_L} \frac{4GM}{\theta c^2} \tag{3.7}$$

and hence, the lens equation 3.5 gets the following form

$$\theta^2 - \beta\theta - \theta_E^2 = 0 \tag{3.8}$$

where, the Einstein angle θ_E defined as

$$\theta_E = \frac{D_{LS}}{D_S D_L} \frac{4GM}{c^2} \tag{3.9}$$

Having fixed the position of the source (i.e $\beta = const$), one can solve an Eq. 3.8 and obtain the values of θ, that correspond to the positions of the images. It is interesting to notice that if $\beta = 0$, hence, the lens is aligned with the source, the positions of the images are symmetric with respect to the optical axis (Chwolson et al., 1924). In this case, due to this symmetry the image is a ring (Fig. 3.2) with the angular extent equal to the Einstein's angle ($\theta = \pm\theta_E$) and radius equal to $R_E = \theta_E D_L$ (Einstein radius).

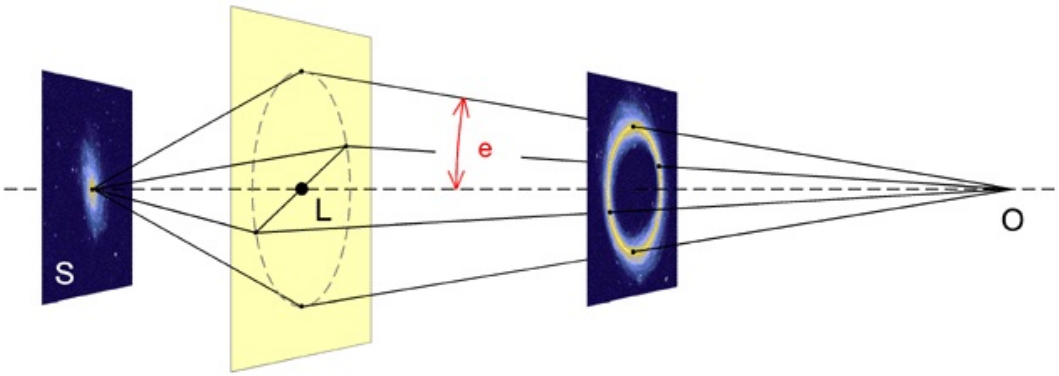

Figure 3.2: Einstein's ring formation. The observer, lens and source are aligned.

For the random position of the source the Eq. 3.8 has two solutions, therefor there will

be two images with the following position angles

$$\theta_{\pm} = \frac{\beta}{2} \pm \theta_E \sqrt{1 + \frac{\beta^2}{4\theta_E^2}} \tag{3.10}$$

The separation between two images, therefor is

$$\Delta\theta = \theta_+ - \theta_- = 2\theta_E \sqrt{1 + \frac{\beta^2}{4\theta_E^2}} \tag{3.11}$$

In some cases this separation is very small (order of microarcseconds (μas)) and the images can not be resolved, but the magnification of the emitted light is observed. For instance, lensing of the quasars by foreground galaxy stars shows angular separation of the order of microarcseconds, as the distances are order of Gpc. The origin of the therm "microlensing" concerns this small (micro scale) angular separation of the images.

3.2.2 Amplification of the flux

In Subsec. 3.2.1 we noted, that in case when the lensing concerning distances are cosmological, the angular separation of the images are not resolved, but the observed additional flux of the source is observed. The detected flux is not one emitted by source star, but the product of its surface brightness times the solid angle it subtends. Therefor, the amplification A of an image is defined as a

$$A = \frac{\mathrm{d}\Omega}{\mathrm{d}\Omega_0} = \frac{\theta\,\mathrm{d}\theta}{\beta\,\mathrm{d}\beta} \tag{3.12}$$

In other words amplification is the ratio between the solid angles of the image and the source. Using the lens equation (Eq. 3.10) we find:

$$A_{\pm} = \frac{1}{2} \pm \frac{\beta^2 + 2\theta_E^2}{2\beta\sqrt{\beta^2 + 4\theta_E^2}} \tag{3.13}$$

The total amplification is the sum of the absolute values of two image amplifications. Hence,

$$A = A_+ + \mid A_- \mid = \frac{\beta^2 + 2\theta_E^2}{\beta\sqrt{\beta^2 + 4\theta_E^2}} \tag{3.14}$$

and introducing the reduced impact factor $u = \frac{\beta}{\theta_E} = \frac{b}{R_E}$ (b is the minimum distance between lens and l.o.s.,)we get:

$$A = \frac{u^2 + 2}{u\sqrt{u^2 + 4}} \tag{3.15}$$

where b is the distance between lens and observer-source line-of-sight. From Eq. 3.15 is clear that when the lens lie on the OS line-of-sight ($\beta = 0$ and $b = 0$), the amplification is infinite, therefor an Einstein ring appears (see Fig. 3.2).

As the original flux of the source is not known, it is impossible to measure the amplification from one observation only. When the lens is moving with respect to the source line-of-sight the amplification changes, therefor the variation of the luminosity of the images can be measured.

3.2.3 The light curve

It was shown in the previous subsection that when the lens passes the line-of-sight to the source star, two images of the source are being observed with the total amplification A of the flux given by the Eq. 3.15. As the lens moves continuously with respect to the OS line-of-sight the amplification changes. This is due to the variation of the impact parameter u,

hence, the Eq. 3.15 can be written as a variable of the time

$$A(t) = \frac{u(t)^2 + 2}{u(t)\sqrt{u(t)^2 + 4}} \tag{3.16}$$

Assuming a deflector moving at a constant relative transverse speed $v_\perp$, reaching its minimum distance u_0 to the undeflected line of sight at time t_0, $u(t)$ is given by

$$u(t) = \sqrt{u_0^2 + \left(\frac{t - t_0}{t_E}\right)^2} \tag{3.17}$$

where t_0 is the time of closest approach ($u(t_0) = u_0$). The characteristic time $t_E = \frac{R_E}{v_\perp}$ is time it takes to the lens to cross the Einstein radius and describes the proper duration of the microlensing event.

Combination of the Eq. 3.16 and Eq. 3.17 leads to a time dependent amplification of the luminosity of the source. The amplification A reaches his maximum A_{max} at time t_0, when $u(t)$ approaches to u_0. It is clear that when $u_0 = 0$ than $A_{max} \to \infty$ and when $u_0 = 1$ (the minimum distance between lens and l.o.s. is an Einstein radius), $A_{max} = 1.34$. This maximum value of amplification is the threshold value for the gravitational lensing.

Fig. 3.3 represents the dependence of the source amplification from time for different values of the minimum impact parameter u_0.

The simple microlensing effect, which is point-like source and point-like lens with uniform relative motion with respect to the line of sight, has some characteristic features which allow one to discriminate it from any known intrinsic stellar variability:

• The event is singular in the history of the source (as well as of the deflector).

• The amplification of the flux is independent of the color, as the effect is pure gravitational.

• The amplification is a known function of time, depending on only following u_0, t_0, t_E, and it has symmetrical shape (Paczyński curve, see Fig. 3.3).

• The impact parameters of the events is uniformly distributed because of the source-lens

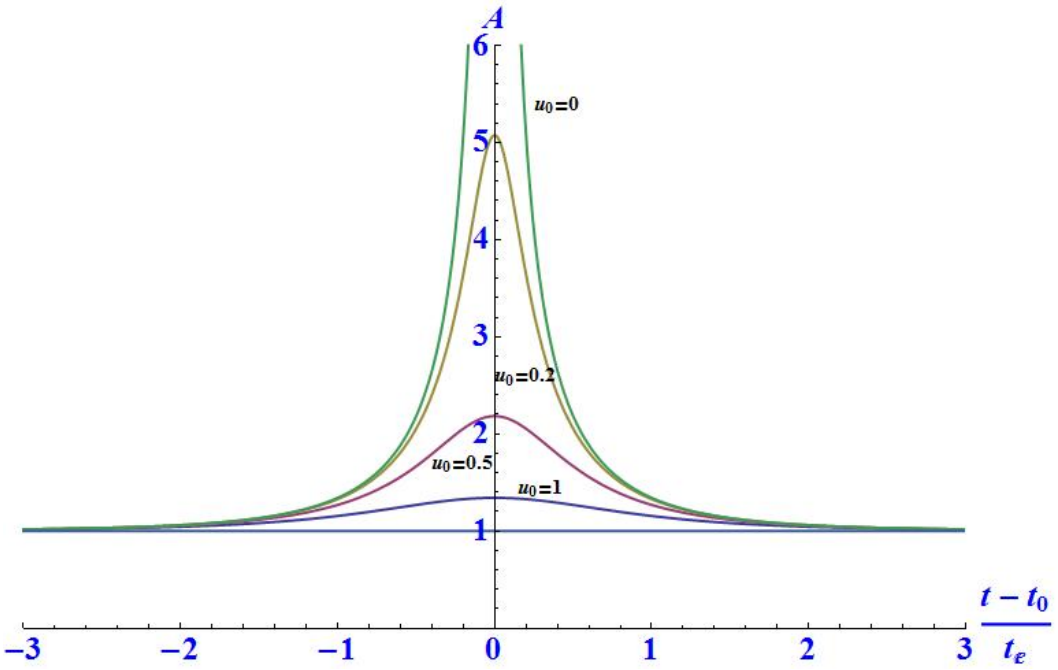

Figure 3.3: Light curve. Time evolution of the amplification for different values of the impact parameter $u_0 = 0, 0.2, 0.5, 1$ are drown.

system random geometric configuration

• The passive role of the lensed stars implies that their population should be representative of the monitored sample, particularly with respect to the observed color and magnitude distributions.

However the simple microlensing description can be broken in various ways, such as the lens may be a double system (Mao & Stefano, 1995), the source may be an extended object (Yoo et al., 2004), or the relative motion with respect to the line of sight may be nonuniform due either to the rotation of the Earth around the Sun (parallax effect) (Gould, 1992; Hardy & Walker, 1995), or to an orbital motion of the source or of the lens around the center-of-mass of a multiple system (Mollerach & Roulet, 2002). The interest of these so-called ”exotics” comes from the extra information on the lensing configuration that can be obtained in such specific cases.

3.3 Microlensing quantities

Gravitational microlensing offers the opportunity to measure the density and total mass of a population of objects - bright or dark - between a background population of sources and the observer. Paczyński (Paczyński, 1986) elaborated this idea quantitatively, and applied it to objects potentially making up the dark matter halo of the Milky Way. Such an objects of masses $10^{-6} \leq M/M_{\odot} \leq 10^{2}$ would produce time variable amplification of background stars in the Large or Small Magellanic Clouds. In this situations the most important quantities to characterize or to have a guess of an existing population are microlensing probability, event rate and timescale distribution.

3.3.1 Optical depth

One of the most important parameter of the gravitational microlensing is the optical depth τ, which is instantaneous probability to observe a microlensing event (i.e. to have a background star microlensed with the amplification higher than 1.34) and is calculated as the integrated number of lenses within the microlensing tube (with cross section given by the Einstein radius, R_E), for a given line of sight (Mao, 2012; Mollerach & Roulet, 2002). In other words the optical depth is the probability to have a lensing object within the "microlensing tube" with the line-of-sight axis and the radius of Einstein radius. Having assumed that all the lenses have the same mass m and that the number density of lenses at distance D_L is $n_L = \rho_L/m$, where ρ_L is the lens density in the distance D_L and bearing in mind that the cross section of the "microlensing tube" is πR_E^2, the differential optical depth is

$$\mathrm{d}\tau = \mathrm{d}D_L n_L \pi R_E^2 \tag{3.18}$$

and therefor

$$\tau = \int_0^{D_S} \mathrm{d}D_L \int_0^{\infty} \mathrm{d}m \frac{\mathrm{d}n_L}{\mathrm{d}m} \pi R_E^2 = \frac{4\pi G D_S^2}{c^2} \int_0^1 \mathrm{d}x \cdot x(1-x)\rho_L(x) \tag{3.19}$$

Here we used new notation x which is the ratio $\frac{D_L}{D_S}$. The optical depth depends on the lens and source spatial density, and in particular it is independent from the lens mass. As the light lenses have smaller Einstein radius and large number densities for given total mass, while the heavier lenses have larger Einstein radius and are less numerous, the two contribution compensate each other in optical depth expression.

In some cases the source distribution spread is remarkable (i. e. the extent of the source distribution is comparable with the microlensing concerning distances) and hence the need of source distribution averaging is important. In such cases the expression for τ is

$$\tau = \frac{1}{N_S} \int \mathrm{d}D_S \frac{\mathrm{d}n_S}{\mathrm{d}D_S} \tau(D_S) \tag{3.20}$$

where the normalization factor is $N_S = \int \mathrm{d}D_S \frac{\mathrm{d}n_S}{\mathrm{d}D_S}$, $\frac{\mathrm{d}n_S}{\mathrm{d}D_S}$ describe number density of the sources along given line-of-sight and $\tau(D_S)$ is defined by Eq. 3.19.

The measured optical depth associated to microlensing events observed in a population of N_{obs} stars monitored for a duration T_{obs} is given by Moniez (2010)

$$\tau = \frac{1}{N_{obs}} \frac{\pi}{2} \sum_{events} \frac{t_E}{\epsilon(t_E)} \tag{3.21}$$

where $\epsilon(t_E)$ is the average detection efficiency of microlensing events with a time scale t_E.

As we noticed the calculated optical depth does not depend on the deflector's mass function. However the measured optical depth, that takes into account the mean detection efficiency $\epsilon(t_E)$, can be biased by this mass function, in particular because the detection function vanishes for very short or very long duration events. This fact makes impossible a perfect compensation of the inefficiencies. If many deflectors are light (resp. heavy) enough to

produce extremely short (resp. long) duration events that cannot be detected, the measured optical depth will clearly be underestimated. This is why collaborations often indicate that their results are valid within a given duration domain.

3.3.2 Microlensing event rate

The optical depth is the probability of stars to be magnied above a threshold of 1.34 at any time. Observations usually measure only change of magnification. Therefore, event rate Γ is another important quantity for observations. It is the number of lenses entering in the microlensing tube per unit time for the given line-of-sight. $\mathrm{d}\Gamma$ differential event rate at which a single star is microlensed by a lensing object is (see Riffeser et al. (2006); de Rujula et al. (1991),

$$\frac{\mathrm{d}^4\Gamma}{\mathrm{d}D_L\,\mathrm{d}M\,\mathrm{d}v_t\,\mathrm{d}b} = 2\rho(D_L)\xi(M)p_{v_t}(v_t, D_L)v_t \tag{3.22}$$

where b is impact parameter, $\rho(D_L)$ is the lens mass density, $\xi(M)$ is the lens mass function, which normalized to $\int \xi(M)M\,\mathrm{d}M = 1$ (Binney & Tremaine, 1987) and $p_{v_t}(v_t, D_L)$ and v_t are lens velocity distribution and transverse velocity, respectively and the number density per lens mass interval is defined by $n(D_L, M) = \rho(D_L)\xi(M)$ (it has units of $length^{-3}mass^{-1}$). Therefore the event rate is just integral of the Eq. 3.22 over lens masses, lens distances, relative velocities, and impact parameters b smaller than a threshold $u_T R_E$, hence

$$
\begin{aligned}
\Gamma(D_S) &= \int_0^\infty \int_0^{D_S} \int_0^\infty \int_0^{u_T R_E} \frac{\mathrm{d}^4\Gamma}{\mathrm{d}D_L\,\mathrm{d}M\,\mathrm{d}v_t\,\mathrm{d}b}\,\mathrm{d}b\,\mathrm{d}v_t\,\mathrm{d}M\,\mathrm{d}D_L \\
&= 2u_T \int_0^\infty \xi(M) \int_0^{D_S} \rho(D_L) R_E(D_L, M) \int_0^\infty v_t p_{v_t}(v_t, D_L)\,\mathrm{d}v_t\,\mathrm{d}D_L\,\mathrm{d}M \\
&= 2u_T \frac{\sqrt{4G}}{c} \int_0^{D_S} \rho(D_L)\sqrt{D(D_L)} \int_0^\infty \sqrt{M}\xi(M) \int_0^\infty v_t p_{v_t}(v_t, D_L)\,\mathrm{d}v_t\,\mathrm{d}D_L\,\mathrm{d}M \\
&= u_T \Gamma_1(D_S)
\end{aligned}
\tag{3.23}
$$

The impact parameter threshold u_T is equivalent to a amplification threshold A_T. Therefore, the number of events with amplification larger than $A_T(u_T)$ is proportional to the threshold parameter u_T. $\Gamma_1(D_S)$ is the event rate along a chosen line-of-sight to a distance of D_S. Analogously to the optical depth, we also define the line-of-sight distance-averaged single-star event rate

$$
\bar{\Gamma}_{1S} = \int p_S(D_S)\Gamma_1(D_S)\,\mathrm{d}D_S \tag{3.24}
$$

The relations give the event rate per line-of-sight or per star. To compare this with measurements of the lensing rate for resolved stars, one has to account for the source density.

A quantitative compatibility of the expected and observed events may help to constrain mass function and fraction of both luminous and dark components of galaxies more accurately. This make the expected number of microlensing event N very important quantity, which is

$$
N_{ev} = N_{obs}T_{obs} \int_0^\infty \frac{\mathrm{d}\Gamma}{\mathrm{d}t_E}\epsilon(t_E)\,\mathrm{d}t_E \tag{3.25}
$$

where $N_{obs}T_{obs}$ is field exposure as defined in Alcock et al. (2000), $\frac{\mathrm{d}\Gamma}{\mathrm{d}t_E}$ is Einstein time distribution and $\epsilon(t_E)$ is the efficiency.

3.3.3 Distribution for the Einstein Time

Another important observable in microlensing surveys is the duration of the event. The distribution $\frac{\mathrm{d}\Gamma}{\mathrm{d}t_E}$, the differential rate of microlensing events with respect to the Einstein time t_E, allows one to estimate the expected typical duration and the expected number of the microlensing events. Having calculated the typical duration of the events of given population, one may have an idea about position of the lens (Mancini et al., 2004). It is because, as the duration of the event is one of few observable of microlensing event, hence, is known, it is possible to guess the belongance of the lens to some known population along observer-source line-of-sight (with some probability). The distribution of the Einstein time of the events (see Riffeser et al. (2006); Han & Gould (1996)) is

$$\frac{\mathrm{d}^2\Gamma}{\mathrm{d}t_E\,\mathrm{d}u_0} = \frac{2}{t_E^3}\int_0^\infty\int_0^{D_S}\rho(D_L)\xi(M)p_{v_t}(\frac{R_E}{t_E})R_E^3\,\mathrm{d}D_L\,\mathrm{d}M \tag{3.26}$$

If one carries out an experiment with a threshold u_T, one obtains with Eq. 3.26 the Einstein timescale distribution of events as

$$\frac{\mathrm{d}\Gamma_T}{\mathrm{d}t_E} = \frac{2u_T}{t_E^3}\int_0^\infty\int_0^{D_S}\rho(D_L)\xi(M)p_{v_t}(\frac{R_E}{t_E})R_E^3\,\mathrm{d}D_L\,\mathrm{d}M \tag{3.27}$$

(Roulet & Mollerach, 1997; Baltz & Silk, 2000; Riffeser et al., 2006).

The normalized probability distribution for the Einstein time becomes

$$P(t_E) = \frac{1}{\Gamma_T}\frac{\mathrm{d}\Gamma_T}{\mathrm{d}t_E} \tag{3.28}$$

Having Eq. 3.28 for probability distribution the average timescale $\bar{t}_E$ of an event with D_S line-of-sight distance, one can obtain (Alcock et al., 1995)

$$\bar{t}_E(D_S) = \frac{2}{\pi\Gamma_1}\int_0^\infty\int_0^{D_S}\rho(D_L)\xi(M)\pi R_E^2\,\mathrm{d}D_L\,\mathrm{d}M = \frac{2}{\pi}\frac{\tau(D_S)}{\Gamma_1(D_S)} \tag{3.29}$$

Here, as usual $\tau(D_S)$ is the optical depth and $\Gamma_1(D_S)$ is the event rate along a chosen line-

of-sight to a distance of D_S. The Eq. 3.29 describe the relationship between optical depth, event rate and average timescale of the event. So, if one calculate the expected event rate and optical depth, one can estimate the expected duration of that event, and hence, to compare with the observed one.

3.3.4 The Transverse Lens-source Velocity Distribution

As we noticed in previous subsections, the microlensing event rate is one of the most important quantities in microlensing research. Eq. 3.23 shows that event rate depends not only on mass function and density profile, but also on velocity distribution of the lenses and sources. Different authors have describe the velocity distribution with different profile, such as Maxwellian (Calchi Novati et al., 2006; Han & Gould, 1995) or Gaussian (Riffeser et al., 2006) profiles or with the new set of Gauss-Hermite moments (Gerhard, 1993; van der Marel & Franx, 1993).

However, we discuss here Gaussian velocity profile both for the lens and source populations in their proper reference frame.

Firstly we introduce the geometry of the microlensing tube section in the plane orthogonal to the line-of-sight to the source in Fig. 3.4. The ω is the angle between lens relative velocity $v^{\perp}$ and normal to the surface and the angle α is the angle between normal to the surface and $\boldsymbol{l}$ direction. The function $\boldsymbol{p}$ in Eq. 3.23 describes relative velocity distribution. Let as consider the observer and source move with the $\boldsymbol{v_S}$ and $\boldsymbol{v_O}$ velocities (those velocities are components of the space velocities perpendicular to the line-of-sight, as parallel components are not important in microlensing effect), respectively. It is easy to see that that the microlensing tube moves with the velocity

$$\boldsymbol{v_t = x v_S + (1 - x) v_O} \tag{3.30}$$

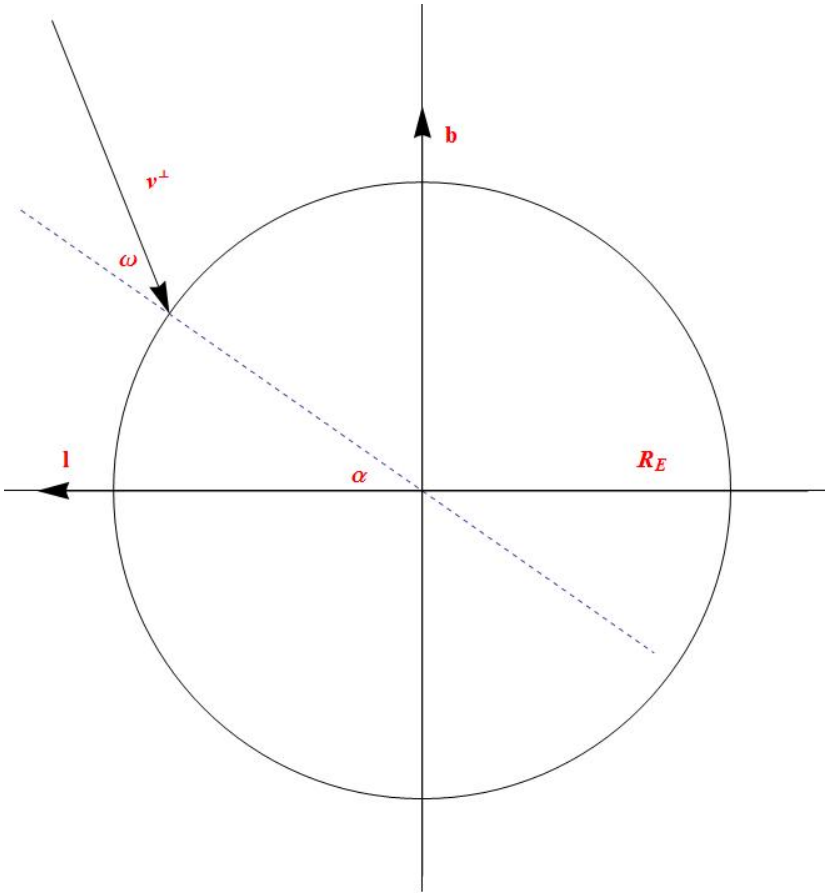

Figure 3.4: Geometrical representation of the microlensing tube section in a orthogonal plane to the line-of-sight to the source. Relevant angles and $v^{\perp}$ velocity are drown too. The $\boldsymbol{l}$ and $\boldsymbol{b}$ corresponds to the directions of increasing longitudes and latitudes, respectively.

where $\boldsymbol{x = D_L/D_S}$. If $\boldsymbol{v_L}$ is the lens velocity in the same reference frame, than the lens relative velocity with respect to the microlensing tube is

$$\boldsymbol{v = v_L - v_t} \tag{3.31}$$

All velocities [1] may be introduced as a composition of two components, bulk motion velocity $\boldsymbol{v_{bulk}}$ and so-called distributive velocity $\boldsymbol{v_{dis}}$ (we assume to be Gaussian distributed)

[1]The velocities $\boldsymbol{v^{\perp}}$, $\boldsymbol{v_t}$, $\boldsymbol{v_L}$, $\boldsymbol{v_S}$, $\boldsymbol{v_O}$ are vectors. Later on we present those velocities in a form of the sum of two components, projected onto $\boldsymbol{l}$ and $\boldsymbol{b}$.

and taking into account 3.31 we obtain

$$v_{bulk} = v_{L,bulk} - xv_{S,bulk} - (1-x)v_O \tag{3.32}$$

and

$$v_{dis} = v_{L,dis} - xv_{S,dis} \tag{3.33}$$

The $v^{\perp}$ component of the v can be written $v^{\perp} = v^l l + v^b b$. In order to obtain velocity distribution function, we firstly write dispersive component of the velocity, which is Gaussian

$$G(v^i_{dis}) = \frac{1}{\sqrt{2\pi}\sigma^i} Exp\left[-\frac{(v^i_{dis})^2}{2(\sigma^i)^2}\right], \tag{3.34}$$

where $i = l, b$ and σ^i are the corresponding velocity dispersions. If the lenses and the sources have σ^i_L and σ^i_S respectively, than the relative velocity dispersion is

$$\sigma^i = \sqrt{(\sigma^i_L)^2 + (x\sigma^i_S)^2} \tag{3.35}$$

From Fig. 3.4 one may obtain distributive component of the velocity in therm of the modulus of the orthogonal relative velocity $v^{\perp}$ (recall that $t_E = \frac{R_E}{v^{\perp}}$)

$$v^l_{dis} = -v^l_{bulk} - v^{\perp}\cos\gamma \tag{3.36}$$

$$v^b_{dis} = -v^b_{bulk} - v^{\perp}\sin\gamma \tag{3.37}$$

where $\gamma \equiv \omega + \alpha$. The velocity distribution p can be obtained by substituting corresponding values of the v^l_{dis} and v^b_{dis} from Eq. 3.36 and Eq. 3.37 into 3.34 and taking into account that

$$p = G(v^l_{dis})G(v^b_{dis})\,\mathrm{d}v^l_{dis}\,\mathrm{d}v^b_{dis} \tag{3.38}$$

3.3.5 Mass distribution

As we saw in subsection 3.3.2 the microlensing event rate depends on mass function. Let as to discuss in details objects mass distribution, that acts as a lenses. We assume, that the lens mass distribution is independent of the spatial distribution (factorization hypothesis) and, hence we can write

$$\frac{\mathrm{d}n}{\mathrm{d}\mu}\,\mathrm{d}\mu = \frac{\mathrm{d}n_0}{\mathrm{d}\mu}\frac{\rho_l}{\rho_{0,l}}\,\mathrm{d}\mu \tag{3.39}$$

where ρ_l and $\rho_{0,l}$ are lens density and local density, respectively μ is the lens mass in units of solar mass and $\frac{\mathrm{d}n_0}{\mathrm{d}\mu}$ is the mass function and has the following form

$$\frac{\mathrm{d}n_0}{\mathrm{d}\mu} = const \cdot \mu^{-\alpha} \tag{3.40}$$

where the classical value of $\alpha = 2.35$ is given by Salpeter (1955). In case, when lens mass range is (μ_0, μ_1), than mass function is normalized as

$$\int_{\mu_{sup}}^{\mu_{inf}} \frac{\mathrm{d}n_0}{\mathrm{d}\mu}\,\mathrm{d}\mu = \frac{\rho_{0,l}}{M_\odot} \tag{3.41}$$

Sometimes it is useful to assume that all the lenses have the same mass μ_0. In this case the mass distribution can be described by delta function

$$\frac{\mathrm{d}n_0}{\mathrm{d}\mu} = \frac{\rho_{0,l}}{M_\odot \mu_0}\delta(\mu - \mu_0) \tag{3.42}$$

However Kroupa (2001) kept $\alpha = 2.3$ above $0.5M_\odot$, but introduced $\alpha = 1.3$ for mass

range (0.08-0.5)$M_{\odot}$ and $\alpha = 0.3$ below $0.08M_{\odot}$. In such a cases, when the mass functions are given with the different slopes (see also, for example Gould et al. (1997)), than normalization may be obtained by

$$const_1 \int_{\mu_{sup}}^{\mu_c} \mu^{1-\alpha_1}\, d\mu + const_2 \int_{\mu_1}^{\mu_2} \mu^{1-\alpha_2}\, d\mu + const_3 \int_{\mu_3}^{\mu_{inf}} \mu^{1-\alpha_3}\, d\mu = \frac{\rho_{0,l}}{M_{\odot}} \qquad (3.43)$$

There are large uncertainties concerning the sub-stellar region. In particular, the classical assumption of a single initial mass function (IMF) covering the whole sub-stellar and stellar mass range is being questioned in favor of a two-component IMF to account for possible different formation modes of sub-stellar objects. I.e. one IMF covering brown dwarfs and very-low-mass stars on the one hand, and another ranging from the higher-mass brown dwarfs to the most massive stars on the other.

Chapter 4

Microlensing towards the SMC: a new analysis of OGLE and EROS results[1].

4.1 Introduction

The original motivation for stellar microlensing (Paczyński, 1986) is the search for dark matter candidates in form of (faint) massive compact halo objects (MACHOs) in the galactic halos. Indeed, over a broad mass range of the putative MACHO population, our current understanding of this relevant astrophysical issue is mainly based on the results of the observational microlensing campaigns carried out to this purpose. On the other hand, the current understanding for the nature of most, if not all, dark matter at the Galactic level is from some yet undiscovered particle (Strigari, 2012) (for a general discussion of dark matter and gravitational lensing we refer to (Bartelmann, 2010; Massey et al., 2010)). The probability for a microlensing event to occur is extremely small. This is described in term of the microlensing *optical depth* which is of the order of $\mathbf{10^{-6}}$ or smaller (we refer to Mao (2012) and references therein for an updated introduction to microlensing), therefore dense stellar fields have to be monitored to increase the rate of events. Microlensing campaigns for the search of MACHOs have been carried out towards the Magellanic Clouds (Moniez, 2010) and M31

[1]This chapter is submitted to the MNRAS.

(Calchi Novati, 2010). Besides the dark matter issue, meanwhile microlensing has become an established tool for analyses of stellar astrophysics (Gould, 2001) and, through observations towards the Galactic bulge, for the search of extra-solar planets Dominik (2010).

The Magellanic Clouds (Large and Small), located within the Galactic halo, are a privileged target for the search of microlensing events. Up to now about 20 candidate events have been reported towards these lines of sight and important, though not always coherent, results have been reported. There is an agreement to exclude MACHOs as viable dark matter candidates for masses below $\approx$ $\mathbf{(10^{-1} - 10^{-2})\ M_{\odot}}$ (down to about $\mathbf{10^{-7}\ M_{\odot}}$). Some debate remains in the mass range $\mathbf{(0.1 - 1)\ M_{\odot}}$ where, according to some observational outcomes, a sizable fraction, if not most of the halo mass, may indeed be in form of compact halo objects. For larger values of the MACHO mass (where the expected number of events decreases) the limits obtained with microlensing analyses are weaker than with other techniques (Yoo et al., 2004; Quinn et al., 2009; Quinn & Smith, 2009); in this mass range it appears to be useful also to consider the cross-matching of microlensing with X-ray catalogues (Sartore & Treves, 2010, 2012). The event duration, the "Einstein time" $\boldsymbol{t_{\mathrm{E}}}$, the main physical observable for microlensing events, is driven by the lens mass, $\boldsymbol{m}$, scaling as $\boldsymbol{\sqrt{m}}$ (though it also depends from other non directly observable quantities as the lens-source relative transverse velocity and the lens and source distances). The coincidence of the mass range $\mathbf{(0.1 - 1)\ M_{\odot}}$ with that of (faint) stars that may act as lenses may suggest some bias in the analysis leading to underestimate the contribution to the signal from these lens populations (or, if not the case, it may have some deeper, still to be understood, astrophysical implications). A possibly non exhaustive list of potential lens populations, to which we broadly refer to as "self lensing" as opposed to MACHO lensing populations, includes lenses belonging to the luminous components of the SMC, which act also as sources, and the disc of the MW (in fact, we will consider also non-luminous lenses belonging to these populations moving down to the sub-stellar mass range to include also brown dwarfs). The suggestion that the events

observed towards the Magellanic Clouds may not be due to MACHOs dates back at least to the analyses of Sahu (1994), Wu (1994), Gould (1995) and has been thereafter the object of several analyses (Salati et al., 1999; Di Stefano, 2000; Evans & Kerins, 2000; Gyuk et al., 2000; Jetzer et al., 2002). It is therefore relevant to reliably determine the signal expected from self-lensing lens populations as compared to that of MACHO lensing.

More specifically, the MACHO collaboration claimed for a mass halo fraction in form of $\sim \mathbf{0.5}\,\mathrm{M}_\odot$ MACHOs of about $f \sim 20\%$ out of observations of 13-17 candidate microlensing events towards the LMC (Alcock et al., 2000), a result further discussed in Bennett (2005) where in particular the microlensing nature of 10-12 out of the original set of 13 candidate events has been confirmed. On the other hand, in disagreement with this result, the analyses of the EROS (Tisserand et al., 2007), and the OGLE collaboration, for both OGLE-II (Wyrzykowski et al., 2009, 2010) and OGLE-III (Wyrzykowski et al., 2011a,b), out of observations towards both the LMC and SMC, concluded by putting extremely severe *upper* limits on the MACHO contribution also in this mass range. In particular, at 95% CL, the EROS collaboration reported an upper limit $f = 8\%$ for $\mathbf{0.4}\,\mathrm{M}_\odot$ MACHOs, and OGLE $f = 6\%$ for $\mathbf{0.4}\,\mathrm{M}_\odot$ MACHOs and $f = 4\%$ in the mass range between $\mathbf{0.01}$ and $\mathbf{0.15}\,\mathrm{M}_\odot$.

Rather than addressing, as also we mainly do in the present work, the issue on the *lens* nature, whether self lensing or MACHO lensing, one may also consider different *source* populations which may possibly enhance the microlensing rate (see for instance Rest et al. (2005) and reference therein for a broad overall discussion of the different possible source and lens populations). For the specific case of the LMC, recently Besla et al. (2013) proposed, as possible sources, a SMC stripped population (still to be observed, though) lying *behind* the LMC, which may explain simultaneously both the MACHO and the OGLE observational results towards the LMC (see however Nelson et al. (2009) which, on a general ground, concluded against the possibility for the sources to lie behind the LMC).

With respect to the LMC, the case of the SMC is somewhat peculiar. As further dis-

cussed below, the SMC is quite elongated along the line of sight. As the microlensing cross section, the Einstein radius, is proportional to the (square root of) the source-lens distance, an elongated structure is expected to enhance the SMC self-lensing signal. As a result, the ratio of self lensing versus MACHO lensing (if any) is larger than towards the LMC making overall more difficult to disentangle the two signals and to draw stringent conclusions on the issue of MACHOs. On the other hand, the characteristics that differentiate the two lines of sight can be considered as a strength when cross-matching the results.

In previous analyses we have addressed the issue of the nature of the reported events towards the LMC by the MACHO (Mancini et al., 2004; Calchi Novati et al., 2006) and the OGLE collaboration (Calchi Novati et al., 2009; Calchi Novati & Mancini, 2011). In this paper we report a detailed analysis of the EROS and the OGLE observational campaigns towards the SMC (as further discussed below, we do not include data from the observational campaign carried out by the MACHO collaboration along this line of sight). The underlying idea behind our approach is to characterize statistically, starting from a reliable model for all possible lens populations, the observed versus the expected signal in order to address the issue of the nature of the reported microlensing candidate events. First, we evaluate profiles of the optical depth, in particular for SMC self lensing. This tells us how the SMC structure is reflected in the expected microlensing signal and carries information on the overall spatial density of the given lens population. To include within the analysis the specific characteristics of the observed events, in particular number, position and duration, we carry out an investigation based on the microlensing rate which then allow us to derive limits on the halo mass fraction in form of MACHOs.

The plan of the paper is as follows. In Section 4.2 we describe the models used in our analysis, with a particular attention to the SMC structure. In Section 4.3 we resume the status and the results of previous and ongoing microlensing campaign towards the SMC. In Section 4.4 we present our analysis. In Section 4.4.1 we present the profiles of the optical

depth. In Section 4.4.2 we introduce the microlensing rate, our main tool of investigation. In Section 4.4.3 we derive the expected microlensing quantities, number of events and duration. In Section 4.4.4 we address the issue of the possible nature of the reported observed events and in particular we evaluate the limits on dark matter in form of compact halo objects. In Section 4.5 we compare our results to previous ones towards the SMC and critically analyze, as for the search of MACHOs, the line of sight towards the SMC against that towards the LMC. Finally, in Section 4.6 we present our conclusions.

4.2 Model

The microlensing quantities, the microlensing optical depth and the microlensing rate, depend on the underlying astrophysical model. In particular, the optical depth depends uniquely from the lens (and source) population spatial density, whereas the microlensing rate depends also from the lens mass function and the lens-source relative velocity. Indeed, for the more common situation of a point-like single lens and source with uniform relative motion, the only physical observable characterizing the events is the Einstein time, $t_{\mathbf{E}}$, which is a function of the lens mass, the lens-source relative velocity and the lens and source distances. None of these quantities, however, is directly observable. The underlying astrophysical models are therefore essential to assess the characteristics of the expected signal from all the possible lens populations. In the present case: self lensing, which fixes the background level, and MACHO lensing, the "signal" we want to constraint.

In the following analysis we consider, as possible lens populations, SMC and MW stars (and brown dwarfs), both contributing to the self-lensing signal, and the would be population of compact halo objects in the MW halo, which we describe in turn.

4.2.1 The SMC: structure and kinematics

4.2.1.1 Structure

The SMC is a dwarf irregular galaxy orbiting the MW in tight interaction with the (larger) LMC (van den Bergh, 1999; McConnachie, 2012). Also because of this complicated dynamical situation, the detailed spatial structure and overall characteristics of the SMC are still debated. For the overall SMC *stellar* mass, which is a quantity of primary importance to our purposes, being in the end (almost) directly proportional to the SMC optical depth and number of expected events, we use $\boldsymbol{M_* = 1.0 \times 10^9\ M_\odot}$ (within **5 kpc** of the SMC center), which is the value of the "fiducial" model of Bekki & Chiba (2009) (see also Yoshizawa& Noguchi 2003). According to reported values of the SMC luminosity this correspond roughly to a mass-to-light ratio within the range $\boldsymbol{M/L_V \sim 2-3}$. We recall that McConnachie (2012) reports $\boldsymbol{M_* = 4.6 \times 10^8\ M_\odot}$, which is half smaller than our fiducial value, and that Bekki & Chiba (2009), for a stellar luminosity $\boldsymbol{4.3 \times 10^8\ L_\odot}$, consider the "reasonable" range for the mass-to-light ratio to be $\boldsymbol{M/L_V \sim 2-4}$, depending in particular on the fraction of the old stellar population. In a previous work, Stanimirović et al. (2004), for a stellar luminosity $\boldsymbol{3.1 \times 10^8\ L_\odot}$, estimated a total stellar mass of the SMC $\boldsymbol{1.8 \times 10^9\ M_\odot}$ (within **3 kpc** of the SMC centre). *Overall, the systematic uncertainty on this relevant quantity we find in literature is of about a factor of 2, with our chosen value lying rather near the upper viable limit*.

The total *dynamical* mass of the SMC has also been the object of several investigations. Stanimirović et al. (2004) report $\boldsymbol{2.4 \times 10^9\ M_\odot}$ within **3 kpc**, a result confirmed in Harris & Zaritsky (2006) who report values in the range $\boldsymbol{1.4-1.9 \times 10^9\ M_\odot}$ within **1.6 kpc** and a less well constrained mass within **3 kpc** between 2.7 and $\boldsymbol{5.1 \times 10^9\ M_\odot}$. These values therefore suggest the existence of a dark matter component even in the innermost SMC region, as thoroughly discussed in Bekki & Stanimirović (2009).

According to the star formation history of the SMC (Harris & Zaritsky, 2004) we can

broadly distinguish two components: an old star (OS) and a young star (YS) population. Several analyses have shown that indeed, besides their age, these populations also show different morphology structures. We base our analysis upon the recent work of Haschke et al. (2012), which in turn is based on the OGLE-III SMC variable stars data but see also, among others, Kapakos & Hatzidimitriou (2012); Nidever et al. (2011); Subramanian & Subramaniam (2009, 2012). In particular, Haschke et al. (2012) address the issue of the three dimensional SMC structure based on the analysis of RR Lyræ stars and Cepheids as tracers of the old and young populations, respectively. Haschke et al. (2012) report estimates for the position and the inclination angles and for the line of sight depth which is a crucial quantity to microlensing purposes as the microlensing cross section, and in the end the microlensing rate, grows with the lens-source distance, so that a large SMC intrinsic depth enhances the SMC self-lensing signal whereas, on the other hand, the details of the inner SMC structure are not essential to determine the expected lensing signal for the MW lens populations (Section 4.4.1). Moreover, Haschke et al. (2012) show contour plots for the stellar density of RR Lyræ stars and Cepheids not only on the plane of the sky but also on the distance-declination and the distance-right ascension planes. For fixed values of the position and inclination angles and line of sight depth we therefore build our model trying to broadly match this full three dimensional view of the SMC.

As a model for both populations we choose a spheroidal structure with a fully Gaussian profile for the YS population

$$\rho_{\mathbf{SMC}}^{(YS)} = \rho_{\mathbf{0}}^{(YS)} \exp\left[-\frac{1}{2}\left(\left(\frac{\xi}{\sigma_\xi}\right)^2 + \left(\frac{\eta}{\sigma_\eta}\right)^2 + \left(\frac{\zeta}{\sigma_\zeta}\right)^2\right)\right] . \tag{4.1}$$

For the OS population we keep the Gaussian profile along the line of sight (which in particular ensures a roughly constant line of sight depth), and a smoother exponential profile in the

orthogonal plane

$$\rho_{\rm SMC}^{(OS)} = \rho_0^{(OS)} \exp\left[-\sqrt{\left(\frac{\Xi}{\Xi_0}\right)^2 + \left(\frac{\Upsilon}{\Upsilon_0}\right)^2}\right] \exp\left[-\frac{1}{2}\left(\frac{Z}{\sigma_Z}\right)^2\right] . \quad (4.2)$$

With respect to the north direction, the value of the position angle is fixed at **66°** and **83°** for the YS and OS populations, respectively. The YS are strongly inclined by an angle of **74°** with the north-east part nearer to us. The OS, on the other hand, do not show an inclination significantly different from zero. We assume therefore a zero inclination angle also in agreement with the analysis of Subramanian & Subramaniam (2012). The line of sight depth is **4.2 kpc** and in the range **5.4 − 6.2 kpc** for the old and young populations, respectively. These values are as reported in the analysis of Haschke et al. (2012) to which we also refer for a critical discussion of previous analyses. The reference frames (ξ, η, ζ) and (Ξ, Υ, Z) are directed along the principal axes of the YS and OS spheroid, respectively. For the YS population we fix $(\sigma_\xi, \sigma_\eta, \sigma_\zeta) = (0.8, 3.5, 1.3)$ **kpc**, for an overall elongated bar-shape. Starting from the x, y, z frame, Fig. 4.1 and with the z axis going from the SMC centre to the observer, we move to the ξ, η, ζ principal axes frame through a counterclockwise rotation around the z axis of the position angle followed by a counterclockwise rotation around the new ξ axis of the inclination angle. For the OS population, $\sigma_Z = 2.1$ **kpc** and $(\Xi_0, \Upsilon_0) = (0.8, 1.2)$ **kpc**, with the reference frame $(\Xi, \Upsilon, Z = z)$ obtained, from the x, y, z one, through a counterclockwise rotation around the z axis of the position angle. Following again the analysis of Bekki & Chiba (2009) we assume a OS over YS mass-ratio of 6:4, as in their fiducial model (this quantity is however not well constrained by the simulation and overall its estimate is still not robust). Accordingly, the central density values are fixed to 3.9×10^7 $M_\odot kpc^{-3}$ and 8.5×10^6 $M_\odot kpc^{-3}$ for the old and young star population, respectively.

The center and the distance of the SMC are both not too well constrained and in particular an offset of the young and old population, both in distance and in position, which may indeed be relevant for the evaluation of the microlensing quantities, has been discussed by several

authors. Here again we follow the analysis of Haschke et al. (2012), and reference therein, and assume, for our fiducial model, the same center and distance for both populations. In particular, we choose the optical center reported by Gonidakis et al. (2009) $\alpha = \mathbf{0^h51^m}$ and $\delta = \mathbf{-73.1}^\circ$ (J2000) and a distance to the SMC of **61.5 kpc**, the median distance of RR Lyræ stars (Haschke et al., 2012) found in agreement with that of the Cepheids. Finally, we fix the tidal radius of the SMC at **12 kpc**.

Because of a relative shift in distance between the OS and YS populations is still compatible with the data and may be expected to enhance the microlensing rate, as a test model we consider the case where the center of the YS population is shifted by **2 kpc** behind that of the OS one, at **63.5 kpc**, rescaling (increasing) the YS axes ratio to keep the same shape on the plane of the sky and changing accordingly the central normalization.

In Palanque-Delabrouille et al. (1998) the EROS collaboration introduced a SMC model for an estimate of the SMC self-lensing optical depth which has therefore become an often quoted "fiducial" value for this quantity. The SMC, for a total stellar mass of $\sim \mathbf{1 \times 10^9\ M_\odot}$ (a value that matches the one we use in our model), is approximated with a single population prolate ellipsoid elongated along the line of sight with exponential profile. The radial scale length, transverse to the line of sight, is fixed at **0.54 kpc** and the scale height along the line of sight left is free to vary in the range $\mathbf{2.5-7.5}$ **kpc**. We recall that the scale height is smaller than the depth by a factor 0.4648 (Haschke et al., 2012), so that **2.5 kpc** is the value that better matches our ones. Although clearly disfavored, in view of the more recent observational evidences, we consider useful to compare to this model in consideration of its importance in the microlensing literature. Indeed, being peculiarly different but still characterized by the same overall quantities (in particular, stellar mass and scale height), it represents a useful test case against our fiducial model[2].

[2]There is a caveat concerning the total mass and the corresponding normalization of this model. In fact, although Palanque-Delabrouille et al. (1998) report a stellar mass of $\sim \mathbf{1 \times 10^9\ M_\odot}$, which corresponds to our chosen normalization for the SMC luminous mass within **5 kpc**, we have to introduce a multiplicative factor 1.6, which we use, in the density normalization, with respect to the values reported in Palanque-Delabrouille et

4.2.1.2 Kinematics

We consider the velocity of SMC lenses as due to the sum of a non-dispersive component and a dispersive component. For the systemic proper motion we follow the analysis of Kallivayalil et al. (2006) with $(\mu_W, \mu_N) = (-1.16, -1.17)$ **mas yr**$^{-1}$ (in acceptable agreement with the outcome of the analysis of Piatek et al. 2008), with an observed line-of-sight velocity **146 km s**$^{-1}$ (Harris & Zaritsky, 2006). For the YS population we also introduce a solid body rotation around the ξ axis (Section 4.2.1.1) linearly increasing up to **60 km s**$^{-1}$ with turnover radius at **3 kpc** (Stanimirović et al., 2004). For the dispersive velocity component we assume an isotropic Gaussian distribution (Harris & Zaritsky (2006) report the line-of-sight velocity distribution to be well characterized by a Gaussian with a velocity dispersion profile independent from the position). For the velocity dispersion values we, again, follow those of the fiducial model of Bekki & Chiba (2009), with $\sigma = 30$ **km s**$^{-1}$ and $\sigma = 20$ **km s**$^{-1}$ for the old and young star populations, respectively. This is in good agreement with $\sigma = 27.5$ **km s**$^{-1}$ for the old populations stars analyzed in Harris & Zaritsky (2006) and with the analysis of Evans & Howarth (2008).

4.2.2 The MW disc and dark matter halo

For the MW disc, with assumed distance from the Galactic center **8 kpc** and local circular velocity **220 km s**$^{-1}$ (in agreement, for instance, with the recent analysis of Bovy & Tremaine 2012), we closely follow the analysis in Calchi Novati & Mancini (2011) with double exponential profiles thin and thick disc components with, respectively, local density **0.044 (0.0050) M**$_\odot$**pc**$^{-3}$, scale height **250 (750) pc**, scale length **2.75 (4.1) kpc** (Kroupa, 2007; Juríc et al., 2008; de Jong et al., 2010), and line-of-sight dispersion of **30 (40) km s**$^{-1}$.

For the Galactic dark matter halo, in order to coherently compare with previous mi-

al. (1998), to match the overall mass of our model within the tidal radius.

crolensing analyses, we assume the "standard" Alcock et al. (2000) pseudo-isothermal spherical density profile with core radius **5 kpc** (de Boer et al., 2005; Weber & de Boer, 2010) and Alcock et al. (2000) central density $\mathbf{0.0079\ M_{\odot}pc^{-3}}$ (in excellent agreement with up to date estimates as in Bovy & Tremaine (2012), see however Garbari 2012) for an isotropic Gaussian distribution velocity with line-of-sight dispersion $\mathbf{155\ km\ s^{-1}}$.

4.2.3 Mass function

For MW disc lenses we assume a power law mass function with slopes 1.3, 2.3 in the mass range $\mathbf{(0.08 - 1)\ M_{\odot}}$, with cut at $\mathbf{0.5\ M_{\odot}}$, upper limit for lenses fixed at $\mathbf{2\ M_{\odot}}$, normalization with mass up to $\mathbf{120\ M_{\odot}}$ and slope 4.5 above $\mathbf{1\ M_{\odot}}$ (Kroupa et al., 2011). Lacking any specific information we assume the same mass function also for the young star SMC population. The upper limit for the lens mass is chosen to avoid possible "visible" lenses, but the exact value is not very relevant because of the steepness of the mass function. For the SMC old star population we use a power law with slope 1.33 in the range $\mathbf{(0.08 - 1)\ M_{\odot}}$, and upper limit for normalization also fixed at $\mathbf{1\ M_{\odot}}$, following the results obtained for the Galactic bulge (Zoccali et al., 2000). Besides the MW and SMC stellar populations we also include a *brown dwarf* component, in the mass range $\mathbf{0.01 - 0.08\ M_{\odot}}$ with power law mass function index **0.3** (Allen et al., 2005; Kroupa et al., 2011). Following the local analysis of Chabrier (2003) we attribute to this component 5% of the overall relative stellar mass component.

For dark matter halo lenses we test a series of delta mass function in the mass range $\mathbf{10^{-5} - 10^{2}\ M_{\odot}}$.

4.3 Microlensing towards the SMC: The EROS and the OGLE campaigns

Microlensing observational campaigns towards the SMC have been carried out by the MACHO, the EROS and the OGLE collaborations. In Fig. 4.1 we show the monitored fields of view and the reported candidate events included in the present analysis.

The EROS collaboration, with the EROS-2 set up, observed a field of view covering the innermost **9 deg^2** of the SMC during about 7 years from 1996 to 2003. The first results of this campaign are discussed in Palanque-Delabrouille et al. (1998), with the presentation of a long duration event, EROS2-SMC-1, $t_{\rm E} \sim$ **120 days**, which was argued to be due, also because of the lack of any parallax signal (Gould, 1992) either by a large mass object in the Galaxy halo or by a lens lying near the source in the SMC itself. The event optical depth was estimated to be compatible with that expected by SMC self lensing. This event, first reported by the MACHO collaboration (Alcock et al., 1997) and known as MACHO 97-SMC-1, has been the object also of a spectroscopic analysis (Sahu, 1998) whose conclusion as for the nature of the lens, based on the lack of any signal from the lens, excluded it from being a Milky Way disc star, are in agreement with those presented in the original EROS analysis. A second analysis of this SMC EROS-2 campaign, for 5 years of data, was then presented in Afonso et al. (2003) with the inclusion of 3 additional long-duration candidate events claimed however to be *doubtful*, and finally rejected in the definite analysis presented in Tisserand et al. (2007) where only EROS2-SMC-1 was retained as a reliable candidate event (and with the analysis of Assef (2006) further favoring the SMC self-lensing interpretation of this event). In their final analysis on the MACHO issue out of observations towards both Magellanic Clouds (Tisserand et al., 2007) the EROS collaboration restricted the number of sources to a subset of "bright" source objects to better address the issue of blending. Overall, the EROS-2 SMC campaign lasted $T_{\rm obs}$ **= 2500 days** with an estimated total number of **0.86 × 10^6** monitored sources. With no candidate events reported towards the LMC, Tisserand et al.

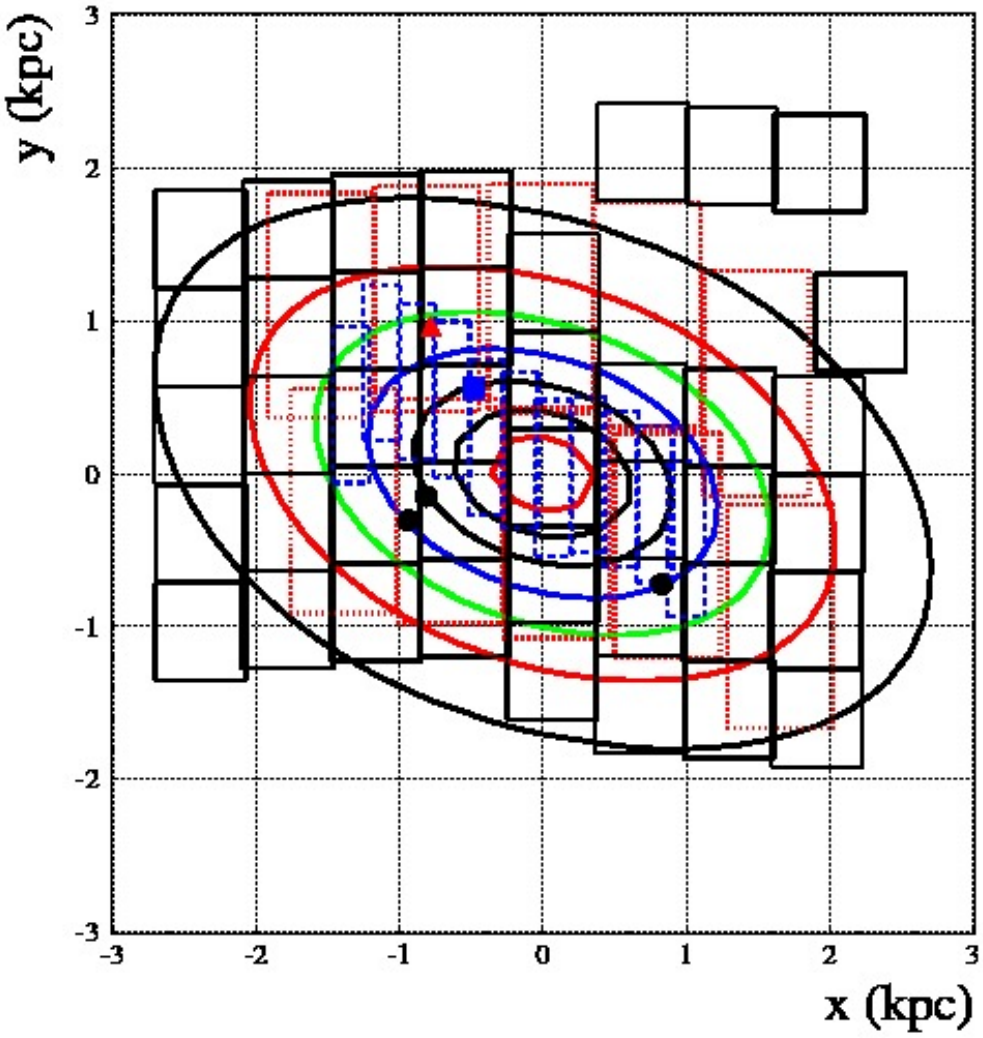

Figure 4.1: The fields of view monitored towards the SMC projected on the plane of the sky by OGLE-II (dashed lines, 11 fields), OGLE-III (solid lines, 41 fields) and EROS-2 (dotted lines, 10 fields). The position of the 5 reported candidate events is also included: 1 for OGLE-II (square), 3 for OGLE-III (circles) and 1 for EROS-2 (triangle). Further details on the events are given in Table 4.1. Also reported, the projected density for our fiducial SMC model (Section 4.2). The contours shown correspond to the values $\mathbf{0.2, 0.4, 0.6, 0.8, 1.0, 1.2, 1.4}$ in units of $\mathbf{10^8\ M_\odot\ kpc^{-2}}$. The $\boldsymbol{x-y}$ reference system has its origin at the center of the SMC, the $\boldsymbol{x}$-axis anti-parallel to the right ascension and the $\boldsymbol{y}$-axis parallel to the declination.

Table 4.1: Microlensing candidate events for the OGLE-II, OGLE-III and EROS-2 observational campaigns towards the SMC. The values for the duration, which are those used for the present analysis, and the estimate for the optical depth are from Wyrzykowski et al. (2009), Wyrzykowski et al. (2011b) and Tisserand et al. (2007), respectively. The coordinate positions are expressed in term of the reference frame used in Fig. 4.1.

event	x [kpc]	y [kpc]	t_E days	τ [10^{-7}]
OGLE-SMC-01	-0.485679	0.555917	65.0	1.40
OGLE-SMC-02	0.831350	-0.725003	195.6	0.76
OGLE-SMC-03	-0.937994	-0.309247	45.5	0.27
OGLE-SMC-04	-0.812418	-0.150195	18.60	0.14
EROS2-SMC-1	-0.781914	0.966178	125.	1.7

(2007) consider the observed rate compatible with the expected self-lensing signal and get to strong constraints on the halo mass fraction in form of MACHOs.

The OGLE collaboration is monitoring the SMC for microlensing events since more than 15 years. Wyrzykowski et al. (2010) reported results out of the OGLE-II campaign, (1996-2000), covering the SMC innermost **2.4 deg^2** for a total duration $\boldsymbol{T_{obs} = 1408}$ **days**. The OGLE collaboration makes the distinction between a larger sample of "All" and a restricted one of "Bright" sources, the latter chosen so to reduce the impact of blending in the analysis (for a discussion of the observational strategy of OGLE, in particular as for the choice of the source sample, we refer to Calchi Novati & Mancini 2011). OGLE reports an estimated number of potential sources $\boldsymbol{N = 3.6 \times 10^6}$ ($\boldsymbol{N = 2.1 \times 10^6}$), for the All (Bright) sample, respectively. Although Wyrzykowski et al. (2010) discuss in general terms the analyses for both samples of sources, they specifically report the results for the All sample only. Accordingly, this is the only one we will include within our analysis for OGLE-II. In particular, Wyrzykowski et al. (2010) report a single candidate event, OGLE-SMC-01, which is considered compatible, based on the optical depth, with the expected self-lensing signal. Thanks to an updated set up, a much larger SMC field of view, **14 deg^2**, was monitored during the OGLE-III phase (2001-2009). The results of this analysis are discussed in Wyrzykowski et

al. (2011b). The observational campaign lasted $\boldsymbol{T_{\rm obs} = 2870}$ **days** with an estimated number of sources equal to $\boldsymbol{N = 5.97 \times 10^6}$ ($\boldsymbol{N = 1.70 \times 10^6}$) for the All (Bright) sample, respectively. Three additional microlensing events are reported, OGLE-SMC-02, OGLE-SMC-03 and OGLE-SMC-04 (with OGLE-SMC-03 belonging to the All sample only), with the total optical depth still estimated to be in agreement with that expected from SMC self lensing.

Among the OGLE-III SMC candidate events, OGLE-SMC-02 (also known as OGLE-2005-SMC-1) deserved special attention. This was alerted by the OGLE-III Early Warning System (Udalski, 2003) and enjoyed additional observations also from space, with *Spitzer*, used to break the model degeneracies and solve the event, with the specific aim to measure the microlensing parallax (Dong, 2007). Dong (2007) address in particular the issue of the nature of the lens and conclude that the most likely location is the Galactic halo from a (binary[3]) black hole with a total mass of around $\mathbf{10\ M_\odot}$.

For the EROS-2, OGLE-II and OGLE-III analyses the source number is reported *per field*, with 10, 11 and 41 fields monitored by each experiment, respectively. In the following we do not include the field 140 of the OGLE-III campaign, the isolated field in the north-west part of Fig. 4.1, which presents a strong over-density of (potential lens) stars being centred along the line of sight of the foreground 47 Tuc (NGC104) globular cluster.

Both EROS (Tisserand et al., 2007) and OGLE (Wyrzykowski et al., 2010, 2011b) carry out an analysis of their detection efficiency based on the estimated number of monitored sources and presented in term of the event duration, $\boldsymbol{\mathcal{E} = \mathcal{E}(t_{\rm E})}$, which we also include in our analysis. In particular, OGLE reports the estimate for the efficiency both for a "sparse" and a "dense" field, depending on the density of stars. Accordingly, for each given value of the duration, we linearly interpolate the efficiency taking into account the estimated number of sources per field (the same value we use to estimate the expected number of events), while

[3]OGLE-2005-SMC-1 shows a deviation from that of a single lens event which has led Dong (2007) to conclude for a binary lens system. The anomaly is however extremely small so that the event is selected in the, single lens, Wyrzykowski et al. (2011b) analysis.

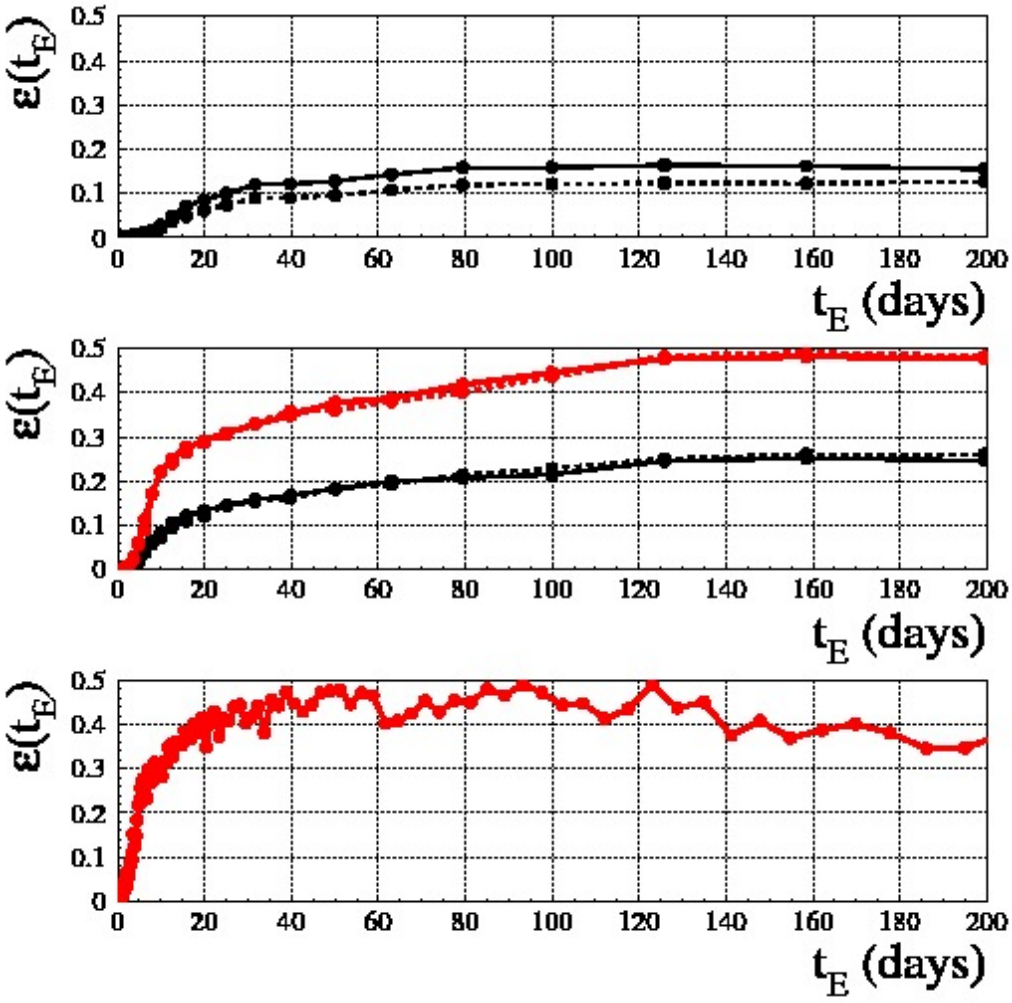

Figure 4.2: The detection efficiency as a function of the duration, $\mathcal{E}(t_{\rm E})$, for OGLE-II (top panel, All sample), OGLE-III (middle panel) and EROS-2. For OGLE the solid and dashed curves trace the efficiency for "sparse" and "dense" fields, as a measure of the crowding, respectively (for OGLE-III the two curves are almost indistinguishable). For OGLE-III the thicker curves (with larger values of the efficiency) refer to the Bright sample of sources.

keeping the reported values as fixed for those fields with lower, respectively higher, source star number. (This expedient, however, is effective for OGLE-II only, as for OGLE-III the available data for the sparse and dense fields indicate that the efficiency is roughly constant across the overall monitored field of view, even though the choice of the, two nearby, fields used for this analysis by OGLE-III may have biased this outcome.) In Fig. 4.2 we report a detail of the efficiency function $\mathcal{E}(t_{\rm E})$ for $t_{\rm E} < 200$ **d**. Besides the dependence on the crowding, we remark the low maximum value of $\mathcal{E}(t_{\rm E})$ for OGLE-II as compared to those of OGLE-III and EROS-2 and, for EROS-2, the much faster increase up to rather large values for small durations as compared to OGLE.

Overall, there are 5 microlensing candidate events reported towards the SMC upon which EROS and OGLE based their analyses and whose characteristics we summarize in Table 4.1 and which we will further consider in the present analysis. For definiteness, we will consider as homogeneous the All sample of sources of OGLE-II and OGLE-III and the Bright sample of sources of OGLE-III together with that of EROS-2.

Besides EROS and OGLE, also the MACHO collaboration monitored the SMC for microlensing events. The microlensing event MACHO Alert 98-SMC-1 has been the first binary caustic crossing event reported towards the Magellanic Clouds (Alcock et al., 1999), also monitored by the PLANET collaboration (Rhie et al., 1999). The analysis of the event, including additional data from the EROS and the OGLE data base, and in particular of the lens projected velocity, led to the conclusion that the event is more likely to reside in the SMC than in the Galactic halo (Alcock et al., 1999; Albrow et al., 1999; Rhie et al., 1999). The MACHO collaboration, however, did not present a detailed and complete analysis of the SMC campaign, as they did for the LMC one. In particular the estimate of the number of sources and the analysis of the detection efficiency, essential information to reliably assess the characteristics of the expected signal, are both missing. For this reason hereafter we no longer consider the results of the MACHO collaboration campaign towards the SMC.

4.4 Analysis

4.4.1 The microlensing optical depth

The optical depth, τ, is the instantaneous probability to observe a microlensing event. This is calculated as the integrated number of potential lenses within the microlensing tube for a given line of sight (for the background theory of microlensing see for instance Mao (2012) and references therein). The cross section radius of the microlensing tube is the *Einstein radius*

$$R_{\rm E} = \sqrt{\frac{4Gm}{c^2}\,\frac{D_l(D_s - D_l)}{D_s}}\,, \tag{4.3}$$

where m is the lens mass and D_l (D_s) the lens (source) distance from the observer, respectively. A relevant outcome of the microlensing theory is that the optical depth turns out to be independent from the lens mass (for a fixed overall mass of a lens population, lenses of smaller mass are more numerous but have a smaller cross section, whereas heavier lenses are less numerous but with a larger cross section, and this just at the level that the two effects compensate one each other). Further taking into account the source density distribution (which is relevant, in our case, for lenses within the SMC)

$$\tau = \frac{4\pi G}{c^2}\,\frac{\int \mathrm{d}D_s \int^{D_s} \mathrm{d}D_l \rho_s \rho_l \frac{D_l(D_s - D_l)}{D_s}}{\int \mathrm{d}D_s \rho_s}\,, \tag{4.4}$$

where ρ_l (ρ_s) are the lens (source) mass density distribution, respectively. According to its definition as an instantaneous probability, τ is a static quantity which can not be used to characterize the observed events. This feature makes the optical depth a very useful quantity from a theoretical point of view, being less model dependent, but also observationally. An estimate of the measured optical depth can indeed be used to trace the underlying mass (and spatial) density distribution of a given lens population.

For an experiment with overall duration $T_{\rm obs}$ and $N_{\rm obs}$ observed sources and sensitive to

event up to maximum magnification $u_0(\mathbf{max})$ (u being the impact parameter, the distance of the line of sight to the lens trajectory, which is roughly inversely proportional to the magnification at maximum), for a set of $N_{\rm ev}$ observed events with duration[4] $t_{{\rm E},i}$ (with $i = 1, \ldots, N_{\rm ev}$) and given efficiency $\mathcal{E}(t_{{\rm E},i})$, the estimate of the *measured* optical depth reads

$$\tau_{\rm obs} = \frac{\pi}{2\, u_0(\mathbf{max}) N_{\rm obs} T_{\rm obs}} \sum_i^{N_{\rm ev}} \frac{t_{{\rm E},i}}{\mathcal{E}(t_{{\rm E},i})}\,, \tag{4.5}$$

with the associated statistical error evaluated through the prescription of Han & Gould (1995a)

$$\sigma(\tau) = \tau\, \frac{\sqrt{< t_{\rm E}^2/\mathcal{E}^2 >}}{< t_{\rm E}/\mathcal{E} >}\, \frac{1}{\sqrt{N_{\rm ev}}}\,. \tag{4.6}$$

Coming to the specific problem of SMC microlensing, also looking at Eq. 4.4, we expect the signal from the MW lens populations to be rather independent from the inner structure of the SMC (with $\rho_l \approx 0$ within the SMC where $\rho_s \neq 0$). It results[5] , in particular, that the profiles for the MW disc and the Galactic halo optical depth are roughly constant across the field of view. Specifically, for the MW halo profile $\tau \sim 6.3 \times 10^{-7}$ (for a full MACHO halo) and for the MW disc $\tau \sim 0.04 \times 10^{-7}$, in both cases with relative variations up to 5% level. The SMC self-lensing optical depth, on the other hand, following the underlying lens spatial density profile, is strongly variable, Fig. 4.3, with peak central value, for our fiducial model, $\tau = 1.3 \times 10^{-7}$, and the observed events falling within the lines of equal optical depth values **0.5** and 0.8×10^{-7}. As expected, the introduction of a shift in distance between the OS and the YS population for a test model against the fiducial one (Section 4.2.1.1) enhances the SMC self-lensing signal. The relative increase with respect to the fiducial model is at 6% level at the SMC center and below 5% for the average values across the monitored fields of view (in particular, with the YS lying **2 kpc** behind the OS, there is a strong enhancing, about

[4]The timescale of a microlensing event is the *Einstein time*, $t_{\rm E} = R_{\rm E}/v$ where v is the (transverse component of the) lens velocity with respect to the microlensing tube.

[5]For cross-check, the evaluation of the optical depth profiles has been carried out independently by two of us.

80%, of the signal from YS sources with OS lenses, which is however almost completely compensated by a corresponding decrease in the signal from OS sources with YS lenses). For completeness we mention also the outcome of the optical depth analysis for the SMC dark matter halo. The profile is asymmetric following the underlying SMC luminous profile and overall inclination, with, for a full SMC halo, peak value $\mathbf{0.46 \times 10^{-7}}$ (in the south-west part of the SMC, following the SMC inclination, around at position $\boldsymbol{x, y = 1.1, -0.6}$ in the reference frame of Fig. 4.1 and Fig. 4.3) and average value across the field of view in the range $\mathbf{(0.31 - 0.38) \times 10^{-7}}$ (the smaller and larger value for OGLE-III and OGLE-II fields, respectively). Overall, this is only about 5% of the MW halo signal and therefore we will hereafter neglect this component.

The MW dark matter halo optical depth we evaluate towards the SMC for a full MACHO halo, $\mathbf{6.3 \times 10^{-7}}$, is significantly larger than the corresponding value we had evaluated towards the LMC, $\mathbf{4.5 \times 10^{-7}}$ (Calchi Novati et al., 2009). This increase is to be attributed to the increase in Galactic longitude and, to somewhat less extent, to the increase of the distance (whereas the increase, in absolute value, in Galactic latitude tends to reduce the optical depth).

In the following we will address the issue of the nature of the observed events through the analysis of the microlensing rate. It is however useful to consider, to some extent, this issue already within the framework of the optical depth, in particular asking whether the stellar lens populations may or not explain the observed signal and this starting from the consideration that the largest signal is expected, as it may be guessed looking at the relative values of the optical depth, from stellar lenses within the SMC rather than from MW disc lenses.

The expected quantity to be compared to the measured optical depth is the *average* optical depth value across the field of view where the $\boldsymbol{N_{\mathrm{obs}}}$ source stars entering Eq. 4.5 are monitored. Furthermore, as to be expected and according to Eq. 4.6, the relative (statistical)

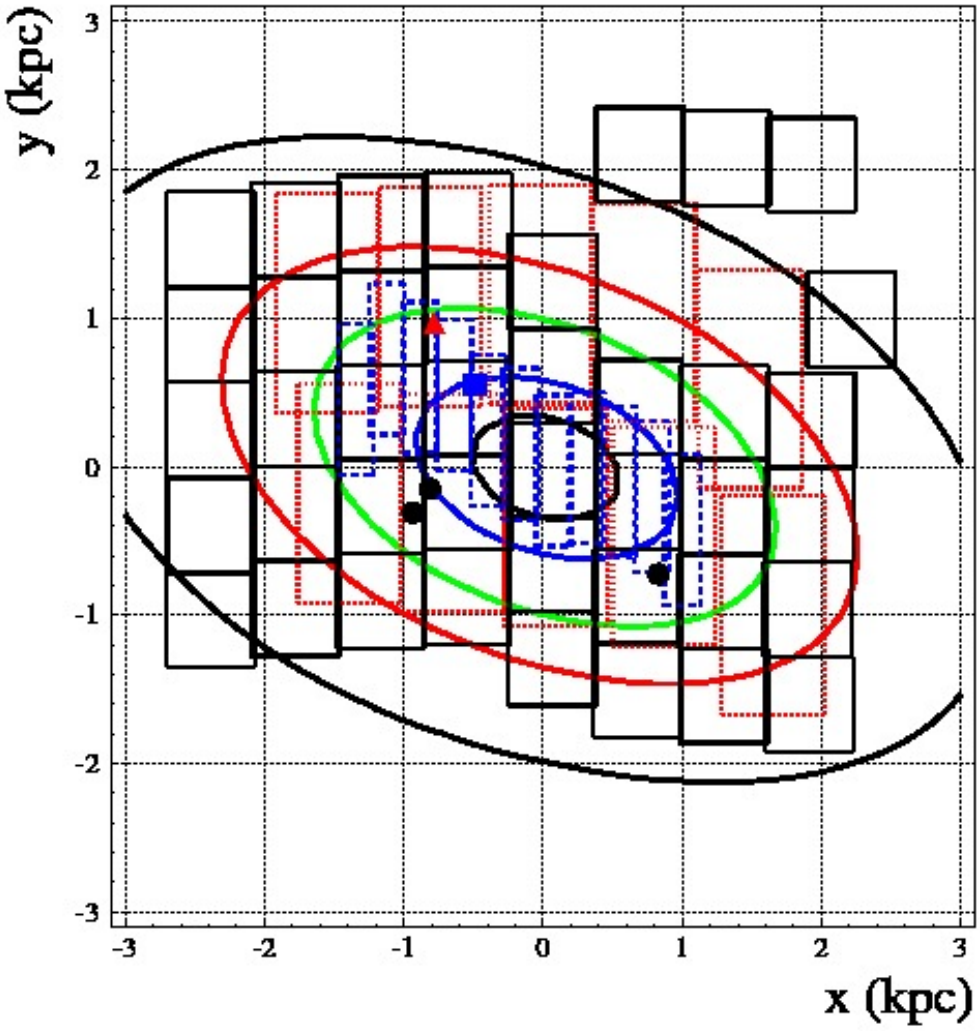

Figure 4.3: SMC self-lensing optical depth profile. The contours shown correspond to the values **0.1, 0.3, 0.5, 0.8, 1.0** in units of $\mathbf{10^{-7}}$. The maximum value is $\mathbf{1.3 \times 10^{-7}}$. The reference system, the observed event positions and field contours are indicated as in Fig. 4.1.

error on this estimate scales with the (square root of the) number of observed events and in particular $\sigma(\tau)/\tau = 1$ for $N_{ev} = 1$. To draw robust conclusions based on the optical depth, being statistical statements, a large enough sample of observed events is therefore mandatory.

The average optical depth for SMC self lensing across the monitored fields of view, according to our fiducial model, is $< \tau_{exp} >= 0.50$, **0.81** and **0.39** (in units of 10^{-7}) for EROS-2, OGLE-II and OGLE-III, respectively. This quantity is to be compared with the values already reported in Section 4.3. For EROS-2 and OGLE-II, with a unique event (and always in units of 10^{-7}) $\tau_{obs} = 1.7 \pm 1.7$ (EROS-2) and 1.40 ± 1.40 (OGLE-II) and $\tau_{obs} = 1.30 \pm 1.01$ for OGLE-III with three reported events. Although larger, the observed values are, within their large error, easily in agreement with the expected ones for SMC self lensing.

Given the very small number of observed events we can not aim at drawing stronger conclusions on the basis of the optical depth analysis. We can still, however, try to gain some further insight by addressing the issue of the spatial distribution of the events. The motivation comes from the observation of the very rapid, nonlinear, variation of the expected optical depth profile across the monitored fields of view (which is made apparent, for instance, by the strong decrease of the expected average value moving from OGLE-II to OGLE-III, where a much larger region has been monitored). This makes the average optical depth value reported above of limited interest. The usual way out to address this issue is to consider smaller and more homogeneous sub-regions where to perform the analysis.

Starting from the observation that the measured optical depth is (inversely) proportional to the number of monitored sources, we choose the bin size so that they contain an equal fraction of the overall number of sources, and in particular we select four bins[6]. The results

[6]To evaluate the number of sources within the bins we start from the knowledge of the number of sources per field from which we have to evaluate, within each field, the number of sources within the region delimited by the given line of equal value of optical depth. To this purpose we use the relative fraction of the integrated source density distribution but we note that the result do not change much if using the relative fraction of surface area.

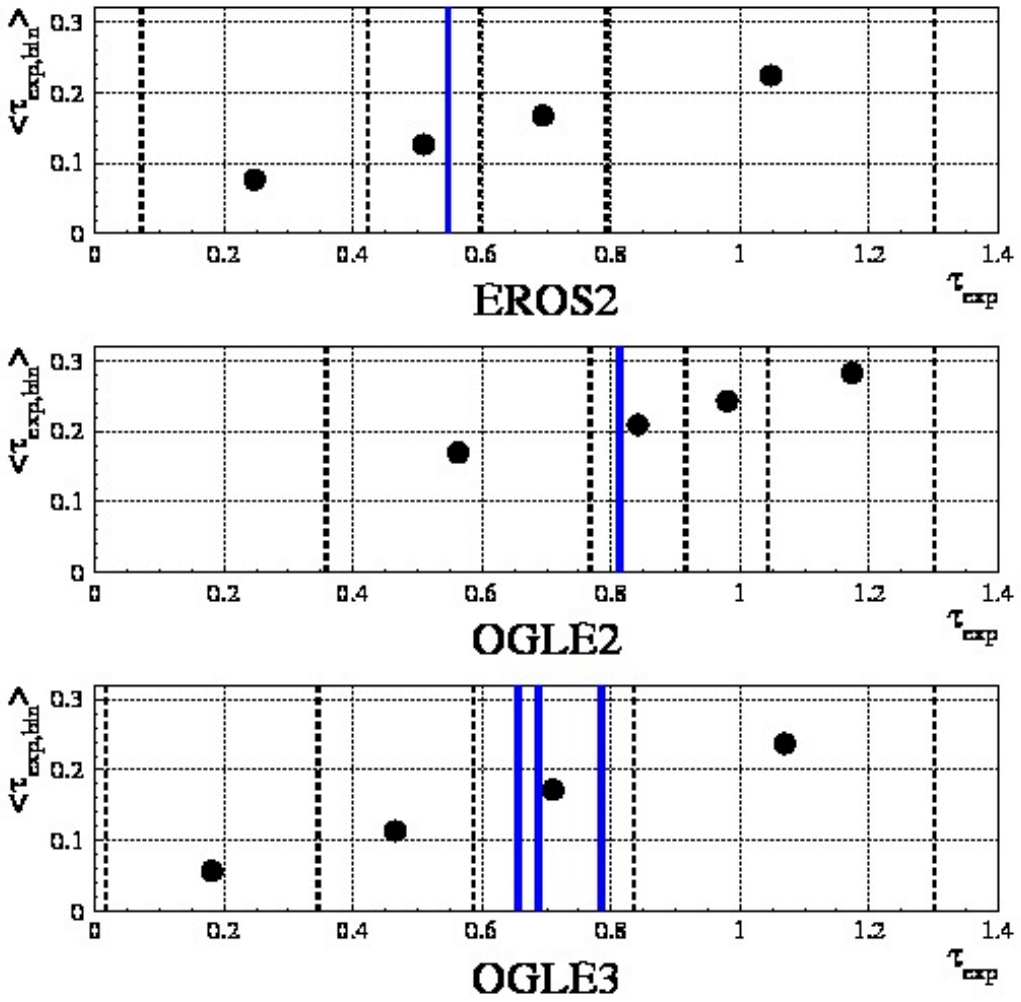

Figure 4.4: Average expected SMC self-lensing optical depth evaluated in bins. also indicated along the x-axis where, to trace to underlying space, we report the value of the SMC self-lensing optical depth as reported in Fig. 4.3. Specifically, the dots indicate the average values as estimated towards the bins whose limits are shown by the dashed vertical lines (the bins are defined so to contain an equal fraction of monitored sources, see text for further details). In particular, the values on the y-axis are rescaled so to be homogeneous with the observed values reported in Table 4.1 (as we have 4 bins and $\tau_{\rm obs} \propto 1/N_{\rm obs}$ the rescaling factor is equal to 4). The vertical solid lines indicate the positions of the observed events in this parameter space. From top to bottom we report the results we obtain for EROS-2, OGLE-II and OGLE-III. All the optical depth values are in units of 10^{-7}.

of this analysis are shown in Fig. 4.4, where the extent to which the average optical depth increases moving towards the SMC center and the relative position of the observed events within this parameter space are highlighted. Looking in particular at OGLE-III (bottom panel), for which all three events fall within the innermost second bin, this can read out as follow. Restricting the analysis to this bin the optical depth value (always in units of $\mathbf{10^{-7}}$) to be compared with $\boldsymbol{\tau_{obs,bin} = 1.30 \pm 1.01}$ would be $\boldsymbol{< \tau_{exp} >_{bin} = 0.17}$.

We can compare these results with those reported in the analysis of Palanque-Delabrouille et al. (1998), as for the SMC self lensing signal, often quoted and used as a "fiducial value". In particular, for a scale length $\boldsymbol{h = 2.5}$ **kpc** Palanque-Delabrouille et al. (1998) report, for SMC self lensing, an average value of $\mathbf{1.0 \times 10^{-7}}$. Allowing for the caveat of the different central normalization (Section 4.2.1), possibly because of a different definition of the region over which we average the optical depth and/or for a difference in other parameters of the model, we fail to reproduce this result. With a peak central value of $\mathbf{6.2 \times 10^{-7}}$ we find instead an average expected value of $\mathbf{0.8 \times 10^{-7}}$ for the EROS-2 monitored fields of view. For OGLE-II and OGLE-III we obtain **1.7** and $\mathbf{0.56 \times 10^{-7}}$, respectively. Comparing with the results of our fiducial model, following also the discussion in Section 4.2.1, we find that this density distribution leads to a much more centrally peaked optical depth profile (with the larger relative difference for the OGLE-II fields). In order to quantify this statement we can repeat the bin analysis discussed above. Considering the OGLE-III case, the three observed events still fall, with line of sight expected optical depth values between **0.81** and $\mathbf{1.3 \times 10^{-7}}$, in the second bin starting from the more central one, for an average expected value to be compared with the observed one of $\boldsymbol{< \tau_{exp} >_{bin} = 0.27 \times 10^{-7}}$. More strikingly, the ratio of the inner over outer bin-averaged optical depth expected value is about 20 for this model as compared to 4 for our fiducial model (in particular, the inner bin average expected value is $\mathbf{0.65 \times 10^{-7}}$ to be compared to $\mathbf{0.24 \times 10^{-7}}$ for the fiducial model). This outcome clearly highlights the different rate of increase of the expected SMC self-lensing signal moving

across the monitored fields of view. Furthermore, allowing for the small statistics of events, this would make it more difficult, on the basis of the spatial density distribution, to reconcile the observed signal with that expected from SMC self-lensing alone.

The SMC self-lensing optical depth has been analyzed also by other authors. Sahu (1998) estimate values in the range $\mathbf{1.0-5.0\times10^{-7}}$. Graff & Gardiner (1999), based on the Gardiner & Noguchi (1996) $\boldsymbol{N}$**−**body simulation of the SMC, derived an average smaller value, $\mathbf{0.4\times10^{-7}}$, arguing that, compared to the Palanque-Delabrouille et al. (1998) and Sahu (1998), both reporting larger values, a reason of disagreement could be traced back in the smaller line of sight thickness used. All these analyses, however, somehow suffer from the very large uncertainties in the model of the SMC luminous components which, if not still fully solved, are by now largely smoothed out by the more recent analyses (as in particular those based on the newly available OGLE-III data set).

For the above discussion on the spatial distribution we have considered, for self lensing, the SMC luminous component lenses only. This is justified by the much larger optical depth of this component compared to that of MW disc lenses. Specifically, the ratio of the optical depth average value for SMC self lensing over that of MW disc vary in the range from $\sim$ **10** up to $\sim$ **20** (for OGLE-III and OGLE-II fields, respectively, the second being more clustered around the SMC center). As further addressed below, coming to the expected signal in term of number of events, the SMC self-lensing signal remains larger than that of the MW disc lenses, but only about half as large as it results from the optical depth analysis alone.

4.4.2 The microlensing rate

The microlensing rate, $\boldsymbol{\Gamma}$, is defined as the number of new lenses, per unit time, entering the microlensing tube and therefore giving rise to a new microlensing event, for a given line of sight and per source star. It is therefore a *dynamic* quantity, as opposed to the optical

depth. We recall that for a generic microlensing event, point-like single lens and source with uniform relative motion, the only physically available measured parameter of the lensing parameter space, besides the position, is the event duration, $t_{\rm E}$. In particular, the lens mass, the lens and source distances and the relative velocity are not directly accessible to the observations. At the price of introducing a number of additional ingredients in the model, with respect to the optical depth, the microlensing rate provides us with the expected event number and, in particular, the expected duration and position distributions.

$$\begin{aligned} {\rm d}\Gamma &= 2\rho_l(D_l)\frac{\rho_s(D_s)}{{\rm I}_s}u_0({\rm max})\times \\ &\quad \xi(\mu)vR_{\rm E}(D_l,D_s,\mu)P(v){\rm d}D_l{\rm d}D_s{\rm d}\mu{\rm d}v\,, \end{aligned} \tag{4.7}$$

where $\mathbf{I}_s$ is the normalization for the source density distribution, the integration of ρ_s along the line of sight, $\xi(\mu)$ the lens mass function. $P(v)$ is the (assumed isotropic) distribution for the lens-source relative velocity (transverse to the line of sight)

$$P(v) = \frac{1}{\sigma_{sl}^2}\,v\exp\left(-\frac{v^2+A^2}{2\sigma_{sl}^2}\right){\rm I}_0\left(\frac{Av}{\sigma_{sl}^2}\right), \tag{4.8}$$

where $\mathbf{I_0}$ is the modified Bessel function of first kind, $\sigma_{sl}^2 \equiv \sigma_l^2 + x^2\sigma_s^2$, with σ_l (σ_s) the lens (source) 1-d velocity dispersion, A the modulus of the bulk motion components (solar motion, SMC internal and bulk motions), $x \equiv D_l/D_s$ (for a discussion we refer for instance to Calchi Novati et al. (2008) where also the more general case of an anisotropic Gaussian distribution is addressed).

The number of expected events, $N_{\rm exp}$, is proportional to the integral of the microlensing rate over the full available parameter space. The experimental detection efficiency being usually evaluated as a function of the event duration, $\mathcal{E} = \mathcal{E}(t_{\rm E})$, it results

$$N_{\rm exp} = N^*_{\rm obs}T_{\rm obs}\int {\rm d}t_{\rm E}\,\frac{{\rm d}\Gamma}{{\rm d}t_{\rm E}}\,\mathcal{E}(t_{\rm E})\,. \tag{4.9}$$

The product $N^*_{\rm obs} T_{\rm obs}$ is sometimes referred to as the "exposure", E. Starting from the relation $t_{\rm E} = R_{\rm E}/v$ we evaluate, from Eq. 4.7, $\mathrm{d}\Gamma/\mathrm{d}t_{\rm E} = \mathrm{d}\Gamma/\mathrm{d}v \times R_{\rm E}/t^2_{\rm E}$.

4.4.3 The number and the duration of the expected events

In this Section we establish the basis for our following analysis on the lens nature for the observed events by reporting the results we obtain by the analysis of the microlensing rate.

As a first step we evaluate the differential rate $\mathrm{d}\Gamma/\mathrm{d}t_{\rm E}$ for all the populations we consider: SMC self lensing, MW disc and MACHO lenses. The number of sources, for each experiment, being known *per field*, we therefore evaluate the rate towards the central line of sight of each EROS-2, OGLE-II and OGLE-III field. For SMC self lensing, because of the large variation across the monitored fields of the underlying lens population, we rather evaluate the *average* rate across the field of view. This becomes relevant especially for the more peaked Palanque-Delabrouille et al. (1998) model, with an overall decrease in the number of expected events, relative to the case where the single central line of sight is considered, that sums up to about 10% (and is much larger in the innermost fields).

In Table 4.2 we report some statistics on the expected duration distribution for self lensing populations and MACHO lensing for the OGLE-III All sample set up and detection efficiency. As remarked, the EROS-2 corresponding distribution is somewhat shifted towards smaller values of $t_{\rm E}$, at about 10%-20% level.

In Fig. 4.5 we show the differential rate modulated by the detection efficiency, $(\mathrm{d}\Gamma/\mathrm{d}t_{\rm E})_{\mathcal{E}}$ for (both stars and brown dwarfs) SMC self lensing and MW disc lenses (top panel) and for a set of MACHO mass values from 10^{-2} up to $1\ \mathrm{M}_\odot$ for MW MACHO lenses. The (normalized) distributions shown are averaged across the monitored fields of view (the spatial variation being more pronounced for the SMC self-lensing signal). In particular we show the result we obtain in the OGLE-III case.

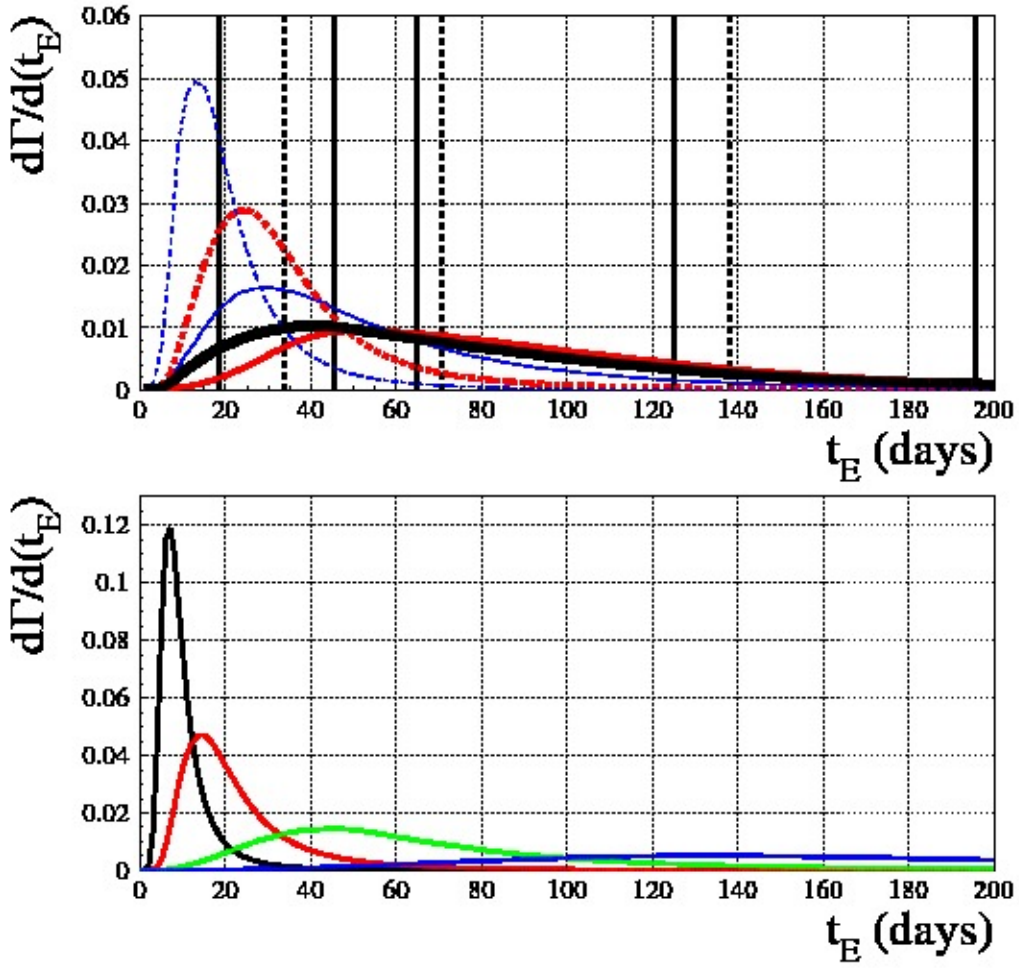

Figure 4.5: Normalized differential rate distribution, $\mathbf{d\Gamma/dt_E}$, corrected for the detection efficiency. Top panel: the expected distribution, each separately normalized, for the different self-lensing populations considered. Dashed and solid line are for the brown dwarf and star lenses, thin and thick lines for MW disc and SMC lenses. The thicker solid line is for the resulting overall self-lensing distribution. The dotted vertical lines indicate the 16%, median and 84% values of this distribution. The solid vertical lines indicate the values for the observed events, Table 4.1. Bottom panel: the expected distribution for MW MACHO lenses varying the MACHO mass. Moving from left to right as for the modal value: **0.01, 0.1, 0.5** and **1** $\mathbf{M_\odot}$.

Table 4.2: Microlensing rate analysis: expected duration distribution for self lensing lenses and MW MACHO lensing. We report the **16%, 34%, 50%, 68%, 84%** values for the OGLE-III All sample set up and detection efficiency.

lenses	16% (d)	34% (d)	50% (d)	68% (d)	84% (d)
SMC	46.	65.	84.	110.	150.
SMC BD	19.	25.	31.	40.	54.
MW disc	25.	36.	48.	66.	94.
MW disc BD	11.	15.	19.	24.	33.
SL	34.	53.	71.	98.	140.
$\mathbf{10^{-3}\ M_\odot}$	2.9	4.2	5.4	7.2	10.
$\mathbf{10^{-2}\ M_\odot}$	5.7	7.4	9.0	12.	16.
$\mathbf{10^{-1}\ M_\odot}$	12.	16.	20.	27.	37.
$\mathbf{1\ M_\odot}$	34.	48	60.	78.	110.
$\mathbf{10\ M_\odot}$	100.	140.	170.	220.	300.

In Table 4.3 we report the total number of expected events for the three experiment considered, EROS-2, OGLE-II and OGLE-III, for the self-lensing population considered, SMC self lensing and MW disc lenses, for both the stellar and brown dwarf contribution, for the All and Bright sample, whenever the case. The inspection of this table suggests a few comments. As for the relative weight of the different experiment, for the ALL sample of sources, the OGLE-III expected signal is about 3 times larger than that of OGLE-II. The EROS-2 signal sums up to about half of that of the Bright sample of OGLE-III. The MW disc signal

Table 4.3: Microlensing rate analysis: expected number of events for the self lensing populations (BD stands for brown dwarfs) for each of the three experiment analyzed.

lenses	OGLE-II	OGLE-III		EROS-2
	ALL	ALL	Bright	Bright
SMC	0.36	1.25	0.71	0.33
SMC DB	0.036	0.13	0.079	0.045
MW disc	0.045	0.22	0.13	0.077
MW disc BD	0.0035	0.020	0.014	0.0093
	0.44	1.62	0.93	0.46

is overall rather small compared to the SMC self-lensing one. The different relative weight for OGLE-II and OGLE-III (about 7% against 12%) can be traced back mainly to the different extent of the monitored fields. The somewhat larger fraction for EROS-2, 17%, can be understood on the basis of the larger efficiency for smaller values of the Einstein time. Overall, this makes EROS-2 quite relevant as compared to OGLE-III. Finally, although small, the expected SMC brown dwarf signal turns out to be about as large of the stellar MW disc one. Here again the relative increase for EROS-2 can be traced back to the different shape of the efficiency curve. Overall, the MW disc signal represents 10%-16% of the overall self-lensing signal. The enhancement of this ratio when considering the expected number as compared to the optical depth analysis is understood, given that $\Gamma \propto \tau / t_{\rm E}$, on the basis of the expected shorter duration of MW disc events.

The Palanque-Delabrouille et al. (1998) model strongly enhances the SMC self-lensing expected signal, resulting in about twice as much expected events. Coherently with the optical depth analysis these are found to be, however, much more strongly peaked in the innermost SMC region (for OGLE-III, for instance, we find that 60% of the events should be expected in the innermost bin, defined as in the previous optical depth analysis, against 40% for our fiducial model). In particular, the expected number of self-lensing events is 1.0 (OGLE-II), 3.1 and 1.8 (OGLE-III, All and Bright sample, respectively) and 0.8 (EROS-2). The major enhancement (about 2.5 times as much) is found, as expected, for the more centrally clustered OGLE-II fields of view.

The number of expected dark matter events, as a function of the MACHO mass for a full MACHO halo, is shown in Fig. 4.6. The expected increase in the number for smaller values of the MACHO mass is increasingly compensated by the corresponding decrease in the detection efficiency for small values of the event duration. In particular, coherently with the relative difference in their detection efficiency functions $\mathcal{E}(t_{\rm E})$, the expected EROS-2 signal overtakes the OGLE-III one for values below $5 \times 10^{-3} {\rm M}_{\odot}$. Overall, the expected

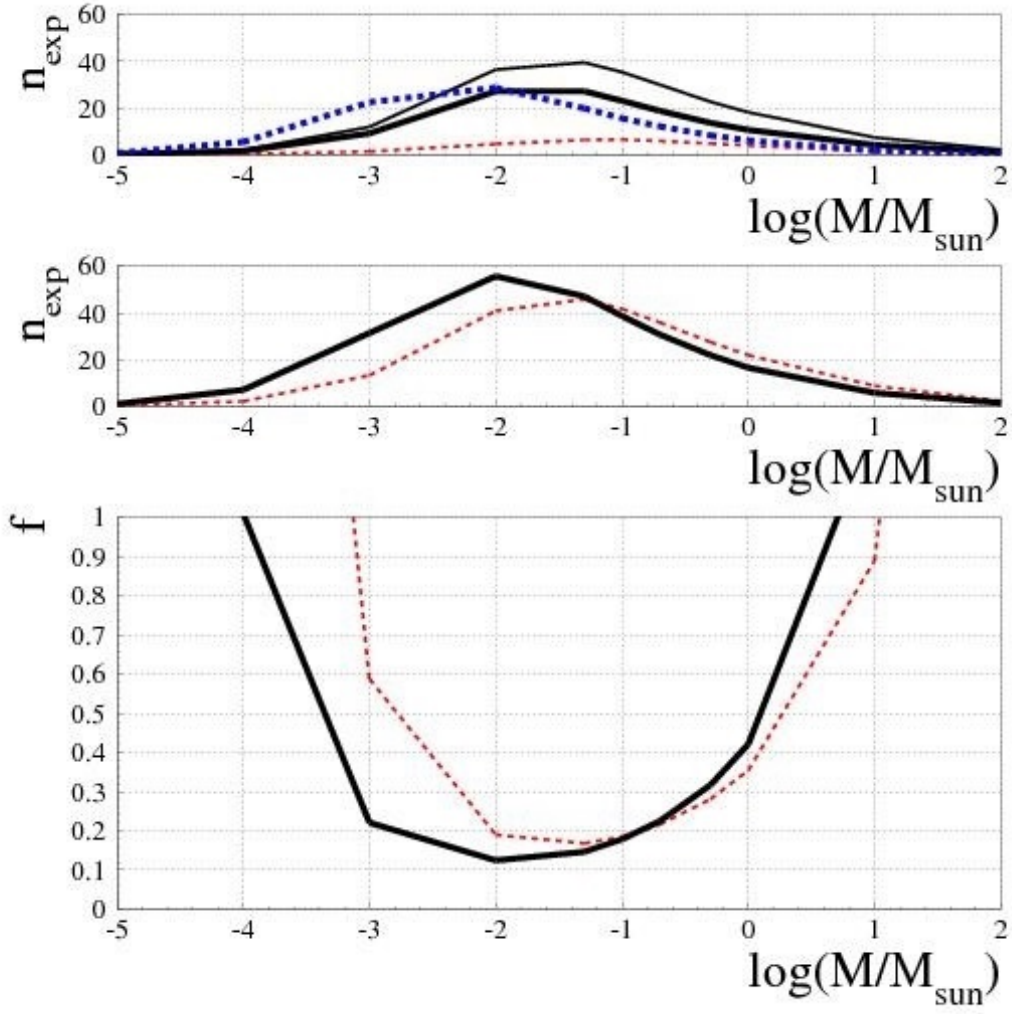

Figure 4.6: Top and middle panel: number of expected MW MACHO lenses events as a function of the MACHO mass for a full MACHO halo. Top panel: we report separately the results for OGLE-II (All sample), OGLE-III (All and Bright samples) and EROS-2 (dashed, thin solid, thick solid and dot-dashed lines, respectively). Middle panel: we report separately the results for the All sample (OGLE-II and OGLE-III, dashed line) and the Bright sample (OGLE-III and EROS-2, solid line). Bottom panel: 95% CL upper limit for the halo mass fraction in form of MACHOs based on the Poisson statistics of the number of events (see text for details). Solid and dashed curves as in the middle panel.

signal rapidly drops to zero below $\mathbf{10^{-3} - 10^{-4} M_{\odot}}$ and, at the opposite end, above $\mathbf{1 - 10\ M_{\odot}}$. The expected peak values in the number of events is for a MACHO population in the mass range $\mathbf{10^{-2} - 10^{-1} M_{\odot}}$.

Overall, the relative ratios of the expected number of events from OGLE-II, OGLE-III (All and Bright sample) and EROS-2 are well understood starting from Eq. 4.9 and the specifications of the different set up, in particular the value of the exposure, $\boldsymbol{E}$ and the efficiency curve $\boldsymbol{\mathcal{E}(t_E)}$. OGLE-II enjoys a large exposure, $\boldsymbol{E_{OGLE-II} = 5.1 \times 10^9}$, however it suffers from a quite small efficiency, below 10% for $\boldsymbol{t_E < 10}$ **d** and raising at most up to about 16%. For OGLE-III it results $\boldsymbol{E_{OGLE-III} = 1.7 \times 10^{10}}$, for the All sample and $\mathbf{4.9 \times 10^9}$ for the Bright sample for which, on the other hand, the efficiency is up to about twice as large than for the All sample. In particular, $\boldsymbol{\mathcal{E}(t_E) \sim 20\%\ (10\%)}$ for $\boldsymbol{t_E = 10}$ **d**, $\boldsymbol{\sim 30\%\ (13\%)}$ at **20 d** with top values about **50% (25%)** in the range $\boldsymbol{\sim 120 - 300}$ **d**, for the Bright (all) sample, respectively. Finally, EROS-2 is characterized by a long duration but a relatively small number of monitored sources so that $\boldsymbol{E_{EROS-2} = 2.3 \times 10^9}$, half as small $\boldsymbol{E_{OGLE-III}}$ Bright sample. The strength of EROS-2 is however the efficiency reaching 30% already at $\boldsymbol{t_E \sim 10}$ **d** and remaining stable above 40% in the range $\boldsymbol{t_E \sim 20 - 140}$ **d**. On this basis we can understand, for instance, the large number of EROS-2 expected MACHO lensing events, in particular for low mass values ($\mathbf{10^{-3} - 5 \times 10^{-2}\ M_{\odot}}$), as compared to OGLE-II whereas the expected self-lensing signal, for EROS-2 and OGLE-II, turns out to be completely equivalent in term of the number of expected events.

In the bottom panel of Fig. 4.6 we report the 95% CL upper limit for the halo mass fraction in form of MACHOs, $\boldsymbol{f}$, based on the Poisson statistics of the expected versus the observed number of events. In particular we make use of the confidence level statistics for a Poisson distribution with a background, also following a Poisson distribution, whose mean value is supposed to be exactly known and which is given in our case by the expected self-lensing signal, following the recipe of Feldman & Cousins (1998). This gives us, in

particular, the upper limit, fixed the confidence level, for the signal (the MACHO lensing number of events). We consider separately the full set of the All sample of sources (OGLE-II and OGLE-III) and the Bright one (OGLE-III and EROS-2). For the All (Bright) sample with $\boldsymbol{n_{\rm obs} = 4\ (3)}$ reported candidate events and a background signal of $\boldsymbol{n_{\rm exp,SL} = 2.06\ (1.39)}$ the 95% CL upper limit turns out to be of 7.70 (6.86) events. The lowest upper limit (here and in the following at 95% CL) for the Bright (All) sample is for $\boldsymbol{10^{-2}}$ ($\boldsymbol{5 \times 10^{-2}}$) $\boldsymbol{M_\odot}$ at $\boldsymbol{f = 12\%}$ ($\boldsymbol{17\%}$), with $\boldsymbol{f = 32\%}$ ($\boldsymbol{28\%}$) for $\boldsymbol{0.5\ M_\odot}$, respectively. The profile of the upper limit for the All and Bright sample follow, reversed, that of the expected number of MACHO lensing events modulated by the expected background signal values. In particular, when joining OGLE-II and OGLE-III for the All sample and OGLE-III and EROS-2 for the Bright sample, following the already remarked enhanced efficiency of EROS-2 to short duration (low mass) events, the resulting constraints for $\boldsymbol{f}$ are stronger (also in an absolute sense) for the Bright sample for small mass values (here roughly below $\boldsymbol{0.1\ M_\odot}$), respectively stronger for the All sample above this threshold.

In their analyses, the OGLE collaboration, roughly based on the expected optical depth but lacking an explicit evaluation of the expected number of event for the self-lensing signal, and also following Moniez (2010), assumes that the background (self lensing) expected value is equal to the number of observed events. In this case 4 (3) for the All (Bright) sample, against our values, 2.1 (1.4), respectively. Under this assumption the upper limits for the signal, and therefore those on $\boldsymbol{f}$, are accordingly smaller, in this case 5.76 (5.25), respectively (which makes, in relative terms, a rather significant change). For reference we mention the values of these same upper limits assuming, instead, that the expected background is zero (namely, assuming there is no expected self lensing signal), 9.76 and 8.25 for the All and Bright samples, respectively.

Starting from the larger values of expected self-lensing events with the Palanque-Delabrouille et al. (1998) model, 4.17 (2.59) for the All (Bright) sample, we would get to

considerably smaller upper limit for the Poisson statistics with a background, 5.60 and 5.66 for the All and Bright sample, respectively (here the statistics makes the first value smaller, which is opposite to the result we obtain with our fiducial model). This then gives rise (the expected number of MACHO lensing events does not change) to stronger constraints for $\boldsymbol{f}$ (always at 95% CL): in the range 12%-16% for $\mathbf{10^{-2} - 0.2\ M_{\odot}}$ and 20% at $\mathbf{0.5\ M_{\odot}}$ for the All sample and down to 10% and below 20% in the range $\mathbf{10^{-3} - 0.2\ M_{\odot}}$ and 26% at $\mathbf{0.5\ M_{\odot}}$ for the Bright sample.

4.4.4 The nature of the observed events

What is the nature of the observed lensing systems?, or, to rephrase it, *is there any evidence for a signal from non self-lensing population, namely, from MACHOs?*. We now attempt to address this issue starting from the results presented in the previous section, and in particular moving beyond the simple statistics based on the event number presented in the last Section (Fig. 4.6).

4.4.4.1 The number of the events and their spatial distribution

OGLE-II reported one candidate event (All sample), for which we evaluate 0.44 expected self-lensing events. OGLE-III reported 3 (2) candidate events from the All (Bright) sample, with our evaluation of an expected self-lensing signal of 1.62 (0.93) events, respectively. Finally, EROS-2 reported one event out of a selected Bright sub-sample of sources, for which we evaluate an expected self-lensing signal of 0.46 events. Based on the underlying Poisson nature of the statistics of the detected events, the observed signal, according to the number of events, can be therefore fully explained by the expected self-lensing signal, according to our model most of it coming from faint SMC stars. As remarked, assuming a SMC model in agreement with that in Palanque-Delabrouille et al. (1998), for the same overall mass of

the SMC luminous population, the number of expected self-lensing events is about twice as large than what we obtain with our fiducial model. This model, leaving aside the discussed issue of the spatial distribution of the events, would then lead to an even stronger confidence on the reliability of this outcome.

Although the statistics of events is not large, we may try to move beyond this considerations by exploiting the additional characteristics of the observed signal. We have already discussed the spatial distribution within the framework of the optical depth analysis. In fact we expect the increase of the SMC self-lensing optical depth moving towards the SMC center to be reflected in a corresponding increase of the expected signal in term of the number of events. If we bin the observed field of view as in Section 4.4.1 we indeed find such an increase. For the MW lens populations, on the other hand, the expected distribution in term of number of events is found to be roughly flat. These results are not surprising as the bins are chosen to contain an equal number of sources and therefore the expected signal follow the underlying optical depth profiles. To gain some further insight we may evaluate the fraction of expected SMC self-lensing events, for each experiment, lying outside the contour of equal expected number of sources fixed by the position of the reported events. It results: 34%, 28% and 38% for EROS-2, OGLE-II and OGLE-III, respectively. For OGLE-III the reported value is derived for the outermost event, and in this case we may also evaluate the fraction of expected events lying within the contour of the inner reported event, which turns out to be of 47% (the corresponding fractions of source stars in these four cases are respectively 44%, 33%, 58% and 29%). Assuming the Palanque-Delabrouille et al. (1998) model we find again the signature of a much stronger gradient moving towards the SMC center, namely the fraction are significantly smaller (and larger for the last considered case). About 15% of the events, for EROS-2, OGLE-II and OGLE-III, are expected out of the contour of equal number of sources fixed by the position of the outermost reported event (for a fraction of source stars equal to 38%, 36% and 50%, respectively) and, for OGLE-III, 72% of

the events are expected (with 35% of the source stars) within the contour of the innermost reported event.

4.4.4.2 The duration distribution

Besides their position, the events are characterized by the duration. This is a useful statistics to our purposes as the duration distribution is independent from the expected event number. As a test case against the distribution of the observed durations we consider the expected distribution for self-lensing events, SMC self lensing and MW disc lenses, both stars and brown dwarf (Fig. 4.5). As a result we find that the duration of 2 out of 5 events falls outside the 16%-84% range of probability for self-lensing lenses. More specifically: there is only about 5% probability to get a self-lensing event duration shorter (longer) than that of OGLE-SMC-04 (OGLE-SMC-02). As apparent also from Fig. 4.5, short events are more likely for brown dwarf lenses, which represent, however, only about 10% of the overall expected signal (Table 4.3). On the other hand, very long duration events look difficult to be explained (the case of OGLE-SMC-02, for which additional information is available to characterize the event, is further discussed below). To further quantify these statements we may attempt to compare statistically the observed and the expected distributions. To this purpose we consider the smaller but homogeneous set of the three All sample OGLE-III microlensing candidates, which span, incidentally, the full range of observed durations, $\boldsymbol{t_{\rm E}}$ **= (18.6, 45.5, 195.6) d**. To compare the observed and expected self-lensing duration distribution first we make use of the Kolmogorov-Smirnov test which allows one to evaluate the probability to accept the null hypothesis that the two distributions are indeed equal. This is known, however, to be specifically sensitive to compare the *median* values of the distributions, and in fact we find a rather large probability, **62%**. A similar statistics, built to be more sensitive to the outliers, is that of Anderson-Darling (Press et al., 1992) for which indeed the probability, which we evaluate through a simulation, drops to **32%**.

A final remark, quite apparent at glance from Fig. 4.5, is that, if not completely by self-lensing events, the very large spread of the observed durations distribution makes unlikely the possibility to explain all the events by a single mass MACHO population (*if* any MACHOs).

4.4.4.3 The likelihood analysis

The likelihood analysis allows us to further address the issue of the nature of the events and in particular to quantify the limits for the halo mass fraction in form of compact halo objects, $\boldsymbol{f}$. To this purpose we proceed as detailed in Appendix 7.2, taking, for reference, the expression of the likelihood in terms of the differential rate with respect to the event duration. This leads to include within the analysis both the line of sight position and the duration of the observed events. Fixed the MACHO mass as a parameter, given the likelihood, we may build the probability distribution for $\boldsymbol{f}$, $\boldsymbol{P(f)}$, by Bayesian inversion assuming a constant prior different from zero in the interval $\boldsymbol{(0, 1)}$.

In Fig. 4.7 we show the results of the likelihood analysis, in particular we report the 95% CL upper limit for $\boldsymbol{f}$ as a function of the MACHO mass. The curve shape reflects in part that of the expected number of MACHO events reported in Fig. 4.6, weighted, however, by the number and the specific characteristics of the observed events. Here we consider separately the two cases of the 4 reported candidates from the All sample (OGLE-II and OGLE-III), and the 3 reported candidates from the Bright sample (OGLE-III and EROS-2), top and bottom panel in Fig. 4.7, respectively. For the All sample we find the lowest constraint for $\boldsymbol{f}$ in the mass range $\boldsymbol{10^{-2} - 10^{-1}\ M_{\odot}}$, with $\boldsymbol{f \leq 11 - 13\%}$. The upper limit then reduces to $\boldsymbol{30\%}$ at $\boldsymbol{1\ M_{\odot}}$, at the same level than that at $\boldsymbol{10^{-3}\ M_{\odot}}$. Whereas this second result is driven by the small number of expected MACHO lensing events there, the increase of the upper limit for $\boldsymbol{f}$ in the $\boldsymbol{10^{-1} - 1\ M_{\odot}}$ range is rather driven by the characteristics of the events. The overall shape behavior of the $\boldsymbol{f}$ upper limit is similar moving to the Bright sample. Here, however, thanks to the enhanced EROS-2 sensitivity to short duration events, we can put a

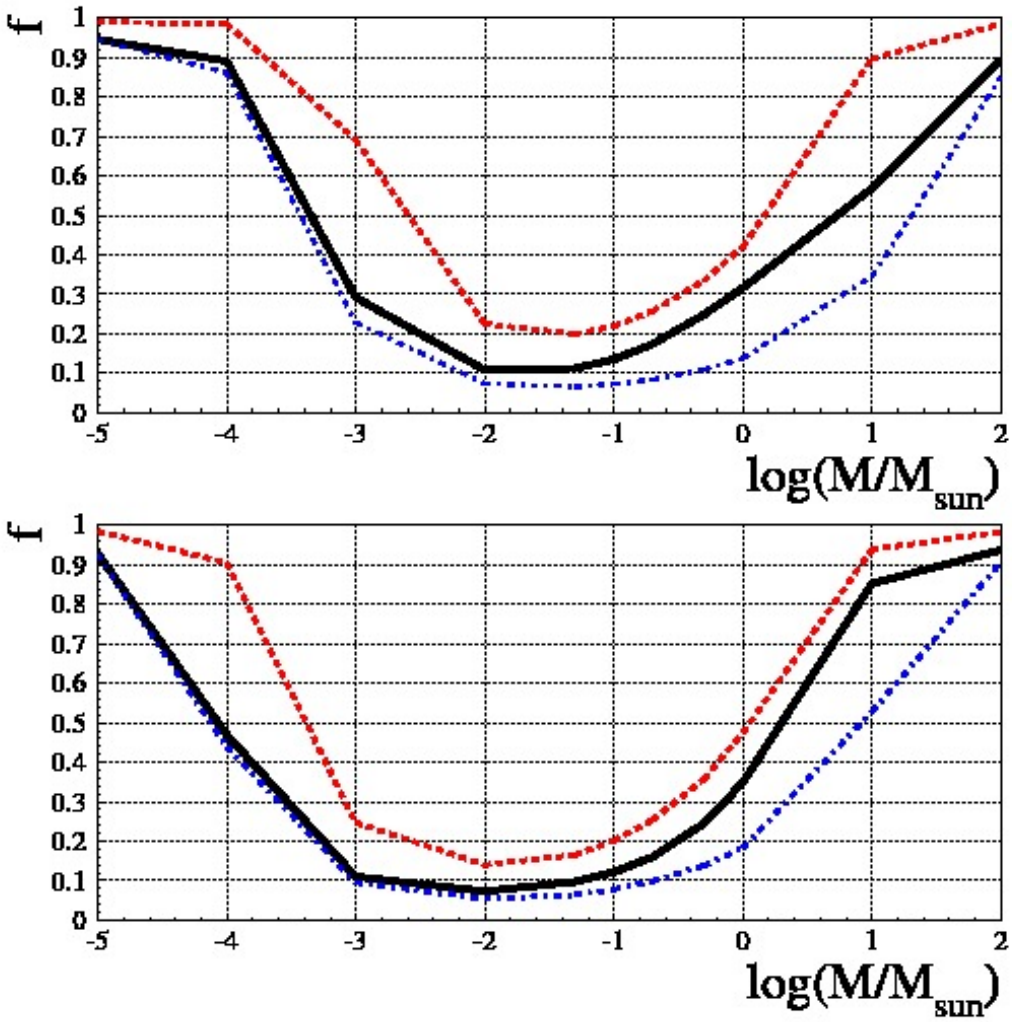

Figure 4.7: Likelihood analysis: 95% CL upper limit for the mass halo fraction in the form of MACHO, f, as a function of the MACHO mass (in solar mass units) for All (OGLE-II and OGLE-III, top panel) and Bright (OGLE-III and EROS-2) sample of sources, solid lines. The dashed (dot-dashed) empty (filled) square are the results we obtain under the hypothesis that the observed event are due to MACHO lensing (self lensing), respectively.

$f \sim 10\%$ upper limit constraint over the range $10^{-3} - 10^{-1}$ $M_\odot$, with the lowest value at $f \sim 7\%$ for 10^{-2} $M_\odot$. The increase in the upper limit above 10^{-1} $M_\odot$ is somewhat faster in this case, with $f < 35\%$ at 1 $M_\odot$. These behaviors, for the All and Bright sample, can also be more specifically explained on the basis of the event characteristics. In particular the very short, $t_E = 18.60$ d OGLE-SMC-04 event, both in the All and in the Bright sample somehow drives the results for low mass values, up to about 10^{-1} $M_\odot$, while the two long events, OGLE-SMC-02 and EROS2-SMC-1, both for the Bright sample, become relevant for large mass values (this is made apparent in particular by the, relatively, stronger constraint on f for 10 $M_\odot$ in the All with respect to the Bright sample, where in the second case two out of three events are very long duration ones).

A better understanding of the likelihood analysis results comes from the inspection of the dashed an dot-dashed upper limits in Fig. 4.7 where we report the results of the likelihood analysis under the assumption that the events are due to MACHO lensing (self lensing), respectively (we remark that these results are based on the MACHO lensing signal only, namely the expected self-lensing rate does not enter the likelihood function). Both for the All and the Bright sample of sources, assuming the events are self lensing, the differences in the upper limit for f, comparing with the solid line where no hypothesis are done on the lens nature, are small up to about 10^{-2} $M_\odot$ and then start increasing up to a rather large size. This somehow measures the extent to which, within the likelihood analysis, the events are weighted as self lensing compared to MACHO lensing. In particular, this confirms that the MACHO lensing signal is strongly suppressed especially for low mass values. The rather large difference in the two curves (solid and dot-dashed) for 10 $M_\odot$ can also be understood on this basis recalling the very long durations events present in the All and Bright sample of sources. The dashed curve built assuming the events are MACHO, on the other hand, can be looked at as giving the more conservative upper limit for f, regardless the characteristics of the events (just as the dot-dashed discussed above give the less conservative one which can

Table 4.4: Likelihood analysis: 95% CL upper limit for f, the halo mass fraction in form of MACHOs for the All and the Bright sample, with in particular (1) OGLE-II, OGLE-III; (2) EROS-2, OGLE-III; (3,4,5,6) OGLE-II and OGLE-III, OGLE-III and EROS-2 (for the All, Bright sample, respectively). In columns (1-3) the likelihood is expressed in term of the differential rate with respect to the event duration; in column (4) the likelihood is evaluated taking into account the number of expected events (Appendix 1); in column (5), (6) the upper limit on f is evaluated under the hypothesis that the observed events are (not) MACHOs.

mass	(1)	(2)	(3)	(4)	(5)	(6)
All sample						
$\mathbf{10^{-3}\ M_\odot}$	0.904	0.326	0.290	0.516	0.691	0.228
$\mathbf{10^{-2}\ M_\odot}$	0.665	0.120	0.107	0.167	0.224	0.073
$\mathbf{0.1\ M_\odot}$	0.579	0.152	0.135	0.167	0.218	0.071
$\mathbf{0.5\ M_\odot}$	0.789	0.261	0.247	0.255	0.333	0.109
$\mathbf{1\ M_\odot}$	0.861	0.325	0.315	0.321	0.420	0.137
$\mathbf{10\ M_\odot}$	0.928	0.615	0.567	0.755	0.896	0.345
Bright sample						
$\mathbf{10^{-3}\ M_\odot}$	0.133	0.437	0.109	0.186	0.247	0.095
$\mathbf{10^{-2}\ M_\odot}$	0.105	0.160	0.072	0.111	0.139	0.053
$\mathbf{0.1\ M_\odot}$	0.204	0.202	0.120	0.162	0.200	0.076
$\mathbf{0.5\ M_\odot}$	0.468	0.366	0.245	0.290	0.356	0.138
$\mathbf{1\ M_\odot}$	0.670	0.478	0.348	0.386	0.474	0.182
$\mathbf{10\ M_\odot}$	0.944	0.859	0.851	0.873	0.938	0.526

be obtained based on the available data). For the All sample this is at about 20% level in the range $\mathbf{10^{-2} - 10^{-1}\ M_\odot}$, reducing to 40% for $\mathbf{1\ M_\odot}$, whereas for the Bright sample the limit is up to about, in absolute sense, 6% smaller in the lower range and, as before, significantly smaller at $\mathbf{10^{-3}\ M_\odot}$ and, on the other hand, somewhat larger for $\mathbf{1\ M_\odot}$. Overall, the difference between the two curves (dashed and solid) is about constant at 10% (in absolute sense) for the Bright sample all the way from MACHO mass above $\mathbf{10^{-3}\ M_\odot}$. For the All sample the difference is also of about 10% but only within the range $\mathbf{10^{-2} - 1\ M_\odot}$. Below and above these values, at $\mathbf{10^{-3}}$ and $\mathbf{10\ M_\odot}$, the shape of the dashed curve then reflects the drop in the expected number of MACHO lensing events. The numerical detail of these results, also distinguishing each experimental set up, is reported in Table 4.4.

We can compare the upper limits on f obtained within the likelihood analysis to those derived from the Poisson upper limits discussed in Section 4.4.3 and Fig. 4.6. Overall, they appear, quite significantly at least in a relative sense, *larger*. The driving motivation is the characterization as *indistinguishable* of the "signal" with respect to the underlying "background" one assumes to evaluate the upper limits, for the signal, for the Poisson distribution with a background (Feldman & Cousins, 1998). The degeneracy in the lensing parameter space justify to some extent this characterization, however the likelihood analysis allows one to take advantage of the specific characteristics of the observed events. It is also interesting to note that, within the scheme of the Feldman & Cousins (1998) statistics, assuming the mean expected background to be equal to the observed signal, one would get to about equal (and for some values of the MACHO mass, even tighter) constraints for f.

The results discussed above on the likelihood are obtained with our fiducial model. We may wonder what happens when using the Palanque-Delabrouille et al. (1998) model for which we expect about twice as much self-lensing events. As a result we find that the upper limit we obtain in this case are indeed somewhat smaller, but the difference turns out never to exceed, in absolute sense, 3%-4%, namely, the two results are about equal. The underlying reason can be traced back in the spatial distribution of the observed events as compared to the expected signal which is, for the SMC self-lensing component, extremely more clustered around the SMC center in the Palanque-Delabrouille et al. (1998) model. From a methodological point of view, this outcome clearly highlights the extent to which it is relevant to include within the analysis all the information available to draw meaningful conclusions on the MACHO lensing as compared to the self-lensing one, which is specifically what is made possible by the likelihood analysis.

To conclude on the likelihood analysis we may address the question of whether the result we obtain is biased by our choice of expressing the likelihood in term of the differential rate rather than considering the number of expected events (Appendix 7.2). In this second

case, corresponding to the line of sight of the observed events, the MACHO lensing and the self-lensing signals are compared based on the number of expected events only (in particular with no reference, therefore, to the observed event duration). As a result, Table 4.4, the upper limit in this case turns out to be larger, and this can be understood on the basis that in most cases the observed durations are in agreement with the self-lensing expected ones and, if not, as for the very long duration events, the expected MACHO lensing signal is however quite small: overall this attributes to the self-lensing rate more weight with respect to the MACHO lensing one than in the case where only the expected number (along a specific line of sight) is considered. The overall change, however, turns not to be not too large, in an absolute if not relative sense, compared to the results reported in Fig. 4.7. In particular the difference is about 5% and up to 10% in the mass range $\mathbf{10^{-2} - 1\ M_{\odot}}$ and $\mathbf{10^{-3} - 10\ M_{\odot}}$ for the All and the Bright sample, respectively, with the difference which tends to be larger for small mass values. The larger difference, about 20%, we find for the All sample at $\mathbf{10^{-3}}$ and $\mathbf{10\ M_{\odot}}$ should, as above, be traced back in the drop of the expected MACHO lensing signal to a level almost compatible with the self-lensing one.

4.4.4.4 The projected velocity: the case of OGLE-SMC-02

Although the likelihood analysis is driven by the characteristics of the observed events, it remains a statistical approach on a full set of events. Further insight into the nature of the lenses can be gained for those events for which additional information is available. Within the present set of events this is specifically the case for the long duration ($\boldsymbol{t_E = 195.6}$ **d**) OGLE-SMC-02 candidate event. As discussed in Section 4.3, Dong (2007) did conclude strongly in favor of the MW MACHO nature of this event. In general, the analysis of the MACHO hypothesis suffers from the degeneracy within the lensing parameter space of the unknown lens mass. As apparent also from inspection of the differential rate distribution, Table 4.2 and Fig. 4.5, a long duration event as OGLE-SMC-02 might indeed be explained

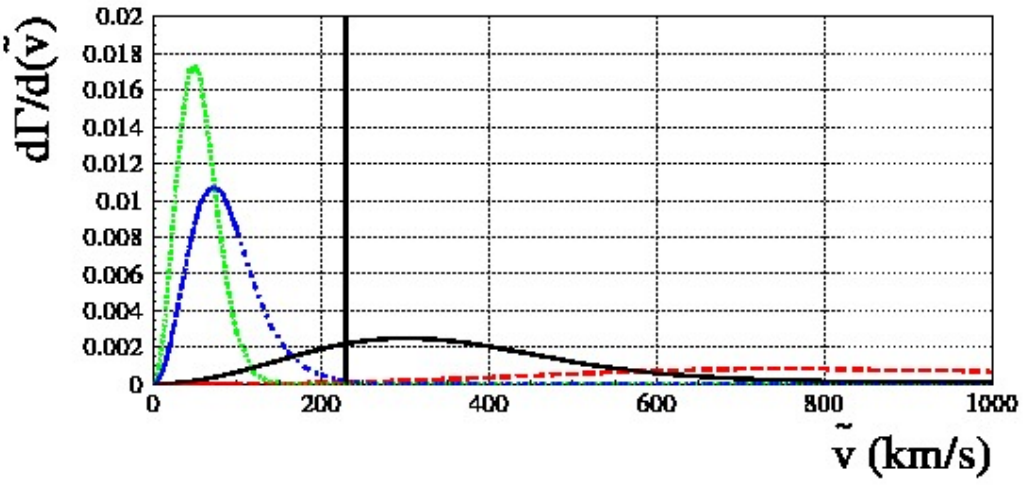

Figure 4.8: Normalized differential rate $\mathbf{d\Gamma/d\tilde{v}}$, where $\tilde{v} = v/(1 - D_l/D_s)$ is the projected velocity, along the line of sight of OGLE-SMC-02 microlensing candidate event ($t_E = 195.6$ d). In particular we show the result for different lens populations: MW thin disc, MW thick disc, SMC self lensing and MW MACHO lensing (dotted, dash-dotted, dashed, solid lines, respectively). The vertical solid line represents the estimated observed value.

by a heavy ($\sim (1-10)\,M_\odot$) MACHO, possibly a black hole, however this statement is subject to an hypothesis on the lens mass. The additional information available for this event allowed Dong (2007) to get rid of this hypothesis. In particular, they were able to provide an estimate of the projected velocity (Gould, 1994) $\tilde{v} = v/(1 - D_l/D_s)$, a quantity which is only weakly dependent on the lens mass (and altogether independent if assuming a delta mass function), with $\tilde{v}_{obs} \sim 230$ km s^{-1}. We have evaluated the expected differential distribution for $\mathbf{d\Gamma/d\tilde{v}}$ given our fiducial model for the SMC self-lensing, MW disc and MW MACHO populations (from Eq. 4.7, we evaluate $\mathbf{d\Gamma/d\tilde{v}} = \mathbf{d\Gamma/dv} \times (1 - D_l/D_s)$). The result of this analysis is reported in Fig. 4.8. At glance, the estimated observed value, $\tilde{v}_{obs}$, is in good agreement with the MW MACHO lensing population projected velocity distribution and at odds with that of the self-lensing populations. In particular, the probability to get a smaller (larger) value than $\tilde{v}_{obs}$ is below 1% for SMC star (MW disc) lenses.

Looking back to the initial issue, the nature of the observed events, we have therefore shown that, although the bare number of observed versus expected events may suggest that all

of them may be attributed to self-lensing populations, a more through analysis, considering the full set of available event characteristics, leads us at very least to soften this conclusion. On the other hand, if any, the extent of the MACHO population compatible with the available data would clearly remain very small.

4.5 Comparison to previous analyses

We can compare our results with those presented by the OGLE collaboration, in particular for the OGLE-III SMC All sample data set (Wyrzykowski et al., 2011b). Overall, the upper limits for f we obtain are tighter (in particular we estimate an increase, with respect to their results, of the expected number of MACHO events driving the upper limit statistics of about 60%), however, we get to only partly understand the underlying reason of this disagreement. OGLE bases his statistical analysis on the following approximated estimate of the expected number of (Galactic) MACHO lensing events (Tisserand et al., 2007) (we recall in particular the underlying assumption $< \mathcal{E} >= \mathcal{E}(< t_{\rm E} >)$ which becomes less and less accurate moving to small values of the MACHO mass for which the resulting differential rate, $\mathbf{d}\Gamma/\mathbf{d}t_{\rm E}$ is significantly different from zero just where the efficiency is negligible)

$$N_{\rm exp} = \frac{2}{\pi} N_{\rm obs} T_{\rm obs}\, \tau\, \frac{\mathcal{E}(< t_{\rm E} >)}{< t_{\rm E} >}\,. \tag{4.10}$$

OGLE then derives the upper limit on f following the recipe of Feldman & Cousins (1998) for a Poisson statistics with a background as that we have carried out in Section 4.4.3 with the assumption that the mean value of the expected background signal (self lensing) is equal to the observed number of events. As discussed in Section 4.4.4.3, comparing to the likelihood, this analysis tends to give more conservative upper limits whenever the two analyses are carried out with coherent values of the expected self-lensing signal. The hypothesis of

OGLE, which in this case overestimates the expected background, drives however the limits much closer to the ones we obtain with the likelihood analysis. Here comes the second caveat, regarding Eq. 4.10, as OGLE uses for τ and $< t_{\rm E} >$ values from previous analyses carried out towards the LMC, specifically $\tau = 4.7 \times 10^{-7}$, for a full MACHO halo, with the Einstein time scaling with the lens mass as $< t_{\rm E} >= 70 \sqrt{m}$ (Wyrzykowski et al., 2010, 2011b). According to our analysis the corresponding, average, values should read instead $\tau = 6.3 \times 10^{-7}$, for a full MACHO halo towards the SMC, with $< t_{\rm E} >= 66 \sqrt{m}$, which overall makes a relative increase, for the expected number of events, of about 40%. For reference we also note that, when considering the line of sight towards the LMC, coherently with these values towards the SMC, one should rather use $\tau = 4.5 \times 10^{-7}$ and $< t_{\rm E} >= 62 \sqrt{m}$ (Calchi Novati et al., 2009; Calchi Novati & Mancini, 2011). As for the LMC, the difference from previous values follows from the assumed distance to the Galactic center, **8 kpc** rather than **8.5 kpc**, and from the inclusion, within the likelihood analysis, of the components of the bulk motion of the relative velocity.

It is also interesting to compare the line of sight towards the SMC to that towards the LMC. Here again we take advantage of the OGLE-III analysis (Wyrzykowski et al., 2011a), which we also have discussed in Calchi Novati & Mancini (2011), to carry out an homogeneous comparison. As for the MACHO lensing signal it is useful again to start from Eq. 4.10. The LMC counts almost 4 times more numerous source stars, which more than compensates the decrease in the ratio $\tau / < t_{\rm E} >$ discussed above. Based on these terms, fixed $T_{\rm obs}$, one should expect almost 3 times more MACHO lensing events towards the LMC than towards the SMC. The efficiency however, at least following the OGLE-III analysis, tends to reduce this difference, especially for the Bright sample (indeed, the efficiency towards the LMC greatly varies from field to field according to the relative crowding, whereas towards the, less crowded SMC fields, it results roughly constant across the monitored fields of view and, especially for the Bright sample, relatively larger). As for self lensing, lensing by SMC stars

is strongly enhanced by the SMC morphology compared to LMC self lensing; on the other hand the overall MW disc lensing signal is relatively much more important for the LMC because of the much larger extension of the monitored field of view. Overall, the expected self lensing signal towards the LMC turns out to be about twice as large as that towards the SMC. Face to these changes in the expected signal, the observed rate, for the OGLE-III analysis, turns out, with the caveat of the small statistics, to be fully compatible towards the two lines of sight: for the All sample, 2 (3) candidate events are reported towards the LMC (SMC). These effects therefore combine so that the constraints on f from the LMC turns out to be tighter.

4.6 Conclusions

In this paper we have discussed the results of the microlensing campaigns carried out towards the SMC by the EROS (Tisserand et al., 2007) and the OGLE collaboration (Wyrzykowski et al., 2010, 2011b). In particular, we have addressed the issue of the nature of the lens of the observed events, either to be attributed to "self lensing", where the lens belong to some luminous component (either of the SMC or of the MW disc) as opposed to MACHO lensing from the putative population of dark matter compact halo objects of the MW. To this purpose we have carried out analyses of the microlensing optical depth and of the expected signal based on the evaluation of the microlensing rate.

Overall, 5 microlensing candidates have been reported (1 each by EROS-2 and OGLE-II and 3 by OGLE-III). Whereas in term of number of events this may be fully explained by the expected self-lensing signal (out of which about 90% is expected from SMC self lensing), the analyses based on the event characteristics, line of sight position and duration, and for one event on the evaluation of the projected velocity, rather suggest that not all the events may be attributed to this lens population. In particular 2.1 (1.4) self lensing events

are expected, to be compared to 4 (3) observed events, depending on the sample of sources considered. Two events (both reported by OGLE-III) have durations lying outside the 95% limits of the expected self-lensing signal (one shorter, one longer). The long duration event is the same for which the projected velocity analysis, which strongly favor a non-self lensing nature of the lens, has been carried out Dong (2007). Additionally, we have discussed the spatial distribution of the observed events as compared to the profile of the SMC self lensing optical depth. Finally, both the event line of sight position and duration enter the likelihood analysis. Taking into account the expected signal of the self-lensing and MACHO lensing populations this allows us to quantify the resulting upper limit on the halo mass fraction in form of MACHOs, $\boldsymbol{f}$. In particular it results that the upper limit at 95%CL is lowest, about 10%, at $\mathbf{10^{-2}\,M_{\odot}}$, and then reduces to above 20% for $\mathbf{0.5\,M_{\odot}}$ MACHOs. Overall, these limits are somewhat less tight than those obtained by analogous analyses carried out towards the LMC (Tisserand et al. 2007; Wyrzykowski et al. 2011a) where, also compared to a somewhat larger expected signal in term of MACHO lensing events, the number of observed events is not correspondingly larger. Larger set of events, hopefully available in the next future thanks to the ongoing OGLE-IV and MOA-II campaigns should provide further insight in this problem.

The expected SMC self-lensing signal is driven by the underlying model of the SMC luminous components for which, in this work, we have taken advantage of several recent analyses (Bekki & Chiba (2009); Subramanian & Subramaniam (2012); Haschke et al. (2012) and references therein), which however still do not provide a full coherent picture of its formation history, dynamic and morphology. Among the more relevant quantities for microlensing purposes, the value for the line of sight depth seem quite well established. There remain however still open questions as the overall luminous SMC mass and the exact balance between the old and the young star populations. A correct model for the SMC luminous remains a key issue for the understanding of the microlensing signal. Indeed, a larger set of events

would make even more important a detailed knowledge of the SMC morphology, providing a further relevant tool of analysis to address the issue of the lens nature.

Chapter 5

Cosmic Microwave Background Radiation. HEALPix maps.

5.1 Cosmic Microwave Background Radiation.

Modern cosmology has undergone an essential progress during the last 10-20 years, entering a phase of so-called precision cosmology. Now it is possible to formulate and study problems with a precision not reachable earlier. This concerns many aspects of the early evolution of the Universe, its present content and structure. New and far more accurate experiments, ground based and , on-board satellites, have supplied the precious data and thus, have determined the present achievements.

The study of Cosmic Microwave Background Radiation (CMB) is one of the most quickly developing areas of modern cosmology, as one of the experimental pillars of a broadly accepted cosmological model of the Big-Bang (Penrose, 1968, 2004; Peebles, 1980; Kolb & Turner, 1990). This model predicts that $\sim$ **14** billion years ago our universe was very hot and small. Then it has expanded from this hot dense condition into much cooler and loose state that we have today. Big Bang theory predicts that the universe should be filled with radiation left from the hot dense matter, the cosmic microwave background radiation, as a cooled remnant heat left over from the Big Bang. CMB is visible to microwave detectors as

a homogeneous and isotropic glow across the entire sky (White et al., 1994; Smoot, 1995).

Historically, the existence of CMB was predicted in 1946-1948 by Gamow and collaborators (Gamow, 1946; Alpher, 1948), but this profound hypothesis was practically forgotten until 1964, when CMB was detected accidentally by Penzias and Wilson (Penzias & Vilson, 1965). They measured a radiation of extraterrestrial origin causing an additional incomprehensible temperature of their detector.

Accordingly, in the very early Universe the temperature was so high that the matter was fully ionized. It adiabatically cooled down as expands, until the first atoms are formed the radiation was steadily Compton scattered, the matter and photons were in thermal equilibrium, and the universe was opaque to the photons. When the temperature fell below 3000 K, electrons and protons combine and form atoms. The Universe with mainly neutral atoms becomes transparent for photons. This decoupling happened when the universe was $\sim \mathbf{300,000}$ years old, at redshift $z \simeq \mathbf{1100}$. Photons began to propagate freely, and with universe expanding, they continued the cooling. Today's temperature of CMB is approximately 2.7 K. The surface when the decoupling happened is called the surface of last scattering. So, the radiation from that surface, traveled about 14 billion years before reaching our detectors, and since the early universe was in thermal equilibrium, the CMB must have strictly black-body spectrum. This was known by early 1990s (Peebles, 1993; Landau & Lifshitz, 1989) and was confirmed by observations.

The last 20 years were marked by a number of significant experiments which produced large amount of accurate data and along with other observations, allowed to turn the above picture to a level of precision cosmology.

During several decades since the very discovery of CMB, the experimenters were searching for the anisotropies in the CMB radiation. The dipole anisotropy (anisotropy of the level of $\mathbf{10^{-3}}$) was securely detected already in 1977 (Smoot et al., 1977) and is due to the motion of the Earth (detector) with respect to the CMB frame. Without the dipole anisotropy, the

CMB signal is isotropic in all directions with precision $\mathbf{10^{-5}}$. The quadrupole anisotropy however has to describe the primordial structure of cosmological density inhomogeneities, which later would have led to the formation of contemporary structure of galaxies and galaxy clusters. The first secure detection of small-scale quadrupole anisotropy was due to Cosmic Background Explorer (COBE) satellite in 1992: upper limit of anisotropy was established at 100 $\boldsymbol{\mu K}$ at about 30 $\boldsymbol{\mu K}$ amplitude (Mather et al., 1990; Smoot et al., 1992; Tegmark et al., 1996).

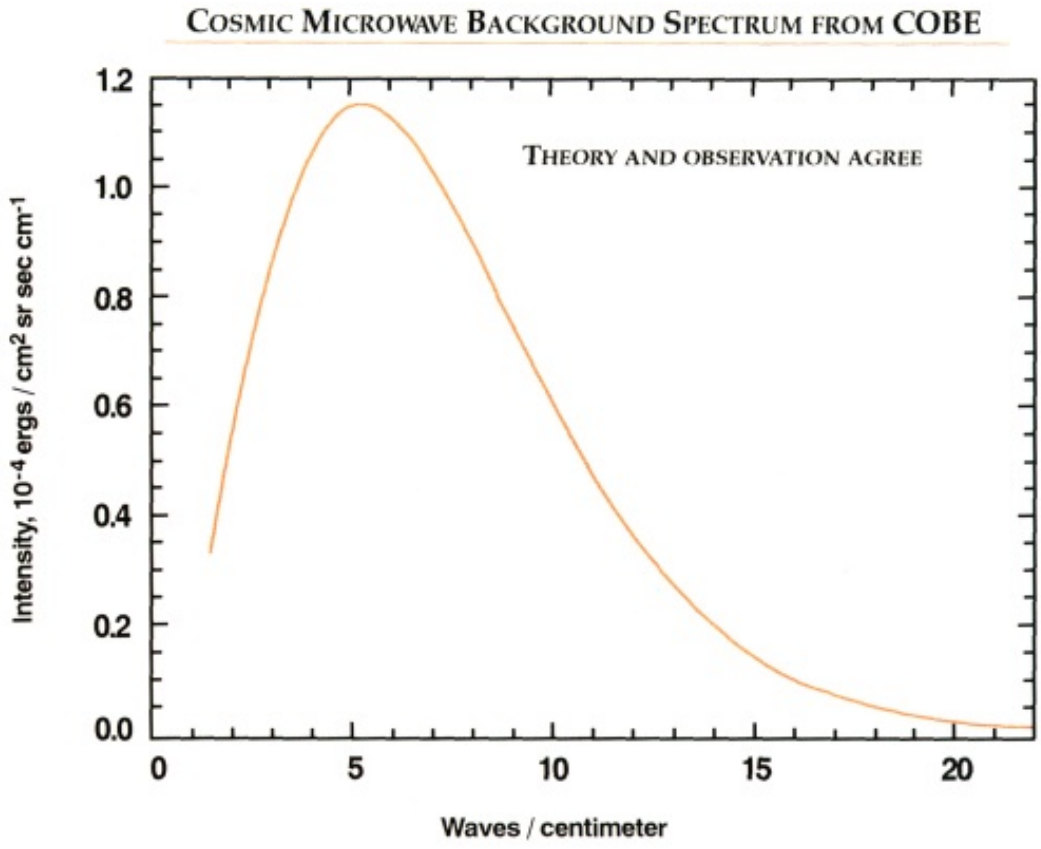

Figure 5.1: The cosmic microwave background spectrum measured by the COBE satellite. The data points and error bars are so small, that are obscured by the theoretical curve. This image is taken from the web page (7).

COBE's CMB spectrum perfectly coincides with black-body spectrum with a temperature of **2.728 ± 0.002** K (see Fig. 5.1), spectral deviations from Planck spectrum were less than 0.005 %. By mapping the dipolar variation in the CMB's temperature across the sky, COBE determined Earth's velocity with respect to the cosmic rest frame to a precision of 1 %. COBE's results led to a major advance in cosmological studies.

The next breakthrough was due to a series of balloon-borne and ground based experiments performed since COBE: MAXIMA, BOOMERanG, DASI, CBI, ARCHEOPS and others (Alsop et al., 1991; Lee et al., 2001; Abroe et al., 2002). BOOMERanG (Balloon Observations of Milimetric Extragalactic Radiation and Geophysics) balloon-borne experiment measured CMB temperature anisotropies with high signal to noise ratio during flight in Antarctica in 1998 and 2004 (de Bernardis et al., 2000, 2003). This experiments produced high quality maps of CMB anisotropies for about 2 % of the sky with angular resolution 7 arcmin (35 times higher then that of COBE) at 90, 150, 240 and 410 GHz. Results of the measurements combined with other experimental data, via the power spectrum indicate that, the geometry of the universe is close to the flat.

The data used in this thesis to show the possible detection of the dark halo of the galaxy are due to the most profound up to now experiment, the Wilkinson Microwave Anisotropy Probe (WMAP) satellite (Bennet et al., 2003; Spergel et al., 2007). It measured CMB anisotropies of the full sky and provided more precise values for cosmological parameters, that have been extracted from previous measurements. WMAP provided full sky CMB maps at 10 different bandwidths. In Fig. 5.2 we demonstrate an example of the WMAP 94 GHz map.

WMAP produced accurate and precise power spectrum of CMB, determining the positions of acoustic peaks, which allow the extraction of cosmological parameters, especially, when combined with the data on distant supernovae, nucleosynthesis, large scale galaxy surveys, gravitational lensing (Dodelson, 2003).

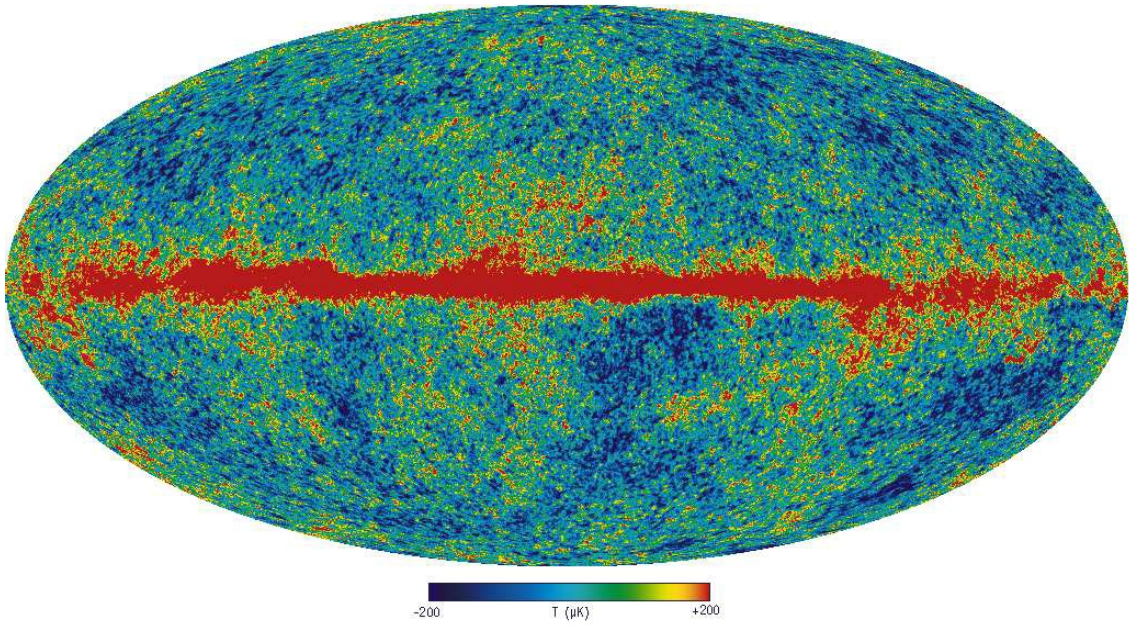

Figure 5.2: The temperature map of the Cosmic Microwave Background radiation measured by the Wilkinson Microwave Anisotropy Probe (WMAP, NASA) satellite at 94 GHz (Jarosik et al., 2007).

Simultaneously to the mentioned CMB experiments, the observations of distant supernovae of type Ia (Perlmutter et al., 1999; Riess et al., 1998; Tonry et al., 2003) showed that, the global mass/energy content of the Universe, and thus its dynamics is dominated by repulsive so-called dark energy, which accounts about 72% of the current mean density. Einstein's cosmological constant, $\mathbf{\Lambda}$ (Einstein, 1917; Landau & Lifshitz, 1989), is one special, and viable case. Another way to constrain $\mathbf{\Lambda}$ is the gravitational lensing (Kochanec, 1996; Falco & Kochanec, 1998), which gives $\mathbf{\Omega_\Lambda \simeq 0.74}$ at 2-$\boldsymbol{\sigma}$ confidence level. The nature of the dark energy, including its redshift evolution, is one of the outstanding problems of modern physics and astrophysics.

The mentioned observational data, combined with those of the cosmological nucleosyn-

thesis and large scale structure, lead to the concordance model with the following content of the Universe. The baryonic matter constitutes about 4-5 %, and includes, particularly, the matter of stars and planets; stars only yield about 0.5 %. The dark matter, is different than atoms, i.e does not absorb or emit light, and comprises about 23 % and has been detected indirectly, only by its gravity. The major part of the Universe, about 72 % is the mentioned dark energy.

5.2 HEALPix maps.

Data on the cosmic microwave background (CMB) radiation had a big role on the understanding of a variety of physical processes in the early phases of the Universe and on the estimation of the cosmological parameters. The WMAP data is one of the most precise data up to now. Moreover, recently De PAolis et al. (De Paolis et al., 2011, 2012) showed the possibility of detection of the galactic disk and halo on CMB. In their analysis, they used WMAP bands (W, V, and Q) maps HEALPix - the Hierarchical Equal Area iso-Latitude Pixelization (Górski et al., 1999) - representation.

The HEALPix package provides an convenient instrument for digitizing and manipulating with any spherical cart, including CMB maps. It is a mathematical structure which supports a suitable discretization of functions on a sphere at sufficiently high resolution, and to facilitate fast and accurate statistical and astrophysical analysis of massive full-sky data sets.

Satellite missions to measure the cosmic microwave background (CMB) anisotropy - NASA's currently operating Microwave Anisotropy Probe (MAP), and the ESA mission Planck - will produce multi-frequency data sets sufficient for the construction of full-sky maps of the microwave sky at an angular resolution of a few arcminutes. Hence, the HEALPix is powerful tool for this purposes.

As a coordinate system the HEALpix pixelization produces splits of a spherical surface.

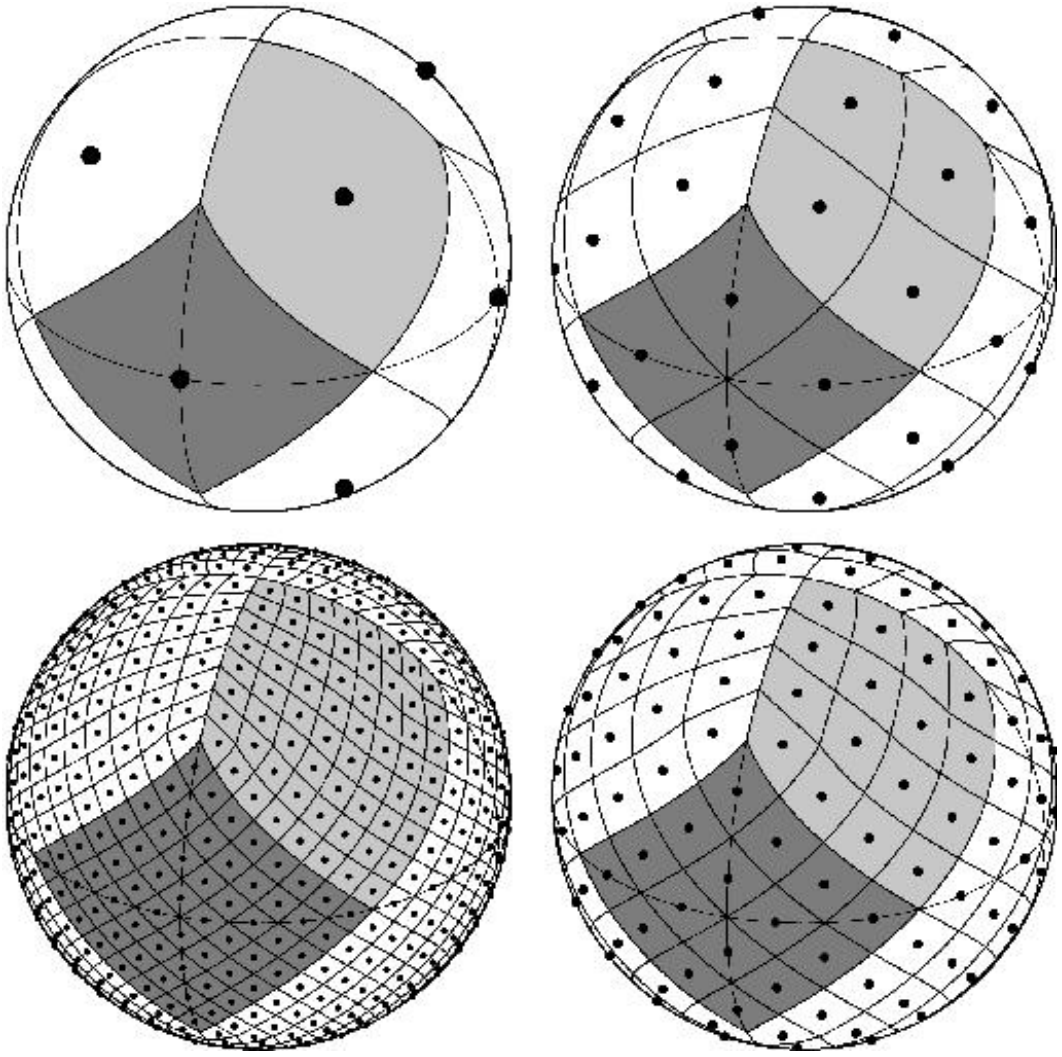

Figure 5.3: Orthographic view of HEALPix partition of the sphere (Górski et al., 1999). Over-plot of equator and meridians illustrates the octahedral symmetry of HEALPix. Light-gray shading shows one of the eight (four north, and four south) identical polar base-resolution pixels. Dark-gray shading shows one of the four identical equatorial base-resolution pixels. Moving clockwise from the upper left panel the grid is hierarchically subdivided with the grid resolution parameter equal to N_{side} = 1, 2, 4, 8, and the total number of pixels equal to $N_{pix} = 12 \times N_{side}^2$ = 12, 48, 192, 768.

The Fig. 5.3 illustrates the separation scheme of a sphere by HEALPix system. We see the increase of resolution from one sphere to another (Fig. 5.3). The initial sphere illustrates the lowest resolution possible, with the HEALPix base separating scheme of the

sphere surface into 12 equal sized pixels (base pixels). The following sphere has a HEALPix net of 48 pixels, the third one has 192 pixels, and the fourth sphere is covered by 768 pixels.

Chapter 6

Possible detection of the M31 rotation in WMAP data[1]

6.1 Introduction

Galaxy rotation, in particular for the Andromeda galaxy (M31) has been well studied especially in the optical, IR, and radio bands, and it gives important information on the mass distribution not only in galactic disks but also in their halos (Binney & Merrifield, 1998). On the other hand, since they are not directly observable, but their presence is deduced from their effect on galactic dynamics, galactic halos are relatively less studied structures of galaxies. Various populations, such as globular clusters, RR Lyra, sub-dwarfs, and other types of stars, have been used to trace the halo of the Galaxy, its vertical structure, and its rotation speed (Kinman et al., 2004). Nevertheless, there are still many ambiguities not only in the main halo constituents, but also in the basic properties such as, in particular, in rotation.

The degree to which galactic halos rotate with respect to the disks is difficult to investigate; actually, as stated in the most recent study of M31 (Courteau et al., 2011), testing for the rotation of M31's halo is still beyond our reach. Naturally, the importance of understanding the galactic halos is closely related to the nature and distribution of the dark matter,

[1]This chapter was previously published in A&A, 534, L8, 2011

which is relevant for the formation and dynamics of galaxies. In this respect, the methodology adopted in the present paper of using WMAP data to probe both the disk and the halo of M31, even if with the limitation of the presently available data, may suggest a novel way of approaching this problem.

6.2 The 7-year WMAP analysis

In our analysis we use the seven-year WMAP data (Jarosik et al., 2011) in the three bands W (94 GHz), V (61 GHz), and Q (41 GHz). Using three WMAP bands is important in revealing the possible contribution of the Galactic foregrounds since dust, free-free, and synchrotron emission contributes differently in each band. Here we remind the reader that the band least contaminated by the synchrotron radiation of the Galaxy is the W-band, which also has the highest angular resolution.

The CMB map's general structure in the W-band in the region of M31, with the marked $\mathbf{4^0}$ radius circle (although our analysis extends farther out), is shown in Fig. 6.1 (left panel). In our analysis, we also used the maps provided by the WMAP Collaboration with the Galactic disk contribution modeled and removed (Gold et al., 2011). It is always specified in the text when we considered these data. To reveal the different contributions by the M31 disk and halo, the region of the sky around the M31 galaxy was divided into several concentric circular areas as shown in Fig. 6.1 (right panel). In the optical band the total extent of the M31 galaxy along the major axis is slightly more than about $\mathbf{3^0}$ and along the minor axis is about $\mathbf{1^0}$. Radio observations have shown that the M31 HI disk is more extended with respect to the stellar disk (Chemin et al., 2009; Corbelli et al., 2010) , with a major axis sizes of about $\mathbf{5.6^0}$ and a minor axis size of about $\mathbf{1.2^0}$. In this paper, the adopted M1 and M2 disk regions (Fig. 6.1, right panel) have major axis size of $\mathbf{8^0}$ and minor axis size of $\mathbf{1^0}$; this allows us to retain the warped part of the M31 disk in the M1 and M2 regions. Moreover, we have checked that it is irrelevant, as far as our analysis is concerned, to extend the M31 minor axis

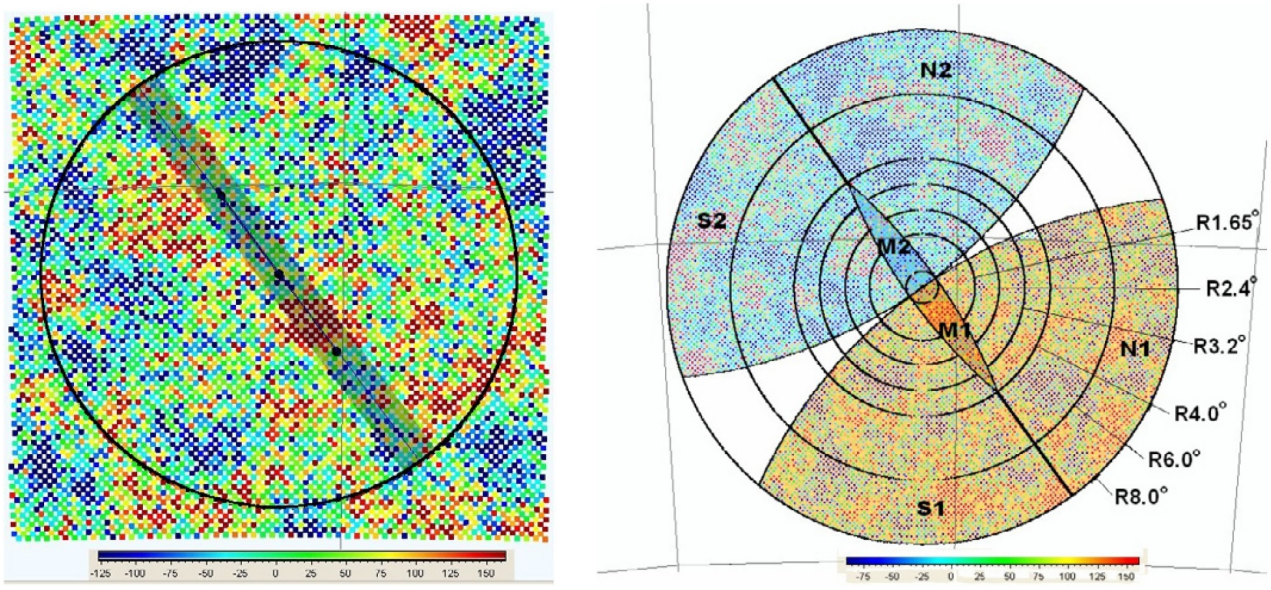

Figure 6.1: In the left panel, the WMAP W-band towards the M31 galaxy. The $\mathbf{8.5^0 \times 8.5^0}$ sky field centered at $\mathbf{(121.17^0, -21.57^0)}$ with the marked $\mathbf{4^0}$ circular region. The oblique strip indicates the M31 disk, and the analysis in the halo region of M31 galaxy is extended far beyond the region indicated in the figure. The detailed geometry (up to $\mathbf{8^0}$) used in the analysis is shown in the right panel.

to $\mathbf{1.2^0}$. The mean temperature excess per pixel $\boldsymbol{T_m}$, in μK/pixel, in each region was obtained in each band and is shown in Table 1 with the $\mathbf{1}\sigma$ error [2] , along with the number of pixels in each area. For convenience, Table 1 gives the temperature excess in each M31 region up to $\mathbf{8^0}$, even if our analysis was extended to the region around the M31 disk with concentric annuli with radii up to $\mathbf{20^0}$.

[2]The standard error of the mean is calculated as the standard deviation of the excess temperature distribution divided by the square root of the pixel number in each region. We have verified that, within the errors, the sigma values calculated in that way are consistent with those evaluated by using the covariance matrix obtained by a best-fitting procedure with a Gaussian to the same distribution.

Table 6.1: Temperature excess in the M31 regions for the non foreground-reduced WMAP maps.

R, deg, kpc	Region	N, pix	W, $T_m \pm \sigma$	V, $T_m \pm \sigma$	Q, $T_m \pm \sigma$
1.65, 21.4	N1 + M1 + S1	324	**63.1 ± 5.6**	**67.2 ± 5.4**	**90.0 ± 4.2**
	N2 + M2 + S2	321	**20.3 ± 4.7**	**17.3 ± 4.3**	**37.0 ± 3.3**
	N1 + S1	205	45.5 ± 5.7	38.0 ± 5.3	64.1 ± 4.0
	N2 + S2	205	33.8 ± 5.9	34.3 ± 5.3	41.8 ± 4.1
	M1	119	**121.4 ± 19.6**	**117.6 ± 10.0**	**134.3 ± 7.4**
	M2	116	**−7.7 ± 7.4**	**−12.7 ± 6.8**	**28.4 ± 5.5**
2.40, 31.1	N1 + M1 + S1	670	**43.7 ± 3.6**	**43.5 ± 3.4**	**66.0 ± 2.8**
	N2 + M2 + S2	664	**21.0 ± 3.6**	**19.1 ± 3.3**	**35.6 ± 2.7**
	N1 + S1	506	41.0 ± 3.5	32.2 ± 3.1	55.6 ± 2.6
	N2 + S2	504	24.5 ± 4.3	23.6 ± 3.9	34.8 ± 3.3
	M1	164	**73.0 ± 9.4**	**78.3 ± 9.3**	**98.2 ± 7.4**
	M2	160	**11.2 ± 6.3**	**5.8 ± 6.4**	**38.1 ± 4.8**
3.20, 41.5	N1 + M1 + S1	1176	**36.5 ± 2.7**	**38.9 ± 2.4**	**59.6 ± 2.1**
	N2 + M2 + S2	1166	**16.0 ± 2.7**	**11.3 ± 2.5**	**30.3 ± 2.2**
	N1 + S1	980	35.3 ± 2.7	34.0 ± 2.3	53.9 ± 2.1
	N2 + S2	976	16.4 ± 3.0	11.5 ± 2.8	27.7 ± 2.4
	M1	196	**63.8 ± 8.4**	**63.2 ± 8.3**	**88.1 ± 6.6**
	M2	190	**12.5 ± 5.8**	**10.3 ± 5.8**	**44.0 ± 4.4**
4.00, 51.9	N1 + M1 + S1	1818	**37.4 ± 2.2**	**39.6 ± 2.0**	**56.7 ± 1.7**
	N2 + M2 + S2	1808	**1.7 ± 2.3**	**−2.4 ± 2.1**	**16.9 ± 1.9**
	N1 + S1	1610	36.8 ± 2.2	36.9 ± 1.9	53.3 ± 1.7
	N2 + S2	1609	− 0.4± 2.5	− 3.8 ± 2.2	13.5 ± 1.9
	M1	208	**64.7.0 ± 8.1**	**60.8 ± 7.9**	**83.6 ± 6.4**
	M2	200	**12.5 ± 5.6**	**9.4 ± 5.6**	**43.6 ± 4.3**
6.00, 77.8	N1 + S1	3748	29.7 ± 1.5	27.0 ± 1.4	44.0 ± 1.2
	N2 + S2	3749	11.3 ± 1.7	7.1 ± 1.5	25.8 ± 1.3
8.00, 103.8	N1 + S1	6606	34.3 ± 1.2	34.7 ± 1.1	51.5 ± 4.0
	N2 + S2	6600	19.2 ± 1.3	15.0 ± 1.2	38.7 ± 1.0

Notes. The radius of the considered annulus is given in degrees and in kpc in the first column; the value of 744 kpc (Vilardell et al., 2010) is adopted for the distance to M31. The considered regions as in Fig. 1 (right panel). The numbers of pixels in each region are given. The last three columns show the CMB mean temperatures per pixel of each region in μK in the W, V, and Q bands, respectively, with the corresponding $\mathbf{1}\sigma$ errors (see text for details).

6.3 Results for the M31 disk

For the M31 disk, our analysis shows that each M1 region is always hotter than the corresponding M2 region, as can be seen from Table 1. Indeed we find a temperature excess contrast (i.e. the difference between the temperature excesses per pixel) between the M1 and M2 regions in all three WMAP bands that turns out to be about **129 ± 21** μK/pixel within 21.4 kpc (in the W band) and then slightly decreases (but remains as large as about **41 ± 10** μK/pixel at about 50 kpc).

This effect seems to come from the rotation induced Doppler shift of the gas and dust emission from the M31 disk - indeed, the hotter (M1) region corresponds to the side of the M31 disk that rotates towards us [3].

If one compares what WMAP data show towards the M1 and M2 regions with the maps of the M31 thick HI disk obtained at 21 cm (Chemin et al., 2009; Corbelli et al., 2010) one sees a remarkable superposition of the hot (M1) and cold (M2) regions in both observations.

Even if the temperature asymmetry between the M1 and the M2 regions looks significant, we have to check whether it might be due to a random fluctuation of the CMB signal. It is indeed well known that the CMB sky map has a "patchy" structure characterized by the presence of many hot and cold spots with temperature excesses up to several tents of μK/pixel on angular degree scales. We therefore considered (Fig. and also the online material) 500 control fields and 500 simulated sky maps (from the best-fitted cosmological parameters as provided in the WMAP web site) [4] - and evaluated the temperature contrast with the same geometry as was used towards M31. We also give (red curve) the M31 temperature contrast

[3] A detailed study of the frequency dependent temperature asymmetry in the CMB arising from different distributions of gas and dust in the M31 disk is left to a forthcoming paper. In any case, although some inhomogeneity in the disk structure is not excluded, there is no reason to assume that it is the sole cause.

[4] CMB maps were simulated by assuming $\Delta T(\hat{n}) = \Delta T_{CMB}(\hat{n}) \otimes B(\hat{n}) + N(\hat{n})$, where ΔT_{CMB} is a realization of the Gaussian CMB field, $N(\hat{n})$ is the pixel noise and $B(\hat{n})$ is the proper beam of the experiment. We made 500 realizations of the CMB sky using `synfast` routine of HEALPix with the best-fit power spectrum as given by the WMAP Collaboration. The maps are then convolved with WMAP beams for W, V, and Q bands, respectively. Noise realizations (simulated with $\sigma_0 = 6.549$ mK, $\sigma_0 = 3.137$ mK, and $\sigma_0 = 2.197$ mK for W, V, and Q-bands, respectively) are added to the beam convolved maps in the end.

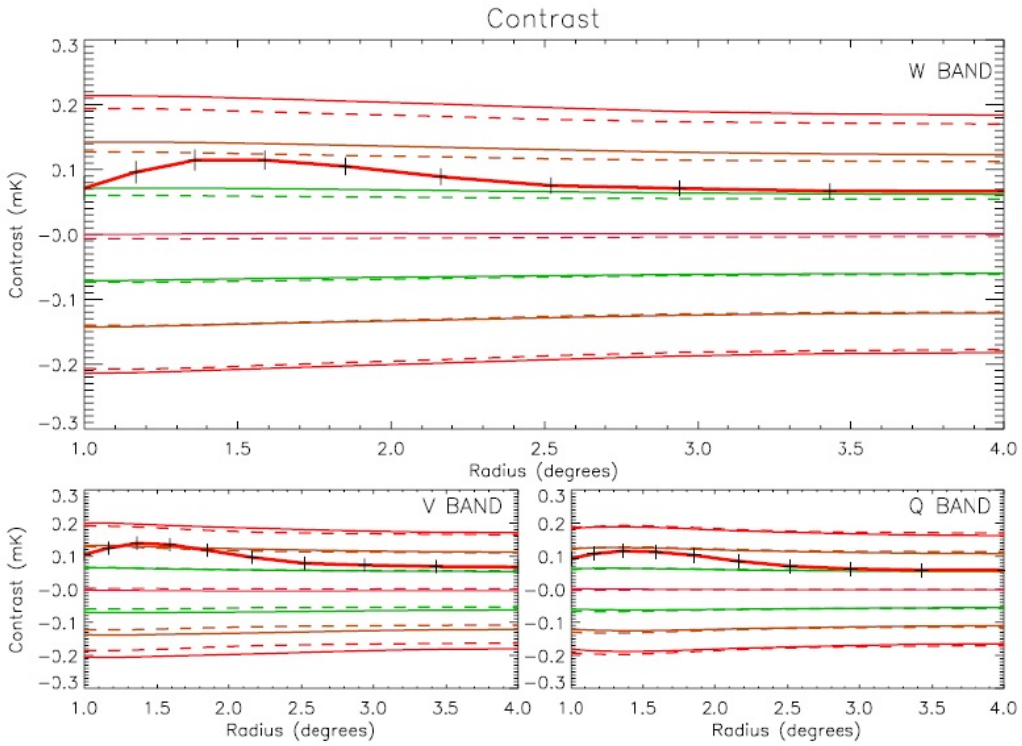

Figure 6.2: The 1σ (green lines), 2σ (brown lines), and 3σ (red lines) excess temperature contrast (in mk/pixel) curves (in the W, V, and Q bands) along with the mean profile (pink line close to zero) for 500 random control fields (continuous lines) and 500 simulated CMB sky maps (dashed lines). In red, the observed temperature contrast profile in the M31 disk (with $\mathbf{1\sigma}$ errors) is given. The WMAP maps with the Galactic disk contribution modeled and removed (foreground-reduced maps) are used here.

profile in the M31 disk. Due to our chosen geometry, each curve is given up to $\mathbf{4^0}$. As one can see, the contrast temperature profile for the M31 disk is always a nicely smooth curve that is close to the $\mathbf{2\sigma}$ curve in the intermediate region of about $\mathbf{1.5 - 2^0}$. Both the control field and the CMB simulation analyses show that there is a probability of less than about **4%** that the temperature asymmetry revealed comes from a random fluctuation of the CMB signal. Actually, if one takes the direction of rotation of the M31 disk into account, such a probability reduces (by using the theorem of the composite probability) by a factor of two. Finally, we mention that we have found that the temperature excess contrast of the two M31

disk regions obtained by dividing the M1+M2 region with respect to the north-west/south-east symmetry axis (the M31 disk axis) turns out to be **0.008 ± 0.012** mK, which seems to further confirm that the temperature contrast between the M1 and M2 regions is not due to a random fluctuation in the CMB signal.

6.4 Results for the M31 halo

The next step was to enlarge our analysis to the region around the M31 disk by considering concentric circular regions of increasing galactocentric radii (see also Fig. 1, right panel). We estimated the difference of the temperature excess in the region N1+S1 in the three WMAP bands with respect to that in the region N2+S2. A temperature contrast between the region N1+S1 with respect to N2+S2 shows up (see Table 1), and the N1+S1 region turns out to always be hotter than the N2+S2 region. The detected effect resembles the one towards the M31 disk, although with less temperature asymmetry. In all three bands, the maximum temperature contrast reaches a maximum at a galactocentric distance of about $\mathbf{4^0}$ and then decreases slightly. It is apparent from the size of the considered regions that a contamination of the M31 disk in the regions N1, N2, S1, and S2 can be completely excluded, and also the Galactic plane emission cannot account for the observed temperature asymmetry since it eventually would make a larger contribution towards the upper regions of M31 (while the opposite is observed in the data). As for the M31 disk, the temperature asymmetry in the M31 halo is indicative of a Doppler shift modulated effect possibly induced by the rotation of the M31 halo.

Also in this case we need to check the robustness of our results; that is, we have to estimate the probability that the temperature asymmetry in the M31 halo is due to a random fluctuation of the CMB signal. In Fig. 6.3 (see also the online material) we have considered 500 control fields and 500 simulated sky maps (from the best-fitted cosmological parameters

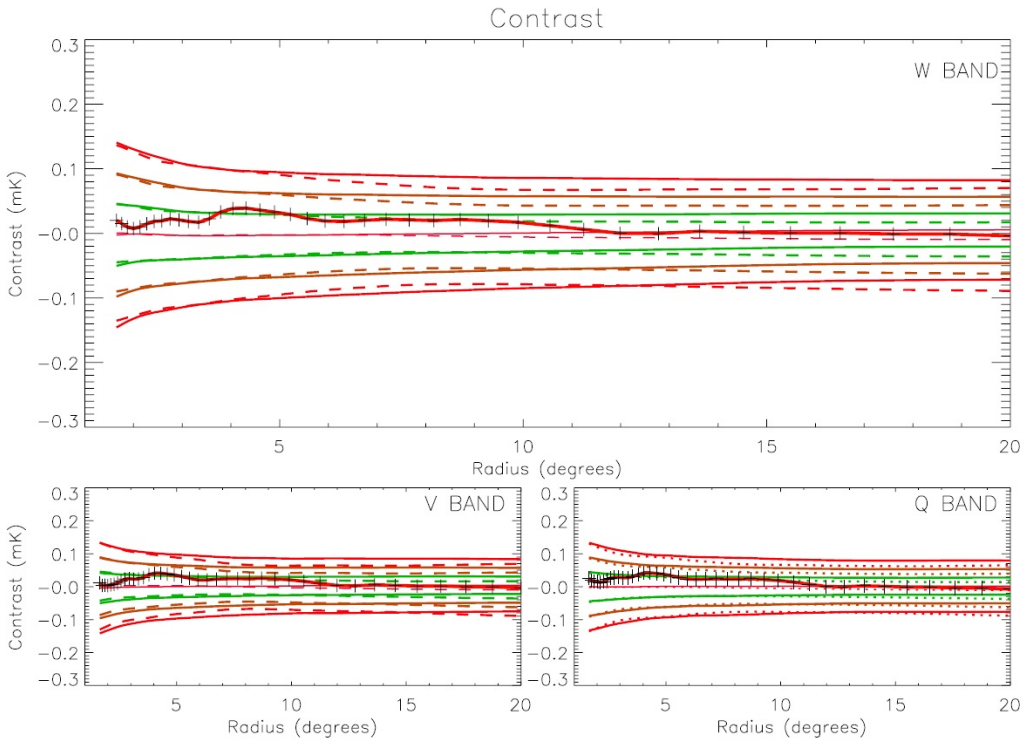

Figure 6.3: The same as Fig. 6.2 but for the M31 halo (temperature contrast of the N1+S1 with respect to the N2+S2 regions in mK/pixel - red line) for 500 random control fields (continuous lines) and 500 simulated sky maps (dashed lines). Here the WMAP maps with the Galactic disk contribution modeled and removed (foreground-reduced maps) are used.

as provided on the WMAP website). As one can see, in all three bands, the contrast temperature profile of the M31 halo is close to the $\mathbf{1\sigma}$ curve up to about $\mathbf{10^0}$ and goes slightly beyond it at about $\mathbf{50-60}$ kpc where the halo effect is maximum. This means that there is less than $\mathbf{30\%}$ probability that the temperature contrast we see towards the M31 halo is due to a random fluctuation of the CMB signal.

We also point out that we have verified that the temperature asymmetry towards the M31 halo vanishes if the adopted geometry is rigidly rotated of an angle larger than about $\mathbf{10^0}$ with respect to the M31 major axis, thus giving a further indication that the halo temperature contrast effect might be genuine and not simply a random fluctuation of the CMB.

We also point out that the use of three WMAP bands is useful for revealing the role of the contribution to the Galactic foregrounds since each emission mechanism contributes differently in each band. That the temperature contrast seems present in all three bands and is more or less the same in each band up to about $\mathbf{10^0 - 11^0}$ indicates that the foregrounds are far weaker than the effect. This size corresponds to the typical size inferred for the dark matter halos around massive galaxies and might open the possibility of a new way of studying these systems, galactic disks, and halos, by using the microwave band. In any case, a careful analysis of the Planck data that will be released shortly should allow either proving or disproving our results.

6.5 Discussion and conclusions

We have shown that a temperature asymmetry in all WMAP bands may exist both in the M31 disk and halo in the direction of the M31 spin. For the M31 disk, the effect is fairly clear, and there is a probability below about **2%** that it is a random fluctuation of the CMB signal. If real, the detected temperature excess asymmetry should be due to the foreground emission of the M31 disk modulated by the Doppler shift of the disk spin. That the present study is really timely is strengthened by considering that the M31 galaxy is already detected by the Planck observatory (Ade et al., 2011) [5], whereas it did not appear in the WMAP list. These are all reasons to expect that the particular effect we discuss here can be studied more accurately with Planck data.

As for the M31 halo, we have shown that, although less evident than for the M31 disk, there is some evidence of a temperature asymmetry between the N1+S1 and the N2+S2 regions that resembles that of a Doppler shift effect induced by the M31 halo rotation. We have shown in the previous section that there is less than about **30%** probability that the

[5]However, there is no mention of any temperature asymmetry in the M31 disk in that paper.

detected temperature asymmetry at a galactocentric distance $\sim$ **50** kpc comes from a random fluctuation of the CMB signal. [6]

If one assumes that this temperature asymmetry in the M31 halo relies in the M31 itself and is related to the M31 halo rotation, one could speculate about the origin of this effect. In general, four possibilities may be considered: (a) free-free emission, (b) synchrotron emission, (c) Sunyaev-Zel'dovich (SZ) effect, and (d) cold gas clouds populating the M31 halo [7]. To work, the first three effects, assume the presence of a rather hot plasma in the halo of M31. Although this hot plasma has not been detected yet, one can assume that a certain amount of this plasma can populate the M31 halo (spiral galaxies are believed to have much less hot gas than elliptic) and may rotate with a certain speed. Free-free emission arises from electron-ion scattering while synchrotron emission comes mostly from the acceleration of cosmic-ray electrons in magnetic fields. Both effects give rise to a thermal emission with a rather steep dependence on the frequency (Bennett et al., 2003) that therefore should give a rather different temperature contrast in the three WMAP bands. The absence of this effect indicates that the contribution from possibilities (a) and (b) should be negligible. And for (c), even for typical galaxy clusters with diffuse gas much hotter than that possibly expected in the M31 halo, the rotational scattering effect would produce a temperature asymmetry of at most a few μK/pixel, depending on the rotational velocity and the inclination angle of the rotation axis (Cooray & Chen, 2002) . Actually, a possible temperature asymmetry in the CMB data towards the M31 halo as a consequence of the existence of a population of cold gas clouds in its halo was predicted in (De Paolis et al., 1995) - possibility (d). Indeed, if the

[6] We also mention that the number and the temperature profile of radio sources in CMB maps (Gurzadyan et al., 2010) excludes their significant contribution in the effect under study.

[7] We also considered the possible influence of the observed high-velocity clouds, either in the M31 or in our galaxy halos (Westmeier et al., 2008; Hulsbosch & Wakker, 1988; Morras et al., 2000) , by removing the pixels in the direction of each cloud from the analysis. The results obtained do not change with respect to those presented here, as expected when also considering the relatively low number of pixels involved. Also the proposed ejecta by the past interaction of M33 and M31 galaxies (Bekki, 2008) cannot play any role in our analysis since it would at most have made hotter some pixels in the S2 region (where the M31-M33 bridge is located), which is instead colder than the S1 one.

halo of the M31 galaxy contains cold gas clouds, we expect them to rotate like the M31 disk (even if, perhaps, more slowly), and thus there should be a Doppler shift inducing a temperature anisotropy ΔT between one side of the M31 halo and the other with respect to the rotation axis perpendicular to the disk. In the case of optically thin halo clouds, the Doppler induced temperature anisotropy would be $\Delta T/T_r \simeq 2vS\,\bar{\tau}/c$, where v is the M31 rotation speed, $\bar{\tau}$ the averaged cloud optical depth over the frequency range ($\nu_1 \leq \nu \leq \nu_2$) of a certain detection band, and S the cloud filling factor, i.e. the ratio of filled (by clouds) to total projected surface in a given field of view. We emphasize that the fact that the temperature contrast in Fig. 6.3 looks approximately the same in each band makes a point towards either possibility (d) or a random fluctuation of the CMB sky (but with a probability, if estimated purely statistically, of less of 30% for the last possibility).

The wealth of data especially in the last decade shows that there is good evidence for the presence in the halos of spiral galaxies of gas in all gaseous phases: neutral, warm atomic, and hot X-ray emitting gas (Bregman, 2007). Atomic gas (often identified as HVCs) is observed in the radio band (particularly at 21 cm) and through absorption lines towards field stars and quasars. The hot gas may be detected in X-rays, while searches for cold gas clouds in galactic halos are more problematic as are searches for them by the presence of a gamma-ray halo (Dixon et al., 1998; De Paolis et al., 1999), stellar scintillations (Moniez, 2003; Habibi et al., 2011) , obscuration events towards the LMC (Drake & Cook, 2003), ortho-H_2D^+ line at 372 GHz (Ceccarelli & Dominik, 2006), and extreme scattering events in quasar radio-flux variations (Walker & Wardle, 1998) have given no clear indication of their presence.

In conclusion, we showed that our analysis based on seven-year WMAP data suggests there is a temperature excess asymmetry in the M31 disk is likely due to the M31 foreground emission modulated by the Doppler shift induced by the M31 spin. We find that there is less than $\simeq 2\%$ probability that the signal up to about 20 kpc comes from a random fluctuation

in the CMB signal. For the M31 halo, we also find a temperature excess asymmetry between the N1+S1 and the N2+S2 regions along the expected spin direction, suggestive of a rotation induced Doppler shift. The effect in the M31 halo is far weaker than for the disk, as obviously expected, and more precise data are necessary before drawing any firm conclusion. In all cases, this research may open a new window into the study of galactic disks and especially the rotation of galactic halos by using the Planck satellite or planned balloon-based experiments.

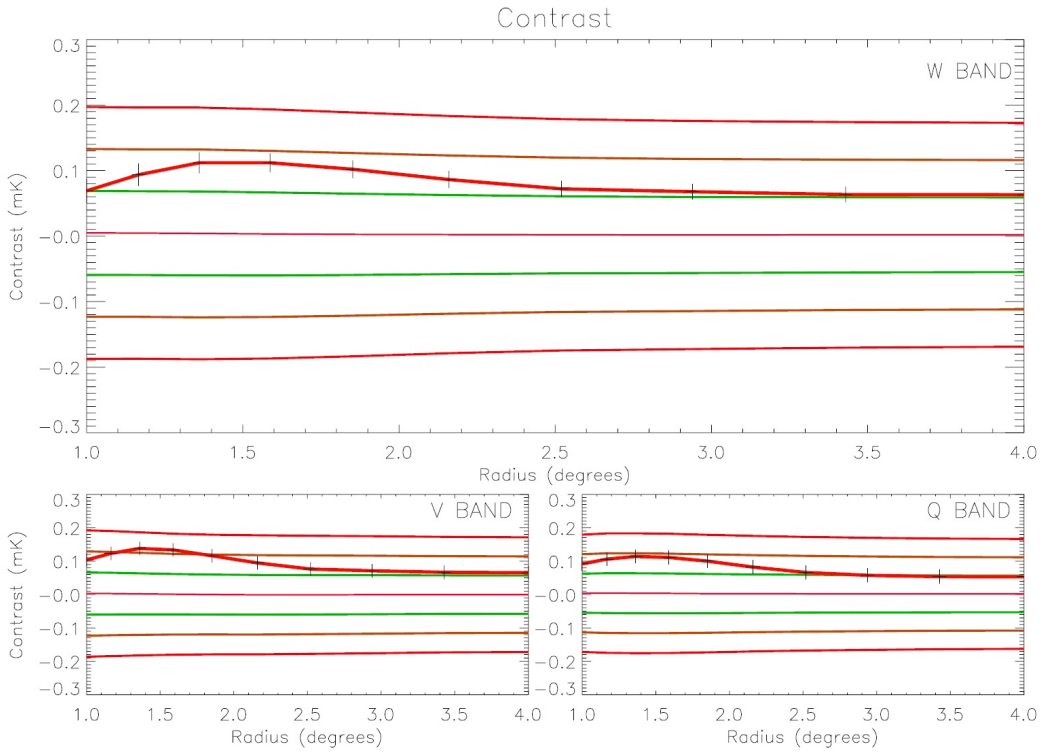

Figure 6.4: In the W, V, and Q bands, the 1σ (green lines), 2σ (brown lines), and 3σ (red lines) excess temperature contrast (in mk/pixel) curves, along with the mean profile (pink line close) for 500 random control fields. The observed temperature contrast profile in the M31 disk (with $\mathbf{1}\sigma$ errors) is given in red. The non foreground-reduced WMAP maps are used here.

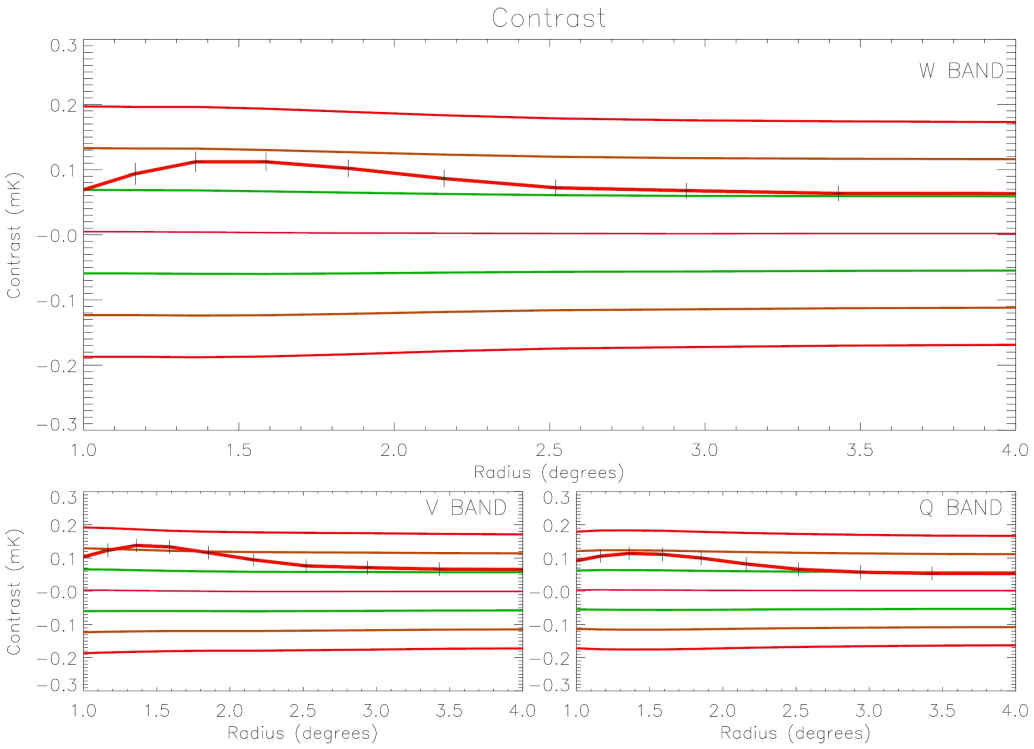

Figure 6.5: As above (in the W, V, and Q bands) the 1σ (green lines), 2σ (brown lines), and 3σ (red lines) excess temperature contrast (in mk/pixel) curves along with the mean profile (pink line close) for 500 random control fields. The real temperature contrast profile in the M31 halo up to $\mathbf{20^0}$ (with $\mathbf{1\sigma}$ errors) is given in red.

Chapter 7

Conclusions

In this thesis we have presented two different topics. One of them concerns to the gravitational microlensing towards the Small Magellanic Cloud and second one is demonstration of the possible detection of galaxy halos using Cosmic Microwave Background Radiation maps. In §7.1, we summarize our results on the new analysis of the results of the EROS-2, OGLE-II, and OGLE-III microlensing campaigns towards the Small Magellanic Clouds. While in §7.2 we discuss the possibility of the detection of the galaxy halos having used CMB as a main tool of investigation.

7.1 Microlensing towards the SMC

We have discussed the results of the microlensing campaigns carried out towards the SMC by the EROS and OGLE collaboration. Specifically we have discussed an issue of the nature of 5 SMC microlensing events whether to be attributed to lenses belonging to known population (SMC itself, MW disk) or to the MW dark halo population. In order to find out the location of the lenses we carried out microlensing statistical analysis, particularly optical dept and number of the expected events analysis, then comparing expected and observed characteristics of events, such as a spatial distribution and duration. We concluded that in therm of number of events the self-lensing alone can explain those 5 events. In particular,

2.1(1.4) self lensing events are expected, to be compared to 4(3) observed events, depending on whether All or Bright samples are considered. But from other side microlensing event characteristics, such as a line of sight position and duration suggest that not all the events may be attributed to the luminous lens population. Particularly, two events, the shortest and the longest one are incompatible with self-lensing scenario expected event duration. Then we have also discussed the spatial distribution of the observed events as compared to the profile of the SMC self lensing optical depth. Furthermore, both the event line of sight position and duration enter the likelihood analysis, which resultes that the upper limit at 95%CL is about 10% and the lowest for $\mathbf{10^{-2}}\boldsymbol{M_{\odot}}$ and above 20% for $\mathbf{0.5}\boldsymbol{M_{\odot}}$ MACHOs. However, our set of 5 events is a few statistics, and in future larger set may help to go deeper in understanding of Galactic halo MACHO fraction and would make even more important a detailed knowledge of the SMC morphology, providing a further relevant tool of analysis to address the issue of the lens nature.

7.2 Dark Halo possible detection using CMB

One of the most remarkable question in the Astrophysics is related to the dark matter. Different approaches have been done to understand how does it distributed and what is the fraction of the dark matter in the Universe. To the purposes of understanding the dark matter distribution in galaxies we have carried out the following analysis. We have used 7-year WMAP data to trace Andromeda galaxy (M31) disk and halo. We have analyzed the temperature excess in three WMAP bands (W, V, and Q) by dividing the region of the sky around M31 into several concentric circular areas. Both cases clearly show temperature asymmetry in the direction of galactic rotation in all bands, in particular, for M31 disk the effect is clear, while for M31 halo it is less remarkable. We have also simulated 500 random control fields in the real WMAP maps and 500 sky maps from the best-fitted cosmological parameters to

analyze robustness of this effect. Quantitatively speaking, we found $\approx$ **2%** and below **30%** probability that the effect is due to the random fluctuation of the CMB signal, for disk and halo, respectively. As the effect of M31 halo is much less weaker than for the disk, more precise data are necessary before drawing any firm conclusion. New data available from *Planck* mission will open a new perspectives into the studies of the galactic disk and especially the rotation of galactic halos, hence contributing in understanding the distribution of the dark matter in the Universe.

Appendix A: The likelihood analysis

The observation of microlensing events follows a Poisson distribution with the expected number determined according to the given model. Suppose we have N_{obs} observed events for an expected signal of N_{exp} events. Introducing a binning of the parameter space which specifies the model we can write down the joint probability distribution for obtaining N_{obs} events, namely the likelihood, as the product over the N_{bin} bins to have n_i observed events for an expected signal x_i, with x_i being the parameter for the Poisson distribution in each separate bin . For a suitable choice of the binning we can then make n_i equal either to 0 or to 1, namely we can get to infinitesimal bins so to have either none or one event per bin (Gould, 2003), which is the second step in Eq. 7.1, whereas in the last step one makes use of the fact that the extent of the bin where no events are observed is indeed overall infinitesimal

$$\begin{aligned} L &= \prod_{i=1}^{N_{bin}} \frac{\exp(-x_i) x_i^{n_i}}{n_i!} = \prod_{i=1}^{N_{obs}} \exp(-x_i)\, x_i \prod_{i \notin (1, N_{obs})} \exp(-x_i) \\ &= \exp(-N_{exp}) \prod_{i=1}^{N_{obs}} x_i \,. \end{aligned} \tag{7.1}$$

In the last term the product runs over the bins containing 1 observed event only. Out of the likelihood, given the prior distribution and by Bayesian inversion, we can build the probability distribution for the parameters of interest. In the following we consider the likelihood as a function of f, the halo mass fraction in form of MACHOs, keeping the MACHO mass fixed as a parameter.

The terms x_i, being related to the expected number of events per bin, are proportional to

the microlensing rate. As a possible approach one can introduce a binning in the duration, $\Delta t_{\rm E}$, and then reduce to Eq. 7.1 by the limit $\Delta t_{\rm E} \rightarrow 0$. In this case $x = {\rm d}\Gamma/{\rm d}t_{\rm E}$, evaluated at the value of the observed durations, $t_{\rm E,obs}$. This is the likelihood expression used, for instance, in the analyses of the MACHO group (Alcock et al. (2000) and references therein). Alternatively, one can directly consider x as the number of expected events per bin evaluated according to Eq. 4.9. This gives the likelihood analysis used, for instance, within the analysis of M31 pixel lensing results of the POINT-AGAPE collaboration (Calchi Novati, 2005). Whatever the choice, the underlying structure of Eq. 7.1 drives the resulting limit on f.

The rate, and therefore the expected number of events, can be looked at as the sum of two terms: the self-lensing contribution plus the MACHO lensing contribution modulated the multiplicative factor f. As a first remark we note that in the exponential term, $\exp(-N_{\rm exp})$, the number of expected self-lensing events drops out as a constant. In particular this implies that for no observed events, either assuming that the observed events are due to self lensing the resulting limits on f are independent from the expected self-lensing signal and are driven by the expected number of MACHO lensing events only. In the more general case of $N_{\rm obs} > 0$, the exponential decrease of f is modulated by $N_{\rm obs}$ factors of the kind $a + fb$, where a and b are constants with respect to f and linked to the expected self-lensing and MACHO lensing signal, respectively. To the purpose of the evaluation of the probability distribution for f, $P(f)$, only the ratio b/a matters so that whatever factor coming in front of both of them drops out in the normalization of $P(f)$. In particular, for the choice mentioned above, $x = {\rm d}\Gamma/{\rm d}t_{\rm E}$, when calculating the differential rate at the observed duration value, the efficiency term $\mathcal{E}(t_{\rm E})$ does drop out (being usually given as a unique function for all the lens populations considered). On the other hand, when considering for x the number of expected events, the efficiency $\mathcal{E}(t_{\rm E})$ enters in an essential way, whereas the constants that drop out are the number of sources and the overall time span of the experiment, so that in particular one can consider, for instance, as the infinitesimal bin choice, the lines of sight corresponding

to each observed event. It is also important to keep trace that in these two cases one is in fact weighting the event characteristics in a different way. In the first case, both the event line of sight position and the duration enter the likelihood (with the relevant caveat that the duration is not modulated by the detection efficiency). In the second, the results are driven specifically by the expected number of events within the chosen bins, namely the line of sight position. The outcome is therefore expected to be more similar to the analysis carried out based on the number of events according to the Poisson distribution. This is not surprisingly as the underlying statistics is the same, with the important caveat, however, that within this likelihood-based analysis also the observed event spatial distribution is included within the analysis.

In the present analysis we consider the joint results from more than one experiment. In this case the probabilities, and therefore the different likelihood term, multiply. Each experiment is characterized by his own number of expected events and this fixes, through the exponential term in the likelihood, the relative weight of each of them. On the other hand, all the reported events, appearing in the product, enter the likelihood on the same footing.

Bibliography

Abroe M. E. et al., 2002, MNRAS, **334**, 11

Ade P. A. R. et al., (Planck Collaboration), 2011, A&A, **536**, A16

Afonso C., Alard C., Albert J. N. et al., (EROS), 1999, A&A, **344**, L63

Afonso C., Albert J. N., Andersen J., Ansari R., et al., 2003, A&A, **400**, 951

Albrow M. D., Beaulieu J.-P., Caldwell J. A. R., Depoy D. L., et al., 1999, ApJ, **512**, 672

Alcock C., Allsman R.A., Alves D.R. et al., 2000, ApJ, **542**, 281

Alcock C., Allsman R. A., Axelrod T. S. et al., 1995, ApJ, **449**, 28

Alcock C., Allsman R. A., Alves D. R., Axelrod T. S., et al., 1999, ApJ, **518**, 44

Alcock C., Allsman R. A., Alves D. et al., (MACHO) 1997a, ApJ, **486**, 697

Alcock C. *et al.*, 1993, Nature, **365**, 621

Alcock C. *et al.*, 2000, Astrophys. J., **542**, 281

Allen P. R., Koerner D. W., Reid I. N., Trilling D. E., 2005, ApJ, **625**, 385

Alpher R. A., 1948, Nature, **162**, 774

Alsop D. C., Cheng, E. S., Clapp A. C. et al, 1991, ApJ, **395**, 317

Ansari R., Cavalier F., Moniez M. et al., (EROS), 1996, A&A, **314**, 94

Armendariz-Picon C., Mukhanov V. F. and Steinhardt P. J., 2000, Phys. Rev. Lett., **85**, 4438

Assef R. J., Gould A., Afonso C., Albert J. N., et al., 2006, ApJ, **649**, 954

Aubourg E. *et al*, 1993, Nature, **365**, 623

Auriere M. *et al*, 2001, ApJ, **553**, L137

Bahcall J., Piran T. , and Weinberg S., eds., World Scientific, 2004, Dark Matter in the Universe, Second Edition,

Bahcall J. et al., 1983, Astrophysical Journal, **265**, 730

Baltz, E. A. & Silk, J. 2000, ApJ, **530**, 578

Bartelmann M., 2010, Classical and Quantum Gravity, **27**, 233001

Bekki, K. 2008, MNRAS, **390**, L24

Bekki K., Chiba M., 2009, PASA, **26**, 48

Bekki K. & Stanimirović S., 2009, MNRAS, **395**, 342

Bennet C. L., Bay M., Hinshaw G. et al., 2003, ApJ, **583**, 1

Bennett C. L. et al., 2003, ApJ, **148**, 97

Bennett D. P., 2005, ApJ, **633**, 906

Besla G., Hernquist L., Loeb A., 2013, MNRAS, **428**, 2342

Binney J. & Tremaine S., 1987, Galactic Dynamics (Princeton, Princeton Univ. Press)

Binney J. *et al*, MNRAS, **397**, 1804

Binney J. and Merrifield M., 1998, Galactic Astronomy (Princeton Series in Astrophysics)

Bonometto S. A, Gabbiani F., Masiero A., Physical Review D (Particles, Fields, Gravitation, and Cosmology), 1994, **49**, 3918

Bovy J., Tremaine S., 2012, ApJ, **756**, 89

Bregman J. N., 2007, Ann. Rev. Astron. Astrophys., **45**, 221

Calchi Novati S., Paulin-Henriksson S., An J., Baillon P., et al., 2005, A&A, **443**, 911

Calchi Novati S., Mancini L., Scarpetta G., Wyrzykowski Ł., 2009, MNRAS, **400**, 1625

Calchi Novati S., Mancini L., 2011, MNRAS, **416**, 1292

Calchi Novati S., de Luca F., Jetzer P., Mancini L., Scarpetta G., 2008, A&A, **480**, 723

Calchi Novati S. 2010, Gen. Relat. Gravit. **42**, 2101

Calchi Novati S., de Luca F., Jetzer Ph., Scarpetta G., 2006, A & A, **459**, 407

Caldwell R. R. and Kamionkowski M., 2009, Ann. Rev. Nucl. Part. Sci., **59**, 397

Caldwell J. A. R., Coulson I. M., 1986, MNRAS, **218**, 223

Caldwell R. R., Dave R. and Steinhardt P. J., 1998 Phys. Rev. Lett., **80**, 1582

Ceccarelli C. & Dominik C., 2006, ApJ, **640**, L131

Chabrier G., 2003, PASP, **115**, 763

Chang K. & Refsdal S., 1979, Nature **282**, 561

Chemin L., Carignan C. and Foster T., 2009, ApJ, **705**, 1395 ApJ, **554,** 1044

Chiba T., Okabe T. and Yamaguchi M., 2000,Phys. Rev. D, **62**, 023511

Chun E.J., Kim H.B., Lyth D.H., Phys. Rev. D, 2000, **62**, 125001

Chwolson O., 1924, Astr. Nachrichten, **221**, 329

Cooray A. and Chen X., 2002, ApJ, **573**, 43

Copeland E. J., Sami M. and Tsujikawa S., 2006, Int. J. Mod. Phys. D, **15**, 1753

Copeland E. J., Liddle A. R. and Wands D., 1998, Phys. Rev. D, **57**, 4686.

Corbelli E. *et al*. 2010. A&A, **511**, A89

Courteau S. *et al*, 2011, ApJ, **739**, 20

Covi L., Kim H.B., Kim J.E., Roszkowski L., JHEP , 2001, **0105**, 033

Crowl H. H., Sarajedini A. et al., 2001, The Astronomical Journal, **122**, 220

Davis M., Huchra J., 1982, AJ, **254**, 437

de Bernardis P. et al., 2000, Nature, **404**, 959

de Bernardis P. et al., 2003, Memorie della Societa Astronomica Italiana, **74**, 75

de Boer W., Sander C., Zhukov V., Gladyshev A. V., Kazakov D. I., 2005, A&A, **444**, 51

de Jong J. T. A., Yanny B., Rix H.-W., Dolphin A. E., Martin N. F., Beers T. C., 2010, ApJ, **714**, 663

Dehnen W. and Binney J., MNRAS,**294**, 429

De Paolis F. et al., 2011, Astron. Astrophys. Lett., **534**, L8

De Paolis F. et al., 2012, Journal of Physics: Conference Series, **354**, 012004

De Paolis F. et al., 1995a, A&A, **299**, 647

De Paolis F. et al., 1999, ApJL, **510**, L103

de Rujula A., Jetzer P. & Masso E., 1991, MNRAS, **250**, 348

de Vaucouleurs G., 1959, Handbuch der Physik, **53**, 311

di Benedetto G. P., 2008, MNRAS, **390**, 1762

Di Stefano R., 2000, ApJ, **541**, 587

Dixon D. D. *et al.*, 1998, New Astronomy, **3**, 539

Dodelson S., 2003, Modern Cosmology, Academic Press

Dodelson S., Widrow L. M., 1994, Physical Review Letters, **72**, 17

Dominik M., 2010, General Relativity and Gravitation, **42**, 2075

Dong S., Udalski A., Gould A., Reach W. T., et al., 2007, ApJ, **664**, 862

Dopit M. A., Lawrence C. J., Ford H. C., Webster B. L., 1985, AJ, **296**, 390

Drake A. J. and Cook K. H., 2003, ApJ, **589**, 281

Durrer R. and Maartens R., 2008, Gen. Rel. Grav., **40**, 301

Einasto J., Kaasik A., & Saar E., 1974, Nature, **250**, 309

Einstein A., 1917, S.-B Preuss. Akad. Wiss., **1**, 142

Eisenstein D. J. et al. [SDSS Collaboration], 2005, ApJ, **633**, 560

Evans N. W., Kerins E., 2000, ApJ, **529**, 917

Evans C. J., Howarth I. D., 2008, MNRAS, **386**, 826

Faber S. M. & Gallagher J. S., 1979, ARA& A, **17**, 135

Falco E.E., Kochanec C. S., 1998, ApJ, **494**, 47

Feldman G. J., Cousins R. D., 1998, Phys. Rev. D, **57**, 3873

Feng J.L., Rajaraman A., Takayama F., Physical Review D, **68**, 085018

Freeman K. C., 1970, ApJ, **160**, 811

Gamow G., 1946, PhRv, **70**, 572

Garbari S., Liu C., Read J. I., Lake G., 2012, MNRAS, **425**, 1445

Gardiner L. T., Sawa T., Fujimoto M., 1994, MNRAS, **266**, 567

Gardiner L. T., Noguchi M., 1996, MNRAS, **278**, 191

Gerhard O.E., 1993, MNRAS, **265**, 213

Goenner H., Einfuehrung in die Kosmologie, Spektrum Akademischer Verlag, Heidelberg, 1994

Gold B. et al. 2011, ApJS, **192**, 15

Gonidakis I., Livanou E., Kontizas E., Klein U., Kontizas M., Belcheva M., Tsalmantza P., Karampelas A., 2009, A&A, **496**, 375

Górski, K. M. et al. 2005, ApJ, **622**, 759

Górski K. M, Hivon E.,Wandelt B. D., 1999, Proceedings of the MPA- ESO cosmology conference, Garching, Germany, 37, astroph/9812350

Goto T., Yamaguchi M., Phys. Lett. B, 1992, **276**, 103

Gott J. R. I., & Turner E. L. 1977, ApJ, **213**, 309

Gould A. 1992, ApJ , **392**, 442

Gould A., Bahcall J. & Flynn C., 1997, ApJ, **482**, 913

Gould A., 2001, PASP, **113**, 903

Gould A., 1995, ApJ, **441**, 77

Gould A., 1994, ApJ, **421**, L71

Gould A., 2003, ApJ, **583**, 765

Graff D. S., Gardiner L. T., 1999, MNRAS, **307**, 577

Grenacher L. *et al.*, 1999, A&A, **351**, 775

Gurzadyan V. G. *et al.*, 2010, Europhys. Lett.,**91**, 19001

Gyuk G., Dalal N., Griest K., 2000, ApJ, **535**, 90

Habibi F. *et al.*, 2011, A&A, **525**, 108

Han C. & Gould A., 1996, ApJ, **473**, 230

Han C. & Gould A., 1995, ApJ, **447**, 53

Han C., Gould A., 1995, ApJ, **449**, 521

Hardy E., Suntzeff N. B., Azzopardi M., AJ, **344**, 210

Hardy S.J. & Walker M.A., 1995, MNRAS, **276**, L79

Harris J., Zaritsky D., 2006, AJ, **131**, 2514

Harris J., Zaritsky D., 2004, AJ, **127**, 1531

Haschke R., Grebel E. K., Duffau S., 2012, AJ, **144**, 107

Hindman J. V., 1967, Australian Journal of Physics, **20**, 147

Hulsbosch A. N. M. & Wakker B. P., 1998, A&A, **75**, 191

Huterer D. and Turner M. S., 1999, Phys. Rev. D, **60**, 081301.

Jarosik N. et al., 2007, ApJS, **170**, 263

Jarosik N. *et al.*, 2011 Astrophys. J. Suppl., **192**, 14

Jetzer P., Mancini L., Scarpetta G., 2002, A&A, **393**, 129

Juríc M., Ivezić Z., Brooks A., Lupton R. H., et al., 2008, ApJ, **673**, 864

Kallivayalil N., van der Marel R. P., Alcock C., 2006, ApJ, **652**, 1213

Kapakos E., Hatzidimitriou D., 2012, MNRAS, **426**, 2063

King I., 1962, AJ, **67**, 471

King I. R., 1966, AJ, **71**, 64

Kinman, T. D. et al. 2004, Memorie della Soc. Astr. Ital., **75**, 36

Kirshner, R.P., Oemler, A., Schechter, P.L., and Shectman, S.A. 1983, AJ, **88**, 1285

Knapp G. R., Kerr F. J. & Williams B. A., 1978, ApJ, **222**, 800

Kochanec C. S., 1996, ApJ, **466**, 638

Kolb E. W., Turner M. S., The Early Universe, Addision-Wesley, Redwood City, 1990

Komatsu E. et al., 2009, [WMAP Collaboration], Astrophys. J. Suppl., **180**, 330

Kroupa Pavel, 2001, MNRAS, **322**, 231

Kroupa Pavel, 2007, astro-ph/0703124

Kroupa P.,Weidner C., Pflamm-Altenburg J., Thies I., et al., 2011 The stellar and sub-stellar IMF of simple and composite populations, published in Stellar Systems and Galactic Structure, **5**, Springer, arXiv:1112.3340

Kunkel W. E., Demers S., Irwin M. J., 2000, The Astronomical Journal, **119**, 2789

Landau L. D., Lifshitz E. M., 1989, The Classical Theory of Fields, Nauka

Lasserre T., Afonso C., Albert J. N. et al., (EROS) 2000, A&A, **355**, L39

Lee A. T. et al., 2001, ApJ, **561**, L1

Liebes S., 1964, Phys. Rev. B, **133**, 835

Mao S., 2012, Research in Astronomy and Astrophysics, **12**, 947

Mao S., Stefano R.D., 1995, ApJ, **440**, 22

Mancini L., Calchi Novati S., Jetzer Ph., Scarpetta G., 2004, A & A, **427**, 61

Maragoudaki F., Kontizas M. et al., 2001, A&A, **379**, 864

Massey R., Kitching T., Richard J., 2010, Reports on Progress in Physics, **73**, 086901

Mather J. C. Cheng E. S. et al., 1990, ApJ, **354**, L37

McConnachie A. W., 2012, AJ, **144**, 4

Fraser-McKelvie A. *et al*, 2011, MNRAS, **415**, 1961

Mollerach S., Roulet E., 2002, Gravitational lensing and microlensing, World Scientific

Moniez M., 2010, General Relativity and Gravitation, **42**, 2047

Moniez M., 2003, A&A, **412**, 105

Morras, R. et al. 2000, A&AS, **142**, 25

Nelson C. A., Drake A. J., Cook K. H., Bennett D. P., et al., 2009, ArXiv:0902.2213

Newton I., 1687, Philosophiae Naturalis Principia Mathematica (London: Royal Society) **315**, 55

Nidever D. L., Majewski S. R., Munoz R. R., Beaton R. L., Patterson R. J., Kunkel W. E., 2011, ApJ, **733**, L10

Ostriker J. P., Peebles P. J. E. & Yahil A., 1974, ApJ, **193**, L1

Paczyński B., 1986, ApJ, **304**, 1

Paczyński B., 1996, ARA&A, **34**, 419

Page T., 1962, ApJ, **136**, 685

Palanque-Delabrouille N., Afonso C., Albert J. N., Andersen J., et al., 1998, A&A, **332**, 1

Peebles P. J. E., Large Scale Structure of the Universe, Princeton University Press, 1980

Peebles P.J.E., 1993, Principles of Physical Cosmology, Princeton University Press

Penrose R., Structure of space time, B.A. Benjamin, Inc., 1968

Penrose R., The Road to Reality, Jonathan Cape, 2004

Penzias A. A. & Vilson R. W., 1965, ApJ, **142**, 419

Perlmutter S. et al., 1999, ApJ, **517**, 565

Persic M. & Salucci P., 1992, MNRAS, **258**, 14

Percival W. J. et al., 2010, MNRAS, **401**, 2148

Peterson S. D., 1978, Ph.D. Thesis, Cornell Univ.

Piatek S., Pryor C., Olszewski E. W., 2008, AJ, **135**, 1024

Press W. H., Teukolsky S. A., Vetterling W. T., Flannery B. P.,1992, Numerical recipes in FORTRAN. The art of scientific computing. Cambridge: University Press, 1992, 2nd ed.

Quinn D. P., Smith M. C., 2009, MNRAS, **400**, 2128

Quinn D. P., Wilkinson M. I., Irwin M. J., Marshall J., Koch A., Belokurov V., 2009, MNRAS, **396**, L11

Refsdal S., 1964, MNRAS, **128**, 295

Rest A., Stubbs C., Becker A. C., Miknaitis G. A., et al., 2005, ApJ, **634**, 1103

Rhie S. H., Becker A. C., Bennett D. P., Fragile P. C., Johnson B. R., King L. J., Peterson B. A., Quinn J., 1999, ApJ, **522**, 1037

Riess A. G. et al., 1998, AJ, **116**, 1009

Riffeser, A., Fliri, J., Seitz, S., & Bender, R. 2006, ApJS, **163**, 225

Riffeser A. *et al.*, 2003, ApJ, **599**, L17

Roberts M. S. & Whitehurst R. N., 1975, ApJ, **201**, 327

Rood H. J., & Dickel J. R., 1978, ApJ, **224**, 724

Rosenberg L.J., van Bibber K.A., 2000, Phys. Rep., **325**, 1

Roulet E. & Mollerach S., 1997, Physics Reports, **279**, 67

Rubin V. C. & Ford W. K. J., 1970, ApJ, **159**, 379

Sahu K. C., 1994, Nature, **370**, 275

Sahu K. C., Sahu M. S., 1998, ApJ, **508**, L147

Salati P., Taillet R., Aubourg É., Palanque-Delabrouille N., Spiro M., 1999, A&A, **350**, L57

Salpeter E.E., 1955, ApJ, **121**, 161

Sartore N., Treves A., 2010, A&A, **523**, A33

Sartore N., Treves A., 2012, A&A, **539**, A52

Smoot G. F., 1995, The Cosmic Background Radiation, Talk at Snowmass Workshop, astroph/9505139

Smith Sinclair, 1936, AJ, **83**, 23

Smoot G. F., Gorenstein M. V., Muller R. A., 1977, PhRvL, **39**, 898

Smoot G. F., Bennet C. L., kogut A., Wright E. L. et al., 1992, ApJ, **396**, L1

Spergel D. N. et al., 2007, ApJS, **170**, 377

Spergel D. N. et al., 2003, ApJ, **148**, 175

Spiro M., Aubourg E., Palanque-Delabrouille N., 1999, Nuclear Physics B - Proceedings Supplements, **70**, 14

Stanimirović S., Staveley-Smith L., Jones P. A., 2004, ApJ, **604**, 176

Strigari L. E., 2012, Galactic Searches for Dark Matter, Invited review to be submitted to Physics Reports, arXiv:1211.7090

Subramanian S., Subramaniam A., 2009, A&A, **496**, 399

Subramanian S., Subramaniam A., 2011, Proceedings of the 29th Meeting of the Astronomical Society of India, ASI Conference Series, **3**, 144

Subramanian S., Subramaniam A., 2012, ApJ, **744**, 128

Tegmark M. et al., 1996, ApJ, **464**, 35

Tisserand P. *et al.*, 2007, A&A, **469**, 387

Tonry J. L. et al., 2003, ApJ, **594**, 1

Turner E. L., 1976, ApJ, **208**, 304

Turner M. S., 1999, Second international workshop on particle physics and the early universe (COSMO-98). AIP Conference Proceedings, **478**, 113

Udalski A., Szymanski M., Kaluzny J. et al. (OGLE Coll.), 1993, Act. Astr., **43**, 289

Udalski A., 2003, Acta Astron., **53**, 291

van den Bergh S., 1999, A&ARv, **9**, 273

van der Marel R.P. & Franx M., 1993, ApJ **407**, 525

Vilardell F. et al. 2010, A&A, **509**, 70

Walker M. and Wardle M., 1998, Astrophys. J. Lett., **498**, L125

Weber M., de Boer W., 2010, A&A, **509**, A25

Westmeier T., Brüns C. & Kerp J., 2008, MNRAS, **390**, 1691

White M., Scott D., Silk J., 1994, ARA&A, **32**, 319

Wood-Vasey W. M. et al. [ESSENCE Collaboration], 2007, ApJ, **666**, 694

Wu X.-P., 1994, ApJ, **435**, 66

Wyrzykowski Ł., Kozłowski S., Skowron J., Belokurov V. et al., 2010, MNRAS, **407**, 189

Wyrzykowski Ł., Kozłowski S., Skowron J., Belokurov V., et al., 2009, MNRAS, **397**, 1228

Wyrzykowski Ł., Kozłowski S., Skowron J., Udalski A., et al., 2011a, MNRAS, **413**, 493

Wyrzykowski Ł., Skowron J., Kozłowski S., Udalski A., et al., 2011b, MNRAS, **416**, 2949

Yoo et al., 2004, ApJ, **603**, 139

Yoo J., Chanamé J., Gould A., 2004, ApJ, 601, 311

Yoshizawa A. M., Noguchi M., 2003, MNRAS, **339**, 1135

Zaritsky D., Harris J., Grebel E. K., Thompson I. B., 2000, The Astrophysical Journal, **534**, L53

Zoccali M., Cassisi S., Frogel J. A., Gould A., Ortolani S., Renzini A., Rich R. M., Stephens A. W., 2000, ApJ, **530**, 418

Zwicky F., 1937, Phys. Rev., **51**, 290

Zwicky F., 1937, Phys. Rev., **51**, 679

Zwicky F., 1933, Helv. Phys. Acta, **6**, 110

Zwicky F., 1937, ApJ, **86**, 217

(1) http://edelweiss.in2p3.fr/Presentation/

(2) http://darkerview.com/darkview/index.php?/archives/2335-Natures-Best-Magnifying-Glass-Views-Early-Spiral-Galaxy.html

(3) http://cfivarese.altervista.org/Dimensioni_Universo.html

(4) http://geopolicraticus.wordpress.com/2011/08/31/why-the-fermi-paradox-must-be-taken-seriously/

(5) http://www.astronomynotes.com/cosmolgy/s10.htm

(6) http://www.aao.gov.au/images/captions/uks017.html

(7) http://www.astro.rug.nl/~hidding/ao/ao.html